Contents

1 Sensor system for long-term analysis of fuel vapor restraint systems

Eva Schieferstein(1), Karl Meller(1), Ulrich Göbel(2), Ingo Schmitz(2), Thomas Seeger (2)

(1) Fraunhofer Institute UMSICH, Osterfelder Str. 3, D-46047 Oberhausen Germany
(2) Institute of Technical Thermodynamics, University Siegen, 57076 Siegen Germany

Abstract

Since the 1970s, fuel vapor restraint systems are used in vehicles to avoid leakage of volatile hydrocarbons from fuel tanks into the atmosphere. Different studies [1, 2] have shown that with the usage of blended fuels more fuel vapor restraint systems fail than usual.

In fuel vapor restraint systems activated carbons are used to adsorb volatile hydrocarbons from the gaseous phase above the fuel tank. The adsorption takes place while the car is parking. When running, ambient air is directed in counter-flow direction across the activated carbon filter for regeneration. By blending ethanol with fossil fuel the composition of the gaseous phase is changed.

To examine the influence of changed compositions on the adsorption process a device was designed, which enabled experimental investigations of many ad-/desorption cycles.

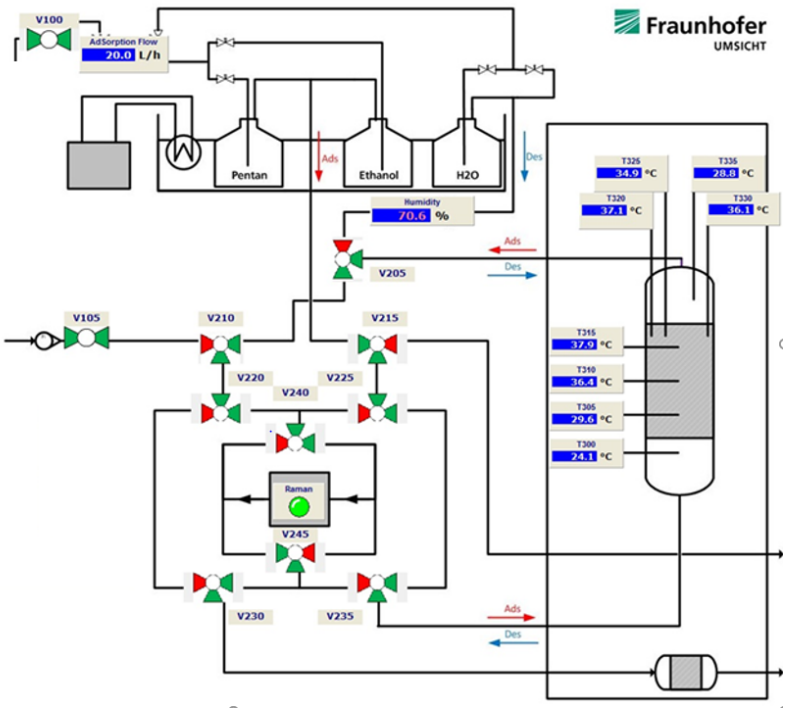

Fig.1: Schematic of adsorption device with Raman-detector and thermocouples

To get insight into the running processes different detectors are used:

- several thermocouples axially and radially distributed in the adsorber,
- a Raman-detector to analyze the composition of the gaseous phase upstream and downstream of the adsorber.

Measurements were done with different adsorptives and the composition of the purge gas was varied. Some results are shown and especially the influence of humidity of the purge gas is examined. By combining the measurement of the temperature in the adsorber with the knowledge of the gaseous composition, information about the influence of fuel additives on the adsorption processes in activated carbons is gained.

References

[1] H. Schmidt, TÜV Nord; „Swedish In-Service Testing Programme 2008 on Emissions from Passenger Cars and Light-Duty Trucks"; ISSN: 1401-9612, 2009

[2] G. Martini, U. Manfredi, M. Rocha, A. Marotta; „Review of the European Test Procedure for Evaporative Emissions: Main Issues and Proposed Solutions"; *JRC Scientific and Policy Reports*, 2012

Funding

Gefördert durch das Bundesministerium für Ernährung und Landwirtschaft (BMEL) (über die FNR) aufgrund eines Beschlusses des Deutschen Bundestages

FNR
Fachagentur Nachwachsende Rohstoffe e.V.

Gefördert durch:

Bundesministerium
für Ernährung
und Landwirtschaft

aufgrund eines Beschlusses
des Deutschen Bundestages

2 Numerical Evaluation of Seabed Influences on Underwater Electric Potential (UEP) Signatures and the Validation Framework

C. Broecheler(1), C. Thiel(1), F. Ludwar(2), J. Doose(2), A. Rennings(1), and D. Erni(1)

(1) General and Theoretical Electrical Engineering (ATE) University of Duisburg-Essen, D-47048 Duisburg, Germany
(2) Technical Center for Ships and Naval Weapons (WTD71), Deutsche Bundeswehr, D-24340 Eckernfoerde, Germany
E-Mail: claas.broecheler@uni-due.de Web: www.ate.uni-due.de

Abstract

Naval vessels are showing an underwater electric potential (UEP) signature generated by chemical potential differences of the ship's hull as well as by the corrosion protection systems. The UEP needs to be minimized to prevent the e.g. triggering of sea mines or other detections of the vessels. For such UEP signatures, the environment, in particular the electrical properties of the sea water and the seabed, is crucial for their amplitudes and shapes [1]. Additionally, beside the generated stationary electric fields, alternating current (AC) fields are present as well for example caused by the rotation of the ship's propeller [2]. Hence, a setup for the measurement of UEP signatures in the range of 0 Hz to 10 kHz is necessary together with a corresponding calibration system which is capable to compensate the environment influences of the measurement site.

For the calibration procedure it is essential to have a precisely known source. In order to design such a calibration source, a preliminary numerical evaluation is carried out with a simulation setup as sketched in Fig. 1 where on the one hand a submarine is placed in a free-water environment and on the other hand examined under measurement conditions including the seabed and the sensor array. As a simplification the ship's UEP signature is represented by a current dipole which is properly positioned and resized to mimic the real field distribution. Instead of discrete points corresponding to the positions of the sensors, the field is analyzed along a straight line emulating a crossing scenario. The software utilized for the numerical evaluation is the finite element method (FEM) based COMSOL Multiphysics simulator [3]. The applied permittivity and electrical conductivity of seawater are $\varepsilon_w = 81$ and $\sigma_w = 2.8$ S/m, respectively [4]. Above the sea level, air with $\varepsilon_l = 1$ and $\sigma_l = 0$ is used. The seabed consists of clay, sediments as well as shales and hence the electrical conductivity of this mixed composite material varies in the range of $\sigma_b = 0.1 \ldots 0.0001$ S/m [4]. Due to the penetration of seawater into the seabed layer the electrical conductivity is significantly increased. As a starting point for the numerical calculations an electrical conductivity of $\sigma_b = 0.73$ S/m is chosen. In order to achieve a dipole moment of 180 Am for the current dipole a length of 20 m and a current of 9 A is specified.

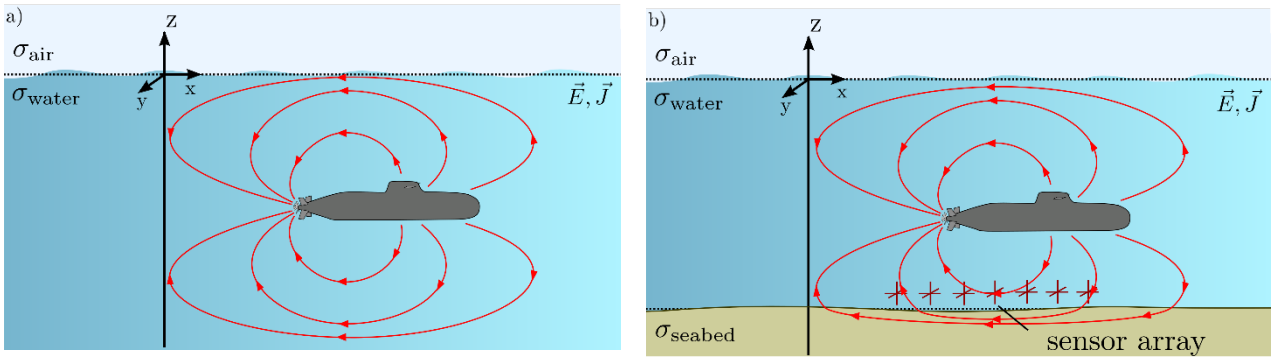

Fig.1: Schematic of the simulation setup of a submarine in a free-water environment (a) and above a seabed of close proximity (b). The sensor array for measuring the UEP signature of the vessel is placed with a certain distance above the seabed. The field lines of the electrical field as well as the electric flux density are displayed as red colored lines.

In case of a submarine in close proximity above the seabed, due to the large differences in conductivity, a reflection of the electric fields takes place at the boundary between the seawater and the seabed. In Fig. 2a) the simulated stationary UEP signatures of the two cases given in Fig. 1 are displayed component-wise. It is clearly evident that the UEP signature has larger amplitudes in case of a nearby seabed. In order to investigate the

influence of different conductivities of the seabed and the seawater a parameter sweep was carried out in the frequency range of interest.

The corresponding results are visualized in Fig. 2b) where the absolute value of the electric field is illustrated in a landscape plot. The changes in the seabed's electrical conductivity and the operating frequency result in different electrical field strengths, which tend to have a maximum value at virtually zero frequency and electrical conductivity, and decrease towards higher frequencies and conductivi-ties. The significant variations of the field values show that it is necessary to exactly retrieve the local measurement conditions and to extract the electric conductivities of the individual layers involved in the measurement by using a calibrated measurement system.

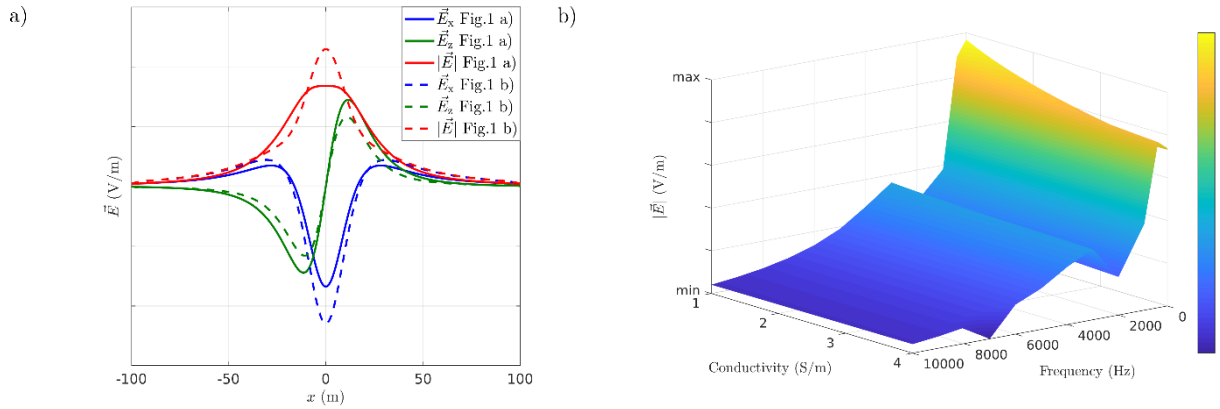

Fig.2: (a) Comparison of UEP signatures of a current dipole in free-water [cf. Fig. 1(a)], and in a 3-layer setup [cf. Fig. 1(b)] including the seabed and the sensor arrangement above; and (b) a landscape plot of the absolute value of the electrical field strength as a function of the operating frequency and the seabed's electrical conductivity.

In the following a 1:5 downscaled model for analyzing the 3-layer setup with a 20cm long current dipole in a correspondingly tailored water basin will be considered for validation purposes. Based on our preliminary simulations following requirements are summarized for the measurement setup with corresponding calibration features: (i) Compact and transportable dipole/multipole excitation system for signature generation; (ii) excitation currents of up to 10 A for DC and AC signals with frequencies up to 10 kHz; (iii) current dipole/multipole arrangement that can be mounted at arbitrary orientations;

The design process of the downscaled measurement system (i.e. dipole system) already resulted in a first prototype of a reconfigurable dipole/multipole current source that will be later used for calibration purposes and to extract the electrical conductivity and associated structural information of the seabed. Similar reconfigurable current sources of larger extent will later be used for calibration of the sensor arrays in the marine signature measurement site in Aschau, Germany. The overall goal is to experimentally estimate the true free-water UEP signature of the naval vessel by de-embedding the measured signature from all its environmental influences, namely from the seabed.

References

[1] D. Schaefer, “Vorhersage und Umrechnung korrosionsbedingter UEP-Signaturen von Wasserfahrzeugen,” Ph.D. dissertation, University of Duisburg-Essen, Duisburg, Germany, 2015.
[2] D. Schaefer, J. Doose, A. Rennings, and D. Erni, "Numerical analysis of propeller-induced low-frequency modulations in underwater electric potential signatures of naval vessels in the context of corrosion protection systems," COMSOL Conference 2011, Oct. 26-28, Stuttgart, Germany, pp. 25, 2011.
[3] Software COMSOL Multihphysics v5.4. [Online]. Available: https://www.comsol.com (accessed on March. 26, 2019).
[4] G. Schlögel, “Modellierung und Lokalisierung kleinräumiger Einlagerungen (Kriegsrelikte) im Untergrund mit Geo-radar,” Diploma thesis, Angewandte Geowissenschaften u. Geophysik, Montanuniversität Leoben, Austria, 2007.

3 Optical sensor system for time resolved in-cylinder temperature measurements in a diesel engine

Jürgen Wultschner[1,2], Fabian Feldhaus[1,2], Ingo Schmitz[1,2], Stephan Fitzner[3], Johannes Ullrich[3], Thomas Seeger[1,2]

[1] Institute of Engineering Thermodynamics, University of Siegen, D-57076 Siegen, Germany
(2) Center for Sensor Systems (ZESS), University of Siegen, D-57076 Siegen, Germany
(3) Hyundai Motor Europe Technical Center GmbH, D-65428 Ruesselsheim, Germany
E-Mail: juergen.wultschner@uni-siegen.de Web: https://www.mb.uni-siegen.de/tts/

Abstract

Major transformations are underway for the global energy sector, from growing electrification to the expansion of renewables, upheavals in oil production and globalization of natural gas markets. Nevertheless the World Energy Outlook shows that due to the increasing mobility the oil demand for passenger cars will be constant or even slightly increasing up to 2040 [1]. Therefore energy efficiency and as a consequence the improvement of the combustion process is the key mechanism that curbs fuel consumption and exhaust gas emissions. Characteristic for engine exhaust gas emissions are CO_2, CO, NO_x and particulate matters like soot. In Diesel engines right now NO_x formation and its reduction is one important objective. NO_x emission from a direct injection Diesel engine is mainly due to formation of thermal NO that is described by the Zeldovich mechanism. Thus, studying the in-cylinder temperature during Diesel combustion can provide useful insight into the formation and destruction of NO_x [2].

Conventional temperature measurement techniques have the disadvantage to impair the combustion. Optical methods do not perturb the measurement, nevertheless most of these need modifications of the engines [3]. Consequently, the measurement results in modified engines are not directly comparable to serial engines. One simple way to solve this problem is to use the glow-plug bore of a Diesel engine as mount of the measurement probe. Thereby it is possible to get optical access to the combustion without further modifications. Figure 1a shows the setup of the used emission spectroscopy based sensor (ESS) system. The designed probe head detects light in a cone with an angle of 25°, as schematically shown in Figure 1b. The optical probe is via fiber connected to a spectrometer. This allows spectrally and time resolved measurements of the internal combustion process.

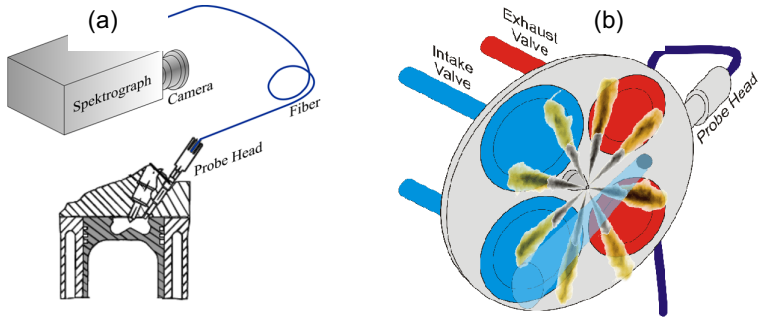

Fig.1: (a) Scheme of the ESS system setup. (b) Cylinder head with the screwed in probe head, which detects light in a cone with the angle α = 25 °.

During the combustion, the soot formed in Diesel engines emits radiation, which can be described as black body radiation. The soot temperature can be calculated with this approach by using a wavelength depended emissivity [4]. The combustion temperature can be achieved through a contour fitting procedure of the spectrally resolved signal and a previous calibration. In a preliminary work the functionality was validated by comparing ESS soot temperatures to coherent anti-Stokes Raman scattering (CARS) gas temperature measurements in a laminar flame [5].

In this work, the ESS system was used for temperature determination in a Hyundai 1,6 l DI Diesel engine with exhaust emission standard Euro 5. At a constant speed of 2000 rpm and 125 Nm load the parameters pilot injection, center of combustion (MFB) and exhaust gas recirculation (EGR) were varied, resulting in 13 different engine operation points. The chosen time intervals were 5°CA (crank angle) and 45°CA with starting points between 25°CA before and 60°CA after TDC (top dead center, 0°CA). Simultaneously the NO_x concentration in the exhaust gas was measured. Figure 2a shows an experimental spectrum achieved with the ESS-sensor system and the best fit, resulting in a temperature of 1777 K. As an example the temperature profile versus crank angle can be seen in Figure 2b for one engine operation point. The data achieved at all operation points were used to find one suitable time window representing clearly the correlation between temperature and NO_x concentration. This demonstrates that the ESS system can be used as an online tool for a time resolved analysis of the in-cylinder NO_x formation.

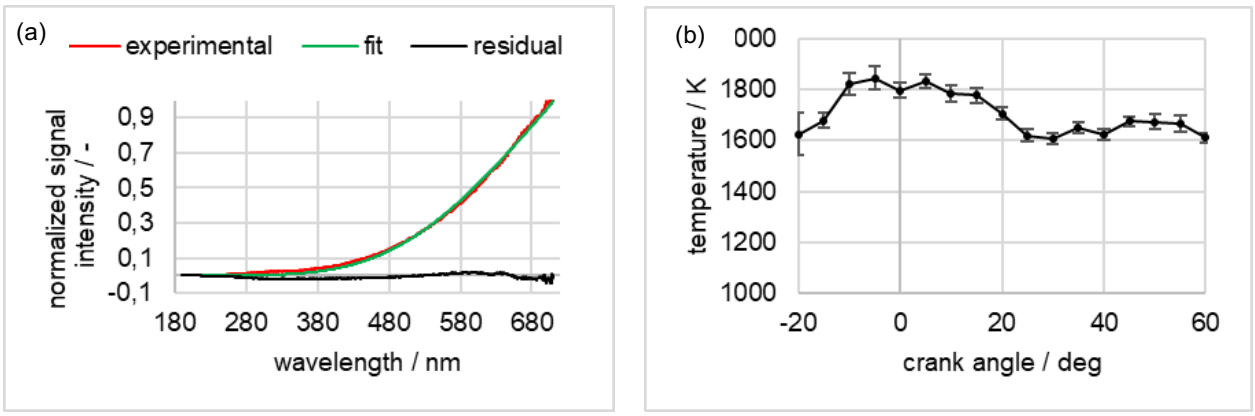

Fig.2: Engine operation point: EGR 50 %, exposure time 5°CA.

(a) Example of an experimental spectrum compared to the calculated function, resulting in a temperature of T = 1777 K (starting point 15°CA after TDC).

(b) Temperature profile versus crank angle.

References

[1] World Energy Outlook, 2018
[2] R. Pischinger, M. Klell, T. Sams, Thermodynamik der Verbrennungskraftmaschine. Der Fahrzeugantrieb, 3rd edn., Wien, Springer 2009.
[3] Bernd Block, Untersuchung von Möglichkeiten und Grenzen optischer Meßtechniken zur Temperaturbestimmung in Verbrennungsmotoren. Dissertation University of Hannover, Hannover November 21, 1997.
[4] H. A. Michelsen, "Understanding and predicting the temporal response of laser-induced incandescence from carbonaceous particles," J. Chem. Phys., vol. 118, no. 15, pp. 7012–7045, 2003.
[5] F. Feldhaus, I. Schmitz, and T. Seeger, "Emission spectroscopy based sensor developed for engine testing," Tech. Mess., vol. 84, no. 1, pp. 13–22, 2017.

4 Multitouch-capable Textile Touchpad using Polymer Optical Fibers

J. Kallweit1, C.-A. Bunge2, Member, IEEE, A. Bērziņš1, C. Grauberger1, P. T. S. Adi1, T. Gries1

(1) Institut für Textiltechnik (ITA) at RWTH Aachen University, Faculty of Mechanical Engineering, RWTH Aachen University, D-52074 Aachen, Germany
(2) Institut für Kommunikationstechnik (IKT), Leipzig, Hochschule für Telekommunikation Leipzig (HfTL), Gustav-Freytag-Str. 43-45, D-04277 Leipzig, Germany
E-Mail: jan.kallweit@ita.rwth-aachen.de

Abstract

Textiles and flexible textile surfaces can be found in many industrial goods, but also in car interiors and other automotive applications. Here, touchpads and other flexible touch-sensitive sensor arrays that can be integrated in these textile surfaces are increasingly in demand. In this contribution, a multi-touch capable textile touchpad based on polymer optical fibers (POF) is presented. The sensing fibers, in particular different fiber cross-section shapes – from circular to trilobal – are studied for maximum sensitivity and minimum cross talk.

Several concepts for textile touchpads have been proposed whereas most of them are based on electrical mechanisms like self- and mutual-capacitance [1,2], resistive potentiometry [3], piezo-resistance [4] or binary contact sensing [5]. These sensors have the disadvantage of being a source of electromagnetic interference or electric discharges or being susceptible to them.

Using light as a sensing medium is a well-known approach. POF are popular sensing fibers due to their mechanical properties, their low price and weight as well as their electromagnetic immunity POF are advantageous for sensor applications [6,7], whereas sensing pressure and deformation in particular are used for measuring touch inputs.

In this contribution, an improved design for a POF touchpad with a multitouch-capable 3x3 matrix is presented. One important aspect for the improvement of the sensitivity are special fibers with non-circular cross sections. The optimum shape in general and trilobal fibers in particular for a POF-based touchpad will be discussed.

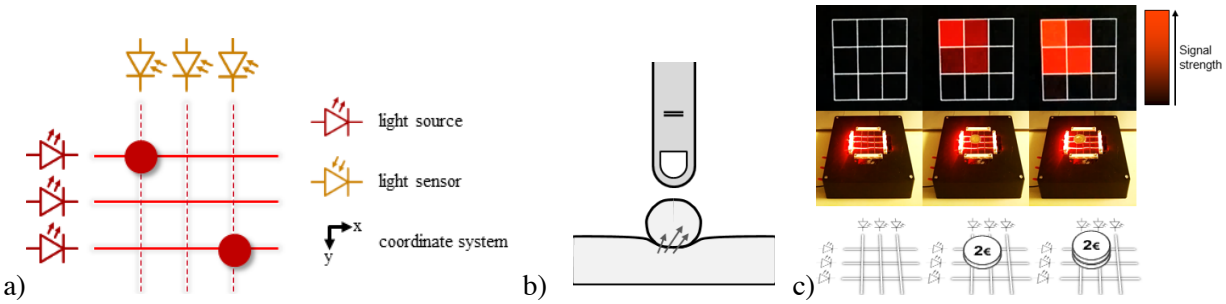

Figure 1: Concept of the optical textile touchpad based on crossing flexible optical fibers that act as input and sensing fibers (a). An applied force at a crossing leads to coupling between the two optical fibers (b). Demonstrator: the resting state, loaded state with a 2 € coin and finally with two coins. The measured signal is displayed in the grid above (c).

The basic principle of the presented touchpad is shown in Fig. 1 and similar to the one used by Gjellum et al. [8] It differentiates between two layers of POF lying orthogonally to each other. One layer contains the driven fibers, which are connected to light emitters, whereas the second layer contains the sensing fibers, which are connected to light detectors. In contrast to Gjellum et al. there is no separating layer in the presented demonstrator. With normal force being applied to the intersection of these fibers, light leaks from the driven into the sensed fiber. This principle is called cross-coupling. According to Hertzian contact theory, the area which enables the cross-coupling mechanism between the two fibers increases with the applied force. This enables the differentiation between different applied forces.

In order to assess the coupling efficiency and thus the sensitivity of the fibers, different pairs of fiber types have been tested as driven and sensing fibers. The evaluated POF were manufactured in a melt-spinning process and a subsequent water bath cooling as described by Beckers et. al. [9]. Different materials such as PMMA (Plexiglas® POQ66), PC (Makrolon® 2445), Bio-PC (DurabioTM D7340) and TPU (Desmopan® TPU 9662 DU) were used as alternatives.

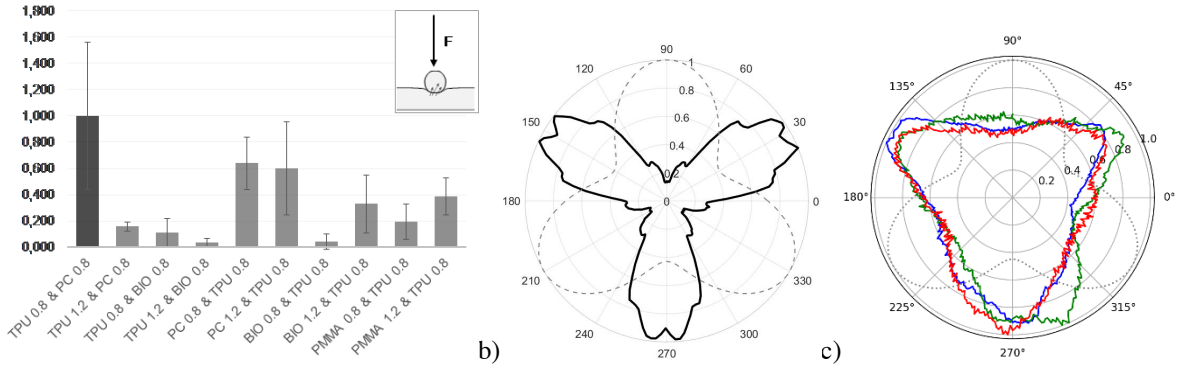

Figure 2: Averaged counts normalized by maximum, including error bars. The best fiber pair is indicated by a darkened bar (a); normalized radiation pattern of a trilobal fiber: simulation results (b) and measurement at three different positions (c). The dotted line represents the contour of the fiber

Fig. 2a shows the results of a first sensitivity test. Here, the fibers were laid orthogonal to each other, illuminated on one side and the optical signal was detected in terms of counts. The pressure was controlled with a special setup that ensured repeatability of the amount and direction of force and the shape of the contact area. The PC fibers showed a good combination of internal scattering and mechanical properties because of which this material combination lead to be strongest sensing signals. As shown in [10], POF with non-circular cross-section can be used to focus the side emission into certain directions. Figs. 2b) and c) show corresponding numerical and experimental results for the emitted light around the fiber circumference. For an optical touchpad, these preferential directions of refracted light rays can be used to either increase the cross-coupled signal between the driven and the sensing fiber or to reduce it in order to create a switch function, which needs a certain minimum normal force to start the cross-coupling mechanism. Depending on the chosen non-circular fiber shape, both can be the case.

Fig. 1c) shows the 3x3 matrix of POF touchpad with a spatial resolution of 15 mm. By sequentially illuming the driven fibers with a repetition rate of 10 Hz, multi-touch capability was achieved. The driven fibers were chosen to be made of TPU, the sensing fibers of PC, both with a diameter of 0.8 mm. The fibers are brought onto a piece of felt and tied with knots at their intersections. This ensures that the positions of the intersections are defined. Support fibers are placed on bottom to lift the sensed fibers off the felt and prevent light from leaking. The textile part of the touchpad (excluding electronics) is flexible and allows the device to function even being bent.

References

[1] M. Sergio, N. Manaresi, M. Tartagni, R. Canegallo, “A textile based capacitive pressure sensor”, Sens Lett 2004; 2(2): 153–160.I. S. Jacobs and C. P. Bean, “Fine particles, thin films and exchange anisotropy,” in Magnetism, vol. III, G. T. Rado and H. Suhl, Eds. New York: Academic, 1963, pp. 271–350.

[2] J. Meyer, B. Arnich, J. Schumm, “Design and modeling of a textile pressure sensor for sitting posture classification”, IEEE Sens J 2010; 10(8): 1391–1398.

[3] J.-S. Roh, "Textile touch sensors for wearable and ubiquitous interfaces." Textile Research Journal 84.7 (2014): 739-750.
M. Donneaud, C. Honnet, P. Strohmeier, “Designing a Multi-Touch eTextile for Music Performances”, Proceedings of the 17th International Conference on New Interfaces for Musical Expression (NIME’17), Aalborg, Denmark. 2017.

[4] M. Inaba, Y. Hoshino, K. Nagasaka, T. Ninomiya, S. Kagami, H. Inoue, “A full-body tactile sensor suit using electrically conductive fabric and strings”, IEEE/RSJ international conference on intelligent robots and systems (IROS 96), Osaka, Japan, 8 November 1996, vol. 2, pp. 450–457.

[5] K. Peters, “Polymer optical fiber sensors—a review” Smart Materials and Structures, Vol. 20(1), 2010.

[6] M. Plümpe, M. Beckers, V. Mecnika, G. Seide, T. Gries, C.-A. Bunge, “Applications of polymer-optical fibres in sensor technology, lighting and further applications”, pp. 311–335 in “Polymer Optical Fibres - Fibre Types, Materials, Fabrication, Characterisation and Applications”, 2017

[7] J. S. Schoenwald, A. W. Thiele, D. E. Gjellum, “A Novel Fiber Optic Tactile Array Sensor”, Proceedings, 1987 IEEE International Conference on Robotics and Automation. Raleigh, NC, USA, pp. 1792-1797.

[8] M. Beckers, T. Vad, B. Mohr, B. Weise, W. Steinmann, T. Gries , G. Seide , E. Kentzinger, C.-A. Bunge, “Novel Melt-Spun Polymer-Optical Poly(methyl methacrylate) Fibers Studied by Small-Angle X-ray Scattering”, Polymers, vol. 9(2): 60, 2017

[9] C.-A. Bunge, B. Mohr, T. Vad, M. Beckers, T. Gries, “Fabrication and analysis of side-emitting poly (methyl methacrylate) fibres with non-circular cross-sections”, Polymer International, vol. 67(9), pp. 1170-1178, 2018.

5 Coating-Defect Localization of Naval Vessels using the onboard Impressed Current Cathodic Protection System

Christian Thiel(1), Kevin Neumann(1), Claas Broecheler (1), Andreas Rennings(1),
Frank Ludwar(2), Jens Doose(2), and Daniel Erni(1)

(1) General and Theoretical Electrical Engineering (ATE), Faculty of Engineering, University of Duisburg-Essen, D-47048 Duisburg, Germany
(2) Technical Center for Ships and Naval Weapons, Naval Technology and Research (WTD 71), Bundeswehr, D-24340 Eckernförde, Germany
E-Mail: christian.thiel.ate@uni-due.de Web: https://www.ate.uni-due.de

Abstract

In this work a method for predicting coating damages of naval vessels using only highly aggregated information provided by the onboard corrosion protection system is presented. The estimation is based on a combination of computational electromagnetics (relying on a finite element method (FEM) simulator) and machine learning. The corrosion process of naval vessels mainly occurs due to different metallic materials which are galvanically connected where in presence of the seawater (electrolyte) a current density from the anodic material to the cathodic material through the seawater will always emerge. This current density field in combination with the electric conductivity of the seawater can alternatively be described as an electric field also known as the so-called *underwater electric potential (UEP)* signature.

The UEP signature is a relevant quantity in marine research especially in the context of signature silencing when using corresponding countermeasures such as e.g. signature minimization and signature management [1]. To prevent the emerging corrosion process, specific protection systems are usually installed on naval vessels, which can be classified in active and passive corrosion protection systems. As an example, a vector plot of the electric current density generated by an active corrosion protection system through the seawater is presented in Fig.1 which has been computed using the FEM simulation platform COMSOL Multiphysics [2].

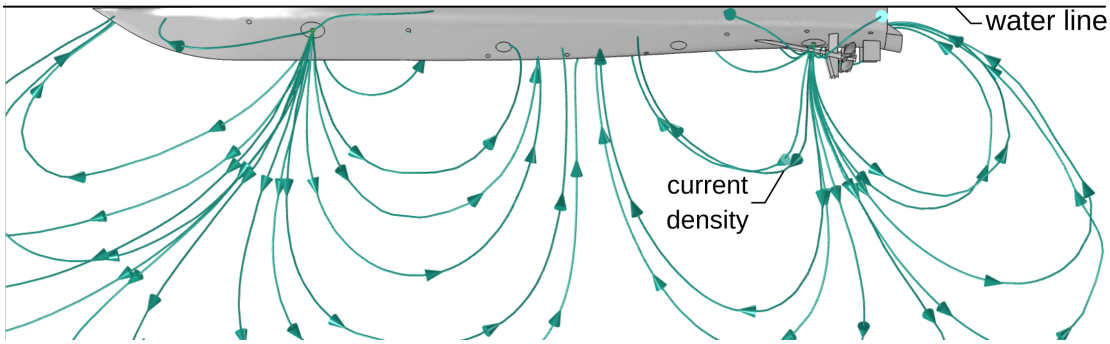

Fig.1: Simulated vector field of the electric current density using the finite element method (FEM) solver COMSOL Multi-physics [1]. The imposed current density points from the corrosion protection system towards the ship's hull and ensures a protective state of the vessel because it counteracts the ubiquitous electrochemically induced corrosion process.

The current density field visualized as streamlines in Fig.1 is pointing from the corrosion protection system (anode) towards the hull to ensure a protective (cathodic) state of the vessel. The active corrosion protection considered here is based on the *impressed current cathodic protection (ICCP)* system which uses a highly corrosion resistant anode material to actively impress anodic currents while enforcing the ship's hull in the desired cathodic regime and hence, inhibiting corrosion.

Additionally, another active corrosion protection scheme, namely the *sacrificial anodic cathodic protection (SACP)* system has been implemented on the vessel which is visualized in Fig. 1 as a regular distribution of small circular patches over the hull. The main reason for adding small SACP electrodes (anodes) to the ICCP

system is to smoothen the electric potential distribution over the hull yielding a more uniform corrosion protection potential. When a specific value of the electric potential on the underlying material surface is reached, this material can be considered as corrosion protec-ted. The exact values of said protection potentials are regulated in corresponding standards.

Passive corrosion protection is defined as a non-conducting coating of the vessel's hull and is also implemented in our numerical analysis. When introducing localized coating damages to the passive protection layer, the active corrosion protection system has to adapt while impressing higher ICCP currents to further maintain the corrosion protective state on the overall hull. Hence, an active control of the ICCP currents depending on the electric potential of the hull is needed. An iterative numerical method to provide a reliable (nonlinear) control scheme for the impressed ICCP currents has already been demonstrated in [3]. In the stationary state when the value of the control's leading variable (namely the corrosion protective state) is reached, ICCP anodes closer to the damaged region will have to provide higher impressed ICCP currents due to both, their proximity to the defects and the lower polarization resistance of the damaged region. This characteristic increase in ICCP currents can now be applied as indicator for the localization of emergent damages on the non-conductive coating.

In the following a classification system has been set up using the four highly aggregate ICCP currents as input variables of an artificial neural network (ANN) in order to identify a coating damage within a set of 12 predefined sectors on the hull (cf. Fig.2). Based on a dataset of 1000 simulated randomized damage scenarios in conjunction with the machine learning toolbox of Matlab [4], a correct tracking prediction rate of nearly 90% has been achieved for randomly sized circular hull damages at random positions on the ship's hull. This is an interesting outcome given the fact that ICCP currents are constantly monitored on real naval vessels. Our current activities are therefore focusing on a real-time monitoring system that should be capable of tracking down hull coating damages of navy ships on the move.

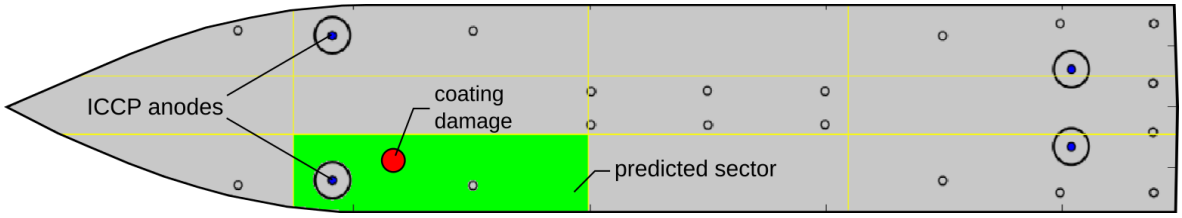

Fig.2: Example of a successful coating damage prediction on a realistic numerical ship model where its hull is sub-divided in 12 different sectors which are defined by the yellow lines. The 4 large patches represent the ICCP anodes whereas the positions of SACP electrodes are indicated by the smaller circular patches. The red patch stands for a potentially emerging coating damage on the hull (i.e. a damaged region). The green sector indicates the successful localization of the damage based on the proposed machine learning scheme.

References

[1] David Schaefer, Vorhersage und Umrechnung korrosionsbedingter UEP-Signaturen von Wasserfahrzeugen. PhD Thesis, University of Duisburg-Essen, Duisburg, April 15, 2015.
[2] Finite element method solver COMSOL Multiphysics: https://www.comsol.de (accessed March 27, 2019).
[3] C. Thiel, K. Neumann, C. Broecheler, F. Ludwar, A. Rennings, J. Doose and D. Erni, "Iterative electric potential adjustment of damaged naval vessels using the onboard ICCP-system," COMSOL Conference 2018, Oct. 22-24, Swisstech ConventionCenter, EPFL Lausanne, Lausanne, Switzerland, 2018.
[4] Matlab: https://www.mathworks.com/products/matlab.html (accessed March 27, 2019).

6 Investigation into polarized light scattering phenomena for optical aerosol characterisation

M.Sc. Lea Sichma[1], Dr.-Ing. Thorsten Schultze[1]

[1] *Chair of Communication Systems NTS, University of Duisburg-Essen D-47053 Duisburg, Germany*
E-Mail: lea.sichma@uni-due.de Web: http://nts.uni-due.de/

Abstract

Smoke detection plays an important role in the field of fire detection technology. Every smoke detector should detect a fire as early as possible, preferably already in the smouldering fire phase, in order to protect human lives and property. For this purpose, mainly optical scattered light smoke detectors are used in Germany. Although these smoke detectors detect the smoke, they also react to other aerosols such as dust or water vapour. In the domestic environment such false alarms repeatedly lead to the smoke detectors being switched off or removed. On the other hand in larger buildings, such as hotels, they lead to high financial costs due to the unnecessary fire brigade deployment.

The subject of this paper is the investigation into an optical smoke detector with reduced susceptibility to false alarms from dust and water mist.

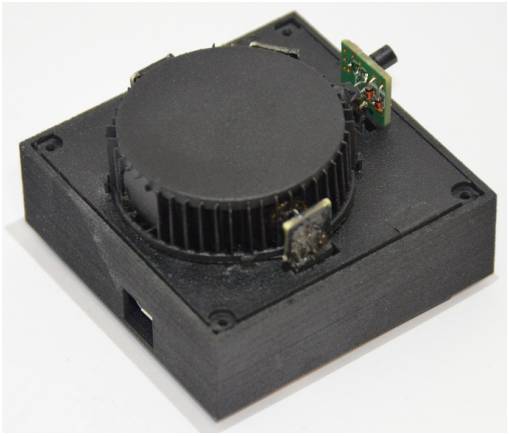

Fig.1: Prototype of a smoke detector with reduced susceptibility to false alarms in the size of a typical smoke detector

Subtitle

Smoke, water mist and dust can be distinguished by their scattering properties. These scattering properties depend on the structure of the individual particles. Smoke mainly consists of single spherical particles or agglomerates. Dust particles, on the other hand, have a rather angular structure. Due to this angular structure, the scattered light is partially depolarised.

Fig.2 shows the result of a measurement of this depolarisation effect for dust particles (a) and for smoke of a smouldering fire (b). The images were taken with a camera with a vertical polarization filter in front of it and show the scattering of two differently polarized light beams at the respective aerosol. The right beam has the same polarisation direction as the polarisation filter of the camera. The left beam, on the other hand, consists of parallel polarized light. A comparison of the two images clearly shows that dust (a) depolarises part of the light. This is not the case for smoke (b). Thus a purely optical differentiation of these two aerosols is possible [1], [4].

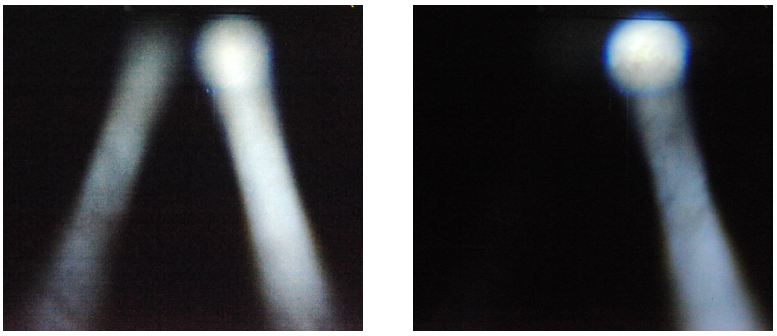

Fig.2: (a) depolarisation measurement with dust, (b) depolarisation measurement with smoke from a smouldering fire

Another natural phenomenon is used to distinguish between water mist and smoke. Due to the low absorption of a water droplet, light is scattered more strongly at certain angles than at other angles. One of these angles is the angle at which a viewer can see a rainbow. Fig. 3, for example, shows two images of the same rainbow taken at a scattering angle of about 138°. The left image was taken with a filter parallel polarised to the rainbow, the right image with a polarisation filter with orthogonal orientation. Already here it can be seen that the rainbow is only visible if the polariser is tangentially aligned to the rainbow. By mathematically determining the degree of polarisation at this angle, water droplets can be distinguished from smoke [1], [2], [3], [4].

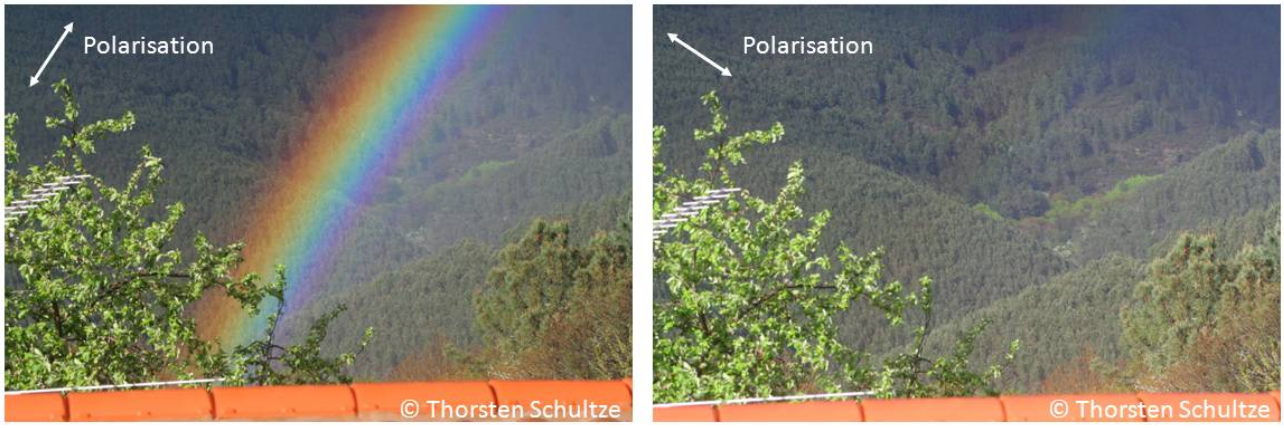

Fig.3: View of a rainbow with filters of different polarization directions [3]

References

[1] L.Marcius, Studie zur Anwendbarkeit einer staubresistenten optischen Methode für die automatische Detektion von Rauch, Masterthesis University of Duisburg-Essen, Duisburg, February 9, 2016

[2] L.Marcius, T.Schultze and I.Willms, "Design of a polarimetric scattering-based aerosol-classifying smoke detector prototype (AUBE 2017), September 12-14, Hyattsville, Maryland, USA, 2017.

[3] T.Schultze, L.Marcius, W.Krüll and I.Willms, "Polarised Light Scattering Analyses for Aerosol Classification (AUBE 2017), September 12-14, Hyattsville, Maryland, USA, 2017.

[3] Thorsten Schultze, Untersuchung zur Minderung von durch Störaerosole bedingten Fehlalarmen bei optischen Rauchmeldern, Dissertation University of Duisburg-Essen, Duisburg, May 18, 2010.

7 Simulation of microfluidic interferometer structures with liquid core waveguides in PDMS

Matthias Behmer[1], Vanessa Hapke[1], and Michael Schlüter[1]

[1] *Microsystems Engineering, Westphalian University of Applied Sciences D-45897 Gelsenkirchen, Germany*
E-Mail: Matthias.Behmer@studmail.w-hs.de Web: https://www.w-hs.de

Abstract

Integrated optofluidics significantly improves Lab-on-a-chip (LOC) applications while opening up the field for enhanced biochemical sensors. By integrating an optofluidic interferometer into a LOC, minor refractive index changes of liquids can be measured. These changes of the refractive index provide information about temperature, concentration, chemical modification, or other changes in the liquid. For the measurement of the refractive index the length of the measurement section is critical. State of the art is to guide light orthogonal to a fluid channel. In this setup, the length of the measurement section is limited by the divergence of the light. The solution to this problem is a liquid core waveguide as a sensing area. This requires a fluid channel which is aligned to the interferometer arm so that the light passes through this channel (*Fig.1*). By varying the length of the liquid core waveguide, the sensitivity can be optimized in relation to the system size. A space optimized sensitivity enhancement can be obtained by arranging the channel in a meandering pattern.

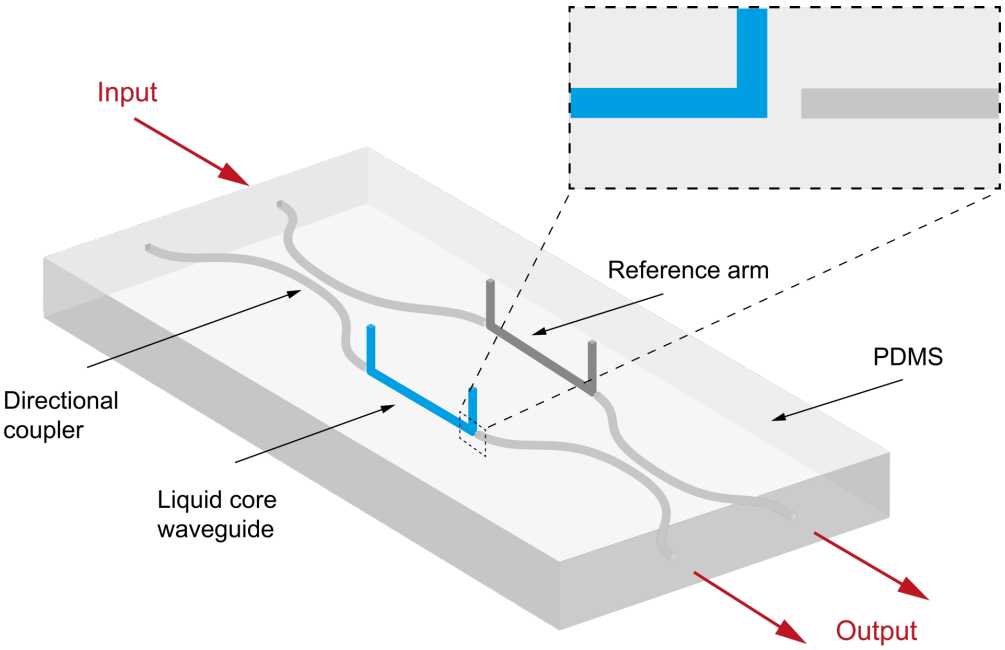

Fig.1: Scheme of the interferometric setup with liquid core waveguides

State of the art is producing liquid core waveguides from doped silica layers deposited on silicon wafers using plasma enhanced chemical vapor deposition . Many microfluidic and optofluidic structures, especially in LOC applications, are made from polydimethylsiloxane (PDMS). PDMS is relatively cheap, temperature resistant, gas permeable, biocompatible, has great optical properties and can be easily processed. Microfluidic as well as optical PDMS structures are generally molded from a masterform, which is usually made by a photolithographic process. This process offers the possibility of manufacturing an interferometer completely in PDMS. Optical structures like waveguides and coupler can be made by using PDMS with different refractive indices.

It is especially important that these structures have low optical losses. For the interferometric measurements single-mode waveguides are preferred to eliminate additional interference signals which would occur due to the mode dispersion. To ensure single-mode, the waveguide width has to be 9 μm or less for a wavelength of 1,31 μm.

This paper presents the design and simulation of a Mach-Zehnder interferometer in PDMS with a liquid core waveguide. Critical parameters can be obtained by the computer simulation. The interferometer was designed and analyzed in Comsol 5.3 by using a beam enveloping physical model and a boundary mode analysis study. The bidirectional transition of the coupler was realized by a waveguide which is bend in a cosine shape. This S-bend was optimized to get the most lossless structure [1,3].

The S-bend depends on the ratio of the length and the width of the transition region . A sufficient effective transition was defined and integrated in the coupler design. In interferometric setups the directional coupler is commonly used. Therefore, this coupler type was analyzed and for comparison, the Y-type coupler and the X-type were also simulated. All couplers were simulated and fitted to a 50:50 power ratio. The comparison between the three couplers yields that the least losses are achieved by the directional coupler. Thus, it was integrated in the interferometer design. The interferometer was analyzed with close attention to the power loss at the junction of the PDMS waveguide and the fluid channel. The analysis proves a neglectable power loss in the interferometer for the proposed application (*Fig. 2*).

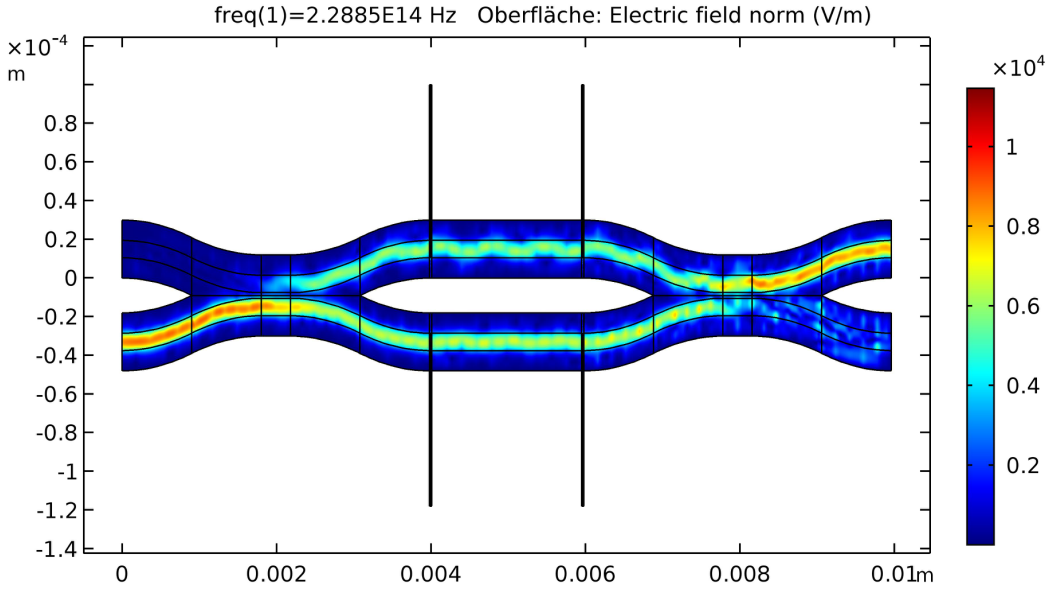

Fig.2: Simulation results of the interferometric setup with liquid core waveguides in PDMS.

References

[1] Patrick Dumais*, Claire L. Callender, Julian P. Noad and Christopher J. Ledderhof, "Integrated optical sensor using a liquid-core waveguide in a Mach-Zehnder interferometer," *OPTICS EXPRESS*, no. 16, 2008.

[2] P. Dumais, C. L. Callender, J. P. Noad, and C. J. Ledderhof, "Integrated optical sensor using a liquid-core waveguide in a Mach-Zehnder interferometer," *Opt. Express*, vol. 16, no. 22, pp. 18164–18172, 2008.

[3] G.A. Boghert, Y. C. Chen., "Low-loss Y-branch power dividers," *ELECTRONICS LETTERS*, no. 25, pp. 1712–1714, 1989.

8 Improvement of spectral representation by using single channel independent component analysis.

Rubens Rossi(1,2) , Norbert Gomolla(1)

(1) DMT GmbH & Co. KG, Industrial Engineering Dept. D-45307 Essen, Germany
(2) Faculty of Technology and Bionics, Rhein-Waal University of Applied Sciences, D-47533 Kleve, Germany
E-Mail: rubens.rossi@hochschule-rhein-waal.de rubens.rossi@dmt-group.de Web: www.mamma-project.eu

Abstract

Early damaged components produce weak and irregular impacts, whose frequencies are smoothed in a simple spectrum. Moreover, it is not always possible to place sensors to the desired locations and in the desired amount, in particular for retrofitting applications and in underground mining machines. As a result, the reduced availability of data increases the complexity of its processing to detect fault patterns.

The independent component analysis (ICA) belongs to the blind source separation methods and it is an unsupervised learning algorithm. Its goal is to find non-Gaussian hidden factors that are as much as possible statistically independent. Given that a source signal x is the sum of several components s, the goal of the ICA is to determine the mixing matrix A or the separating matrix W for the inverse transformation:

$$\mathbf{x}=\mathbf{As};\ \mathbf{A}=\mathbf{W}^{-1} \quad (1)$$

The ICA method has been used for condition monitoring purposes [1], [2] and also in single-channel analysis of vibrational data [3], [4].

In this abstract we examine the signal of a single sensor placed on a gearbox of a hard rock cutting machine. Fault frequencies in this environment are difficult to detect because the signal contains several components and it is highly contaminated by the vibration of the cutting process and by other equipment. Moreover, fault impulses do not always come out since the cutting process itself is discontinuous and the gearbox is thus irregularly loaded.

We use the independent component analysis (ICA) to process the signal of a one-dimensional time series. It is assumed that the components of the signal have non-Gaussian distribution and have disjointed spectra.

Artificial signals are created from overlapping blocks of the source signal and are then organised into a matrix which is then processed with ICA. This novel method is applied to a simulated signal and validated with experimental data, with and without damages.

According to the analysed machine, it is necessary to select one or more ICA components. In our case two components were sufficient to describe the phenomena, additional components would include less information and also make more difficult to comprehend the results.

The fig.1 compares the results of a traditional envelope spectrum with our proposed method. The graphs depict the analysis of a gearbox with damages. The frequencies, identified with a,b,c,d, correspond with the real characteristic frequencies of the shafts and bearings.

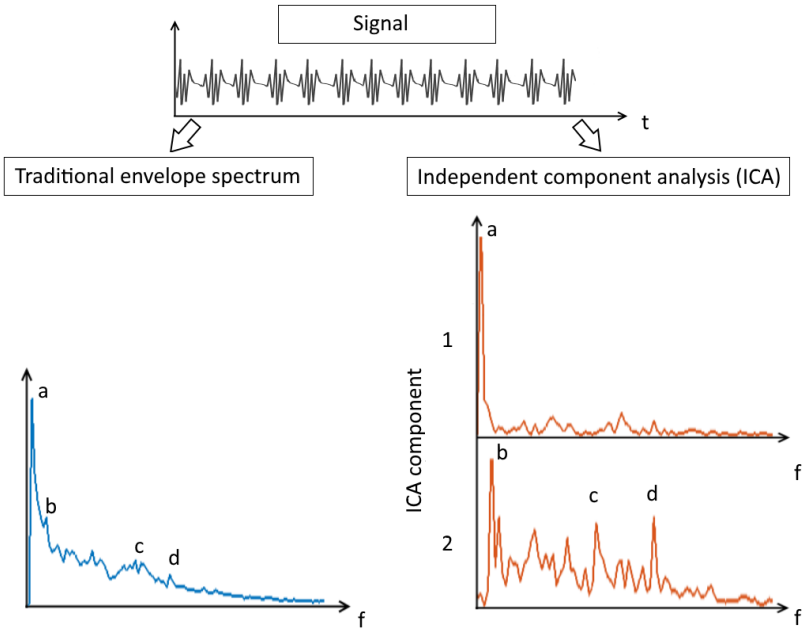

Fig.1: Comparison between envelope spectrum and the results of the analysis with ICA of a gearbox with defects. Letters a,b,c,d denote the characteristic frequencies of the investigated gearbox.

By using our new algorithm, the frequencies of the impacts are more distinguishable and the peak dynamic is improved.

Results demonstrate that the proposed method is able to reveal fault frequencies, which were not visible with a traditional method, in particular when the machine is under load.

In conclusion, the onset of the damage is clearly visible with the proposed algorithm. As a result, it is possible to detect the damage much earlier, which eventually reduces the maintenance cost.

Acknowledgments

R.Rossi is supported by EIT RawMaterials and by the program "Karrierewege FH-Professur" of NRW. N. Gomolla is supported by EIT RawMaterials.

References

[1] J. Wodecki, P. Stefaniak, J. Obuchowski, A. Wylomanska, and R. Zimroz, "Combination of ICA and time-frequency representations of multichannel vibration data for gearbox fault detection," *J. Vibroengineering*, vol. 18, no. 4, pp. 2167–2175, 2016.

[2] G. Yu, "Fault feature extraction using independent component analysis with reference and its application on fault diagnosis of rotating machinery," *Neural Comput. Appl.*, vol. 26, no. 1, pp. 187–198, 2014.

[3] M. E. Davies and C. J. James, "Source separation using single channel ICA," *Signal Processing*, vol. 87, no. 8, pp. 1819–1832, 2007.

[4] P. He, T. She, W. Li, and W. Yuan, "Single channel blind source separation on the instantaneous mixed signal of multiple dynamic sources," *Mech. Syst. Signal Process.*, vol. 113, pp. 22–35, 2018.

9 LIBS Microscopy for Elemental Imaging of Heterogeneous Samples

Thomas Dietz[a], Cassian Gottlieb[b], Peter Kohns[a], Georg Ankerhold[a]

[a]*University of Applied Sciences Koblenz – RheinAhrCampus Remagen, Laser Spectroscopy and Photonics, Joseph-Rovan-Allee 2, 53424 Remagen, Germany*
[b]*Secopta analytics GmbH, Rheinstraße 15b, 14513 Teltow, Germany*
E-mail: ankerhold@hs-koblenz.de Web: www.hs-koblenz.de/laser-spectroscopy

Laser-Induced Breakdown Spectroscopy (LIBS) with pulsed laser excitation is an established method for analyzing the elemental composition of unknown samples based on their characteristic emission spectra [1]. However, heterogeneous samples like concrete require high spatial resolution for a proper classification of the matrix phases [2-4]. An automated LIBS imaging system is used to provide high spatially and spectrally resolved images of the elemental distribution with a lateral resolution of 100 μm (Fig. 1) corresponding to the laser spot size. The system is able to analyze both the atomic and molecular emission with several spectrometers over a broad spectral range simultaneously.

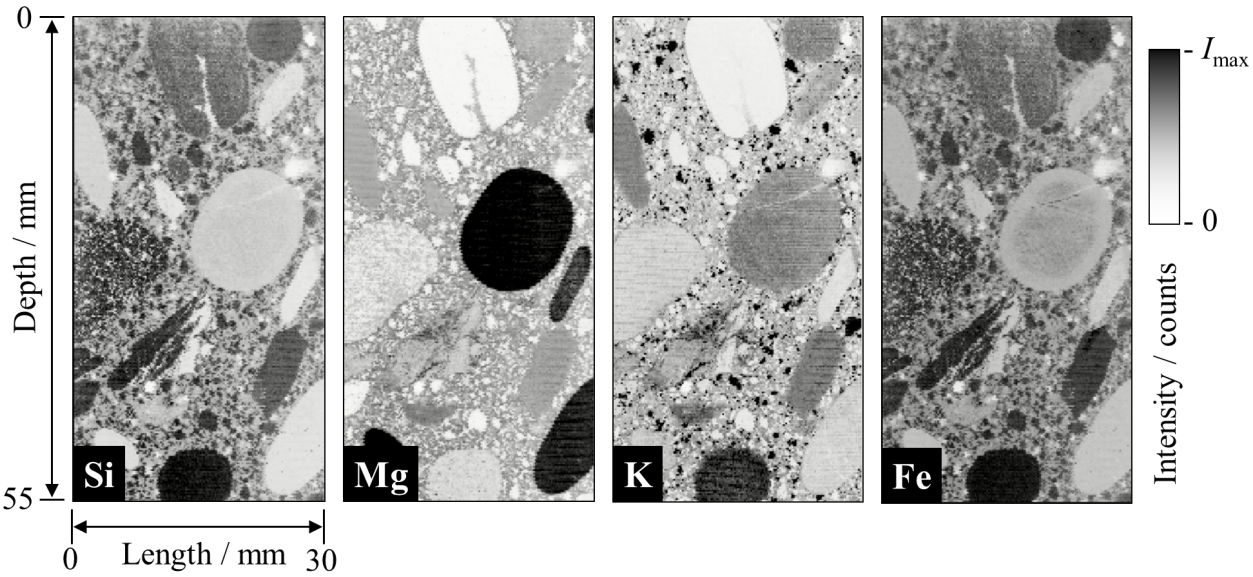

Fig. : Elemental LIBS imaging of silicon (Si), magnesium (Mg), potassium (K) and iron (Fe) of a concrete drill core. As indicated darker colors mean higher elemental concentration.

Critical corrosion effects like chloride induced pitting corrosion in concrete can substantially reduce the lifetime of infrastructure buildings. Since chlorides only diffuse into the cement phase of the concrete the diffusion profile of chlorides is of great interest.

The "LIBS-microscope" is able to visualize the elemental spatial distribution of chlorine in concrete by evaluating both the atomic and molecular emission (Fig. 2). Measurements with the LIBS microscope are compared to the results of the standard wet-chemical potentiometric titration which, however, provides a reduced spatial resolution of only 10 mm. Another drawback of the chemical analysis is the need of a correction factor to estimate the aggregate fraction because the matrix phases cannot be separated before performing the analysis. In practical applications this concrete-dependent factor is not known exactly. LIBS analysis, however, does not need any correction factor.

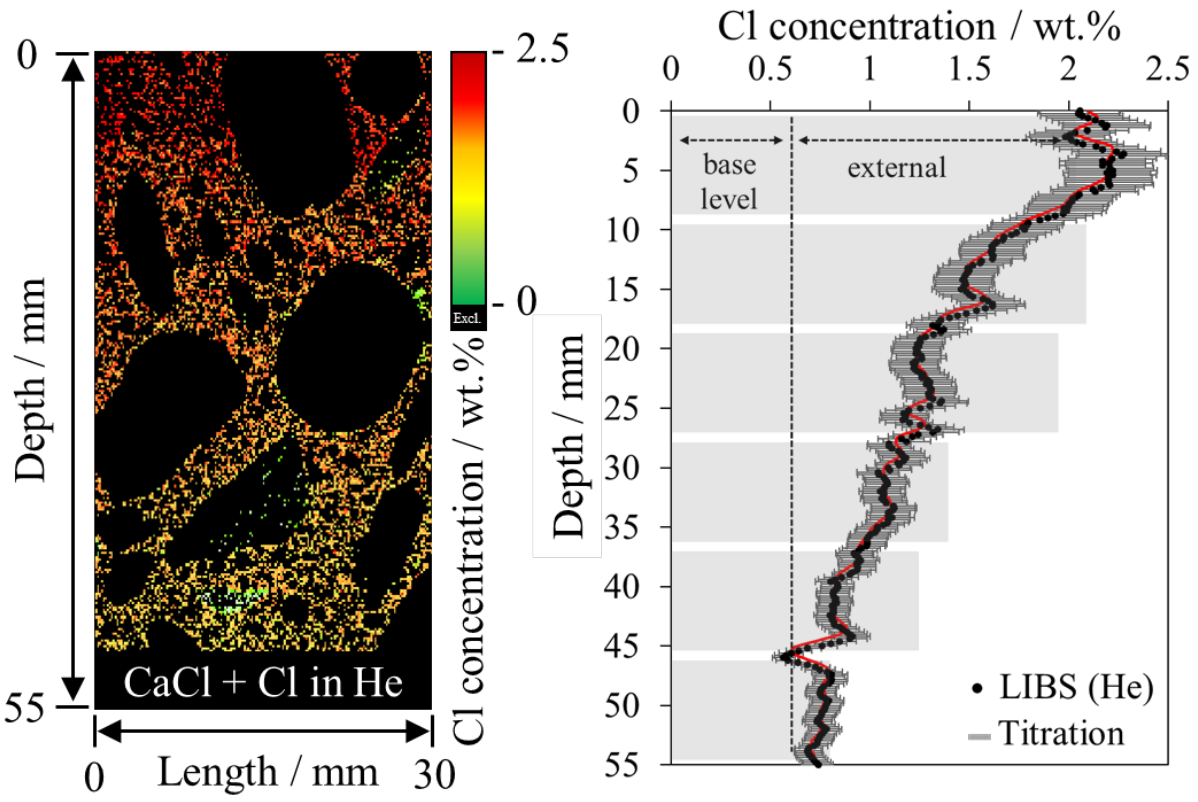

Fig. 2: LIBS imaging of the spatial distribution of harmful chlorides into a concrete drilling core in a helium atmosphere (left). The ingress profiles of chlorides determined by LIBS and by wet-chemistry show a very adequate correlation (right).

Acknowledgements

This project is supported by the German Federal Ministry for Economic Affairs and Energy (BMWi), project grant No. KF26821030F4. The authors thank in particular the BAM (Bundesanstalt für Materialforschung und -prüfung) and SECOPTA analytics GmbH both located in Berlin.

References

[1] R. Noll, "Laser-Induced Breakdown Spectroscopy: Fundamentals and Applications", Springer, 2012, ISBN-13: 978-3642206672.

[2] C. Gottlieb, S. Millar, S. Grothe, G. Wilsch, "2D evaluation of spectral LIBS data derived from heterogeneous materials using cluster algorithm", Spectrochim. Acta Part B, **134**: 58-68 (2017), DOI 10.1016/j.sab.2017.06.005.

[3] T. Dietz, P. Kohns, G. Ankerhold, "Quantitative determination of chlorides by molecular LIBS", Spectrochim. Acta Part B, **152**: 59-67 (2018), DOI 10.1016/j.sab.2018.12.009.

[4] C. Beresko, P. Kohns, G. Ankerhold, "Surface Element-Mapping of Three-Dimensional Structures by LIBS", Spectrochim. Acta Part B, **99**: 20-27 (2014), DOI 10.1016/j.sab.2014.06.004.

10 Measurement of ultrashort laser pulses using light-scattering media performing second harmonic generation

Anne-Sophie Rother, Peter Kohns, and Georg Ankerhold

University of Applied Sciences Koblenz – RheinAhrCampus Remagen,
Laser Spectroscopy and Photonics, Joseph-Rovan-Allee 2, 53424 Remagen, Germany
E-Mail: ankerhold@hs-koblenz.de *Web:* www.hs-koblenz.de/laser-spectroscopy

The duration of ultrashort laser pulses in the femtosecond regime can only be measured by optical autocorrelation. Therefore, single laser pulses are divided by a 50:50 beam splitter and conducted over two different paths with approximately the same optical length, before they are both focused on a nonlinear optical material that performs second harmonic generation (SHG) (see Fig. 1). By making one of the path lengths adjustable the two pulse halves can be temporally superimposed. Measuring the second harmonic signal intensity for adjustments of spatial and temporal overlap in comparison to the left and right-side non-overlap (i.e. using one path to scan the other one), the pulse duration can be calculated from the full width at half maximum (FWHM). This procedure can be seen as the underlying method of several ultrashort pulse measurement techniques like e.g. FROG [1].

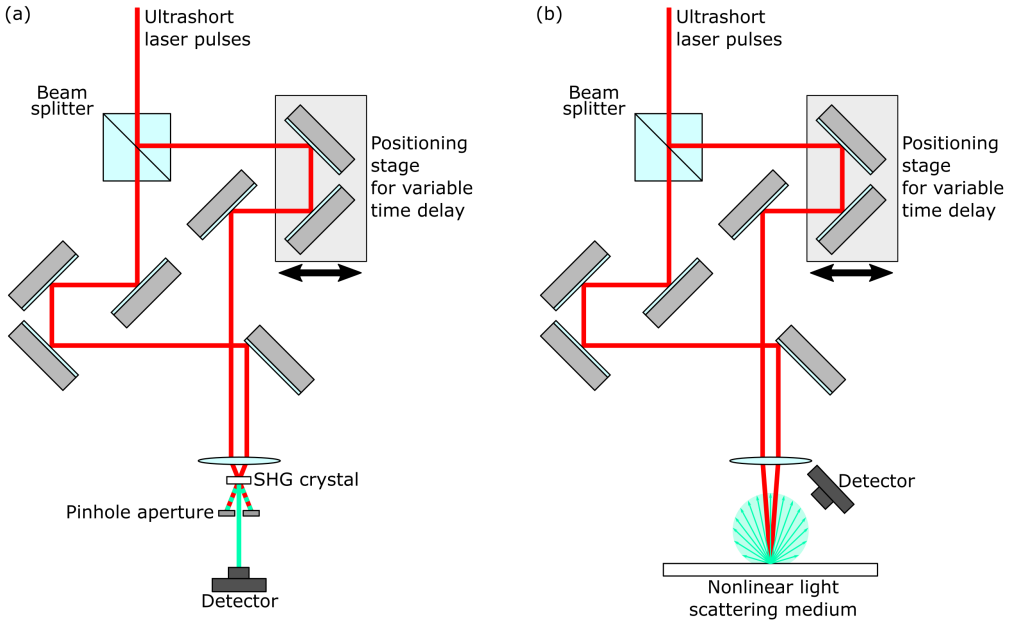

Fig.1: Experimental setup of intensity autocorrelation. Observed second harmonic generation (SHG) is achieved in (a) transmission by a nonlinear optical crystal such as beta barium borate and (b) a frequency doubling light scattering surface such as aluminum nitride.

The standard nonlinear material for autocorrelators is monocrystalline beta barium borate (BBO), which is used in transmission for non-collinear phase matching (Fig. 1(a)). The advantage is to be able to use low pulse energies as well as to measure background free as depicted in Fig. 2(a). However, BBO crystals are brittle and expensive.

Since fiber-based high energy femtosecond laser systems become more and more achievable, it may not be necessary to use BBO. For generating second harmonic signals we chose a fairly uncommon approach by using nonlinear light-scattering media in diffuse reflection instead of monocrystalline BBO in transmission.

Determining the nonlinear optical properties of scattering materials like powders has previously been of interest [2, 3], but to our knowledge scattered second harmonic signals have not been used for pulse duration measurements by now.

We compared the applicability of several light-scattering nonlinear media such as aluminum nitride (AlN), pressed ammonium dihydrogen phosphate (ADP), zinc oxide (ZnO) powder, and ZnO crystals grown by irradiating zinc spray with femtosecond laser pulses as described in [4].

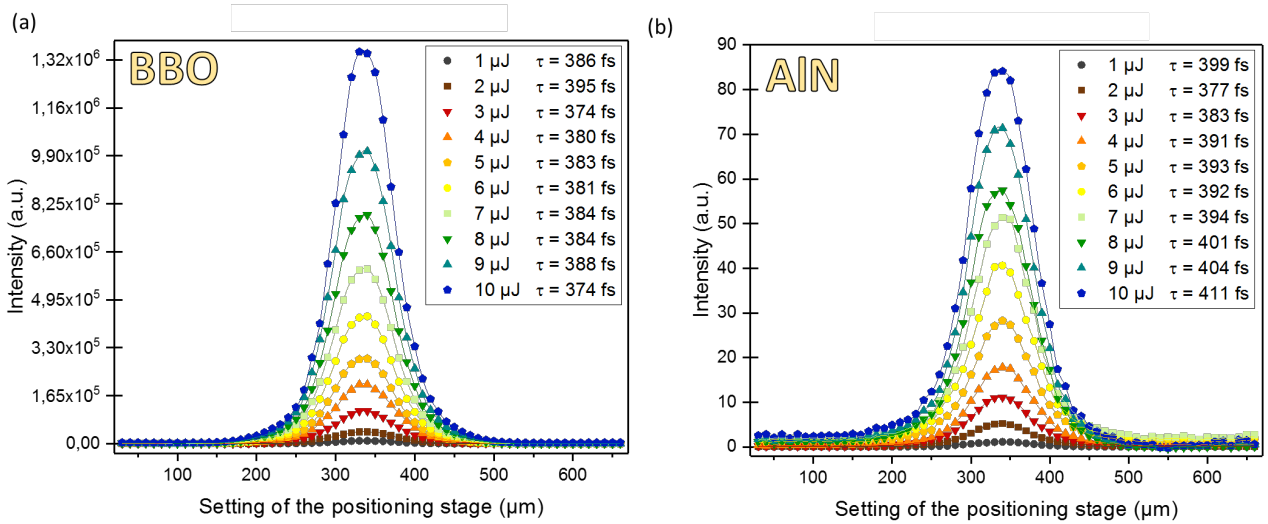

Fig.2: Intensity autocorrelations of laser pulses with a specified duration of 350 fs for 1 to 10 µJ at a repetition rate of 50 kHz using (a) beta barium borate (BBO) and (b) aluminum nitride (AlN). Intensities were estimated with the same spectrometer.

Fig. 2 illustrates SHG results of BBO (Fig. 2(a)) and AlN (Fig. 2(b)) obtained with an experimental setup as shown in Fig. 1. Allowing for measurement inaccuracies, calculated pulse durations are comparable. The scattered signal is typically symmetric and reveals a smooth shape as expected.

Although SHG signals for AlN are weaker by a factor of roughly 10^4 this does not turn out to be problematic for ultrashort laser pulses in the microjoule range at pulse repetition rates of some kilohertz. In addition, homogeneous scattering media do not need complicated adjustment unlike monocrystalline BBO.

In conclusion we present a simple and low-cost method to measure the duration of ultrashort pulses in the microjoule range.

Acknowledgements

We gratefully thank CeramTec GmbH for kindly providing us with samples of aluminum nitride for our research.

References

[1] R. Trebino, *Frequency-Resolved Optical Gating: The Measurement of Ultrashort Laser Pulses*. Springer Science+Business Media, 2000, ISBN: 978-1-4613-5432-1.

[2] S. K. Kurtz, and T. T. Perry, "A powder technique for the evaluation of nonlinear optical materials", J. Appl. Phys., 39: 3798 (1968), DOI 10.1063/1.1656857.

[3] I. Aramburu, J. Ortega, C. L. Folcia, and J. Etxebarria, "Second-harmonic generation in dry powders: A simple experimental method to determine nonlinear efficiencies under strong light scattering", Appl. Phys. Lett., 104: 071107 (2014), DOI 10.1063/1.4866160.

[4] A.-S. Rother, P. Kohns, and G. Ankerhold, "Scattered second harmonic generation on ultrashort laser pulse processed coatings", JNOPM, 27: 1850028 (2018), DOI 10.1063/1.1656857.

11 FPGA based time measurement for SiPM pulses

Jens Winter[1], Björn Brachhäuser[2], Stefan Heidbrink[1] and Michael Ziolkowski[1]

[1] Electronics Development Lab, Faculty IV, Department of Physics, University of Siegen, D-57076 Siegen, Germany
[2] Microsystems and Medical Computer Science, Faculty IV, Department of Electronics and Computer Sciences, University of Siegen, D-57076 Siegen, Germany
E-Mail: jens.winter@uni-siegen.de Web: http://www.uni-siegen.de

Abstract

SiPM applications with low numbers of photons require low thresholds and thereby produce high dark counts. This often leads to the point where the minimal threshold is limited by the data bandwidth of the acquisition system. Data reduction due to high dark counts usually has to be done after the readout bottleneck during the offline analysis. Multi-channel SiPMs are commonly read out through ASIC-based systems, which cannot however offer the flexibility needed to implement specific online criteria for data reduction in each experiment.

Our goal is to develop a flexible and cost-efficient solution to measure SiPM pulses on a time scale of pico-seconds with integrated online data reduction. To achieve this goal, we use standard FPGA evaluation boards for implementing time-to-digital converter (TDC), data reduction and data acquisition. The implemented FPGA code is highly modular, so that reduction criteria, e.g. coincidence of events on a set of channels, can be implemented and parametrized fast and with minimum effort. Each TDC channel provides a resolution of 22ps while processing up to one event every 2.5ns. Only those events meeting the criterion set are transferred to the FPGAs Block-RAM, where the data is organized in frames. One frame contains the data of all 16 channels whereas, 65536 frames can be buffered. The Block-Ram is implemented as a FIFO, which can be read continuously or in a burst mode depending on event rate, bandwidth of the readout interface and user preferences.

As the FPGA requires digital signals, additional hardware is needed to amplify and discriminate the SiPM pulses. This is accomplished with help of two electronic boards developed with standard signal interfaces for modular and flexible use. The first one carries the SiPM and provides a PC-controlled bias voltage and its monitoring, while connecting each SIPM channel to an SMA output. The second one contains a two-stage amplifier and a discriminator for each channel as well as an FMC connector to the FPGA.

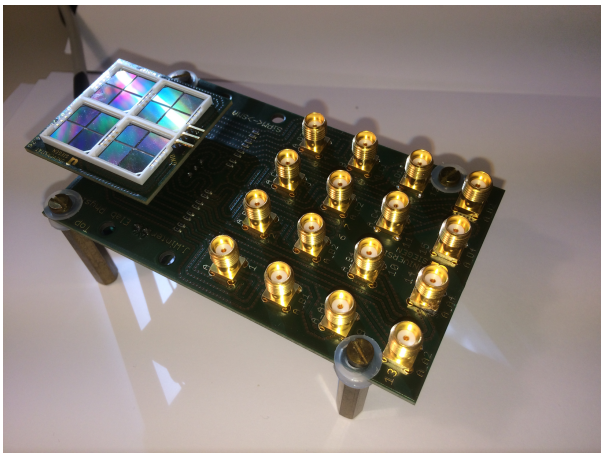

Fig.1: PCB for bias supply and SiPM connectivity

Referenzen?

12 Characterization and Error Analysis of Commercial Laser Displacement Sensors

Markus Beck[(1)] and Gerhard Fischerauer[(1)]

[(1)] *Chair of Measurement and Control Systems, Faculty of Engineering Sciences, University of Bayreuth, D-95440 Bayreuth, Germany*
E-Mail: Markus1.Beck@uni-bayreuth.de Web: www.mrt.uni-bayreuth.de

Abstract

Laser triangulation is widely used for displacement measurements. As an optical measurement technology, it offers several benefits over classical mechanical approaches: No force is applied to the target surface that could influence the target, and since no mass has to be moved, a highly dynamic behavior can be achieved. Comparing with other optical measurement systems, triangulation provides a higher resolution (yet, typically over a smaller range) than time-of-flight based systems and is simpler (however, less precise) than interferometric systems.

The principal idea behind this method is fairly simple (

Figure 3 (a)): A laser source is used to project a single spot – there are other sensors available which use lines or even 2-dimensional patterns, but those are not subject of this work – on the target surface. This spot is observed with a detector, usually a single column of photodetectors combined with some optical lenses. The distance of the target surface is then calculated from the angle, under which the laser spot is observed, combined with the known distance and relative orientation between laser source and the detector, using simple trigonometric relations.

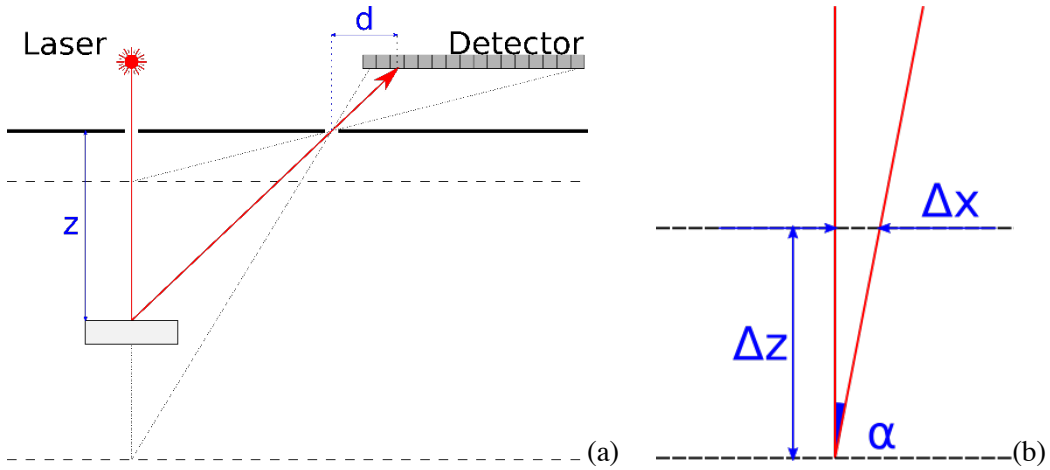

Figure 3: (a) Principal operation of a laser triangulation displacement sensor, consisting of a laser source and a linear photodetector array. (b) Equivalence between a change in vertical displacement and a change in horizontal displacement of the laser spot.

In practical realizations there are several error sources [1]. For one, there are geometric errors, concerning the exact distance and orientation of the laser source and detector or non-ideal behavior of the involved optics. Those errors are basically static, may, however, depend upon environmental conditions such as temperature. As the necessary calculations to determine the distance are highly non-linear, those errors may result in a non-linear sensor characteristic.

Another error source results from the signal processing necessary to determine the position of the laser spot. Commercial laser distance sensors usually aim for a small form factor, therefore placing laser source and detector in close proximity.

As a result, the position of the laser spot must be determined with high precision, as illustrated in

Figure 3 (b). This usually means that the center of the laser spot has to be measured with sub-pixel resolution, meaning that the intensity must be expressed as an interpolation function. While there is usually no information on this interpolation available for commercial sensors, there are reports of resolutions of up to 0.01 pixels in literature [2].

For example, the Panasonic HL-G112 sensor has an angle of 11° at center distance between the emitting and the receiving axis (in

Figure 3 (b) denoted as α) [3]. This means that an error Δx in calculating the center of the laser spot is magnified by a factor of 5.1 to an apparent displacement Δz.

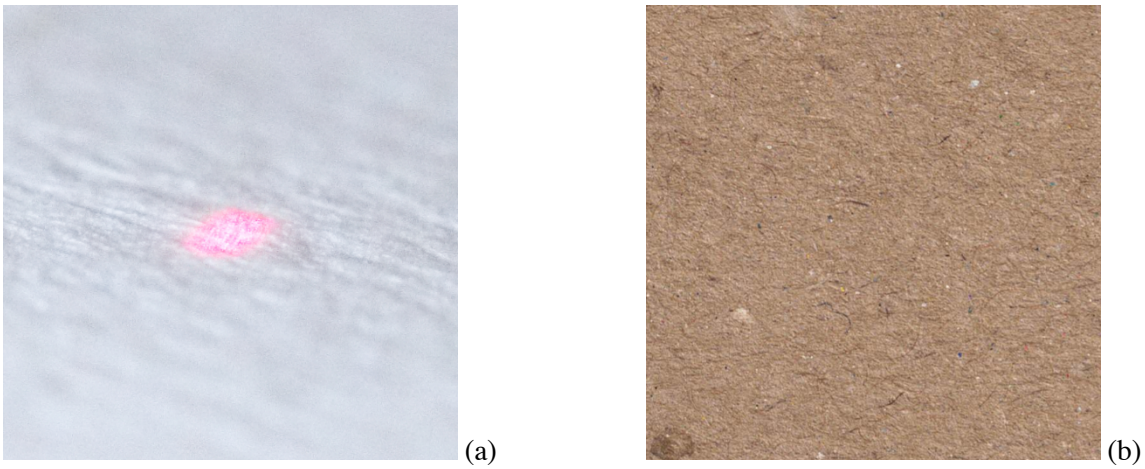

(a) (b)

Figure 4: Small-scale surface properties of technical paper samples that can influence sub-pixel accuracy: (a) Surface roughness (note: the here visible laser spot has a size of about 0.1 mm); (b) Color differences due to material inhomogeneity.

Utilizing the detected per-pixel intensity results in additional sources of measurement error, as this can be influenced by effects like the surrounding lighting or the small-scale surface properties of the target (examples in

Figure 4). Since those are more or less random, those problems are observed as noise when the measurement is repeated. Similar problems are also known to occur with reflective (usually metallic) surfaces, where local maxima in reflectivity cause so-called “speckle noise” [4].

This work analyzes the properties of commercially available laser displacement sensors with a special focus on applications in industrial paper processing. Those sensors usually employ different technologies intended to counter the problems mentioned above. Usually, however, no details are given in the datasheets, and the sensor characteristics are recorded only under idealized conditions. Therefore, these sensors can only be seen as a black box to be characterized for the required conditions.

Acknowledgements

This work was supported by the German Federal Ministry for Economic Affairs and Energy, grant number ZF4152307PO8.

Supported by:

Federal Ministry for Economic Affairs and Energy

on the basis of a decision by the German Bundestag

References

[1] X.-Q. Wen and J.-Y. Liang, “Application of Kalman Filtering Algorithm in Laser Triangulation Measurement,” in *2017 36th Chinese Control Conference (CCC): Application of Kalman filtering algorithm in laser triangulation measurement*, Dalian, China, 2017, pp. 5523–5527.

[2] A. Alam, M. O'Nils, A. Manuilskiy, J. Thim, and C. Westerlind, “Limitation of a Line-of-Light Online Paper Surface Measurement System,” *IEEE Sensors J.*, vol. 14, no. 8, pp. 2715–2724, 2014.

[3] Panasonic, “Abstandsensor mit Präzisionslaser: Serie HL-G1,” 2014.

[4] S. Ibaraki, Y. Kitagawa, Y. Kimura, and S. Nishikawa, "On the Limitation of Dual-View Triangulation in Reducing the Measurement Error Induced by the Speckle Noise in Scanning operations," *Int. J. Adv. Manuf. Technol. (The International Journal of Advanced Manufacturing Technology)*, vol. 88, no. 1-4, pp. 731–737, 2017.

13 Investigation on Shape Evolution of Free Side Surface of Rolled Bar and Rod by Lateral Spread with Image Processing and 3D – Scanning for Improvement of Roll Pass Design Model

Rolf Braun[(1)], Christian Overhagen[(1)] and Rüdiger Deike[(2)]

[(1)] Metal Forming [(2)] Chair for Metallurgy and Steel Production, University of Duisburg-Essen, D-47119 Duisburg, Germany
E-Mail: rolf.braun@uni-due.de Web: www.uni-due.de/umf

Abstract

For reaching high accuracy in cross-sectional size as well as a reduced deviation from the ideal shape of rolled bars and rods process models are used. In the rolling process material is partly in touch with the rolls by which the force is applied to get plastic deformation and formation of the shape. In the roll gap some parts of the surface of the material are not in contact with the tool which allows the material to flow lateral and form a free surface. This work treats the shape evolution of that free side surface. Cross section and the deformation zone of rolled bars and rods are investigated with the help of image processing and 3D-structured-ligth scanning to gain empirical models for prediction of the shape. This work is part of the EFRE project PIREF which is a combination of sensor development, process modeling and process control system development with the aim to increase dimensional accuracy in hot rolling mills for hot rolled bars and rods.

Introduction

The calculation of spread for irregular passes is commonly done by the help of an equivalent flat pass [1], where mean initial and final height and working diameter is calculated to be used in spread formulas developed for flat passes [2]. For the calculation of the mean height the shape of the initial section and roll groove has to be known. The description of the subsequent formation of rolled profiles can be done with a method where the shape of the initial profile of each pass is modeled only on the basis of shape elements of the grooves with which the material got into contact in previous passes [3], there the change of the shape of the free surface is neglected. When one wants to take that change of shape additional to the spread into consideration a model is needed. In former times research has been done on that field [4-9]. In that time the measurement of freeform surfaces was complicated, much more than it is today. In the present work an arrangement of camera, lens and illumination is used to get a fast way to measure the freeform. Sharp images of rolled profiles are gained which then are processed to get the edge data. This data is then subdivided into regions where the material was in contact with the rolls and the free surface region. After that the free surface is approximated by different analytical functions dependent on its shape.

In the case of bigger sections 3D-data sets of hot rolled stickers are evaluated over the whole deformation zone. Therefore structured-light-scanning has been used, which is with respect to the sample preparation a much faster way to get geometrical data with acceptable accuracy.

With the approximating functions the initial cross section can be described more precise with respect to its real shape and the calculation of final rolled section can be optimized.

Calculation Methods

The approximation of the free surface data is done with polynomials of different order and the circle function. For the description of the position dependent width the Johnson-Mehl-Avrami-Kolmogorov equation is used and relations between final geometry and initial geometry as a function of rolling and geometric parameters are investigated.

Results

With the used setup of camera, lens and background illumination and a precise sample preparation, acquisition of geometric data of rolled profiles and its analysis can be done at high accuracy and with acceptable time and effort. When it comes to bigger sections the structured-light-scanning is another step ahead with respect to the necessary sample preparation when plane images of the cross section of rolled profiles are used.

For the simple irregular pass round initial section rolled on flat roll at different reductions it has been identified that the side surface almost keeps its circular shape but with decreased radii at increasing reductions.

The free side surface of investigated square and rectangular bars flat rolled can be described by polynomial of second order close to inlet plane of the roll gap and coming to higher reductions at the outlet a circle function fits better. The JMAK-equation can be used at high accuracy for the approximation of the position dependent width, where two parameters are used.

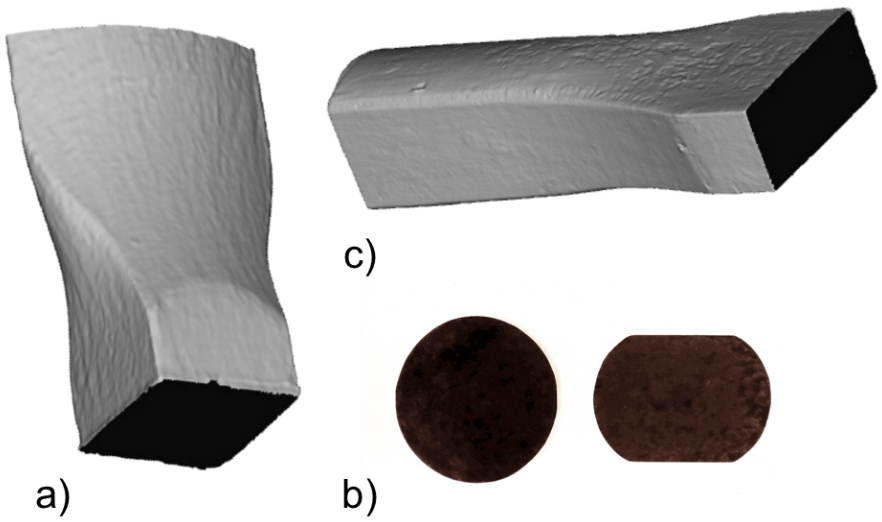

Fig.1: (a) 3D-scandata of square into oval sticker

(b) Image of round initial section rolled on flat roll

(c) 3D-scandata of rectangle rolled on flat roll

Acknowledgments

The project PIREF is financed from funds of the European Fonds for Regional Development (EFRE). The authors thank for financial support of the PIREF project with funds from EFRE.NRW under the project code EFRE-0800805.

EFRE.NRW
Investitionen in Wachstum und Beschäftigung

EUROPEAN UNION
Investing in our Future
European Regional Development Fund

References

[1] A. E. Lendl, "Rolled Bars", *Iron and Steel*, 1948.
[2] P.J. Mauk, Breitung beim Warmwalzen – Vergleich der Berechnungsmethoden - Genauigkeit - neuere Ergebnisse, Der Kalibreur, Heft 37, 1982, S. 3 - 55
[3] Christian Overhagen, *Models for Rolling of Flat and Full Sections.* Dissertation University of Duisburg-Essen, Duisburg, November 2, 2018.
[4] Heinrich Kettner, Stoff-Fluß-Untersuchungen an Stäben mit Vollquerschnitt beim Warm-Walzen auf der Flachbahn, Dissertation RWTH Aachen, Aachen, Dezember 7, 1963
[5] Werner Schiffgen, Untersuchungen über die Formänderung und den Werkstoffffluß beim Warmwalzen, Dissertation Bergakademie Clausthal, Clausthal, Juli 9, 1966
[6] Ansgar Schütza, Untersuchungen über den Formänderungsverlauf beim Warmwalzen von Stahl in einfachen Streckkalibern in Abhängigkeit von der Kaliberform und den Abmessungsverhältnissen, Dissertation RWTH Aachen, Aachen, Februar 16, 1971
[7] Christian Schlegel, Werkstoffffluß und Kontaktspannungen beim Walzen auf der Flachbahn und in ausgewählten Streckkalibern, Freiberger Forschungshefte B190, 1976, S. 7 – 59
[8] Ahmed Eassa Gami El-Nikhailly, Stoffflußmodelle für das Streckkaliberwalzen, Dissertation RWTH Aachen, Aachen, Dezember 17, 1979
[9] Artem Yusupow, Berechnung der Breitung und der Breitenform beim Warmflachwalzen von Stahl mit der oberen Schranke Methode, Freiberger Forschungshefte B343, 2008

13a Analysis of Elastic Rolling Stand Deformation and Inter-stand Tension Effects on Section Faults of Hot Rolled Wire Rod and Bars

Christian Overhagen(1), Rolf Braun(1) and Rüdiger Deike(2)

(1) Metal Forming (2) Chair for Metallurgy and Steel Production, University of Duisburg-Essen, D-47119 Duisburg, Germany
E-Mail: christian.overhagen@uni-due.de Web: www.uni-due.de/umf

Abstract

The present work aims at the mathematical modeling of the hot rolling process for steel wire rod and bars. The work is part of the PIREF project which incorporates the development of sensors, control systems and process models in order to control the dimensional accuracy in hot rolling mills for wire rod and bars. The model presented here allows the calculation of section shapes under the influence of elastic rolling stand deformations and interstand tensions.

Introduction – The model presented consists of the plant data layer and the rolling data layer.

Input information for the plant data is included in the model as a plain text file giving information of all the rolling stands, water cooling sections and distances which are present in the mill layout.

For the simulation on the rolling data layer, a fast method for the rolling process is constructed from a numerical description of the geometries of initial sections and roll grooves.

Calculation Methods – The equivalent flat pass method according to Lendl [5] is used to calculate the lateral spread of the rolling process, which is an important parameter for the evolution of section geometry in rod and bar rolling.

Stress distribution, roll force, torque and power, necessary rotational speeds of the rolling mill rolls as well as temperature and flow stress of the rolled material is calculated by utilizing a slab method approach for the equivalent flat pass. The fast slab method approach is available for both two- and three-roll rolling processes [1-3].

The exit section geometry is then calculated by making use of the given initial section shape, as well as the roll groove geometry and the calculated spread. It is fed into the next pass as an initial section.

The rolled section geometries are generally affected by an elastic feedback deformation of the rolling stand and rolls a reaction to the acting rolling force, as well as the interstand tension stresses acting in the rolled material. The interstand tensions reduce spread and therefore have a direct effect on section geometries, which is a common problem in section rolling that is addressed in the PIREF project.

Results – The elastic rolling stand feedback increases the size of the rolled product in each stand.

As the volume flux is constant throughout the mill for one time (but time-dependent), a distortion of section shapes as induced by rolling stand feedback will influence the velocity distribution along the rolling mill and therefore lead to the build-up of additional interstand tensions.

Fig. 1 shows interstand tension distributions for different rolled materials in a finishing block of a wire rod mill, where the differences originate from the different flow stresses as well as temperature-dependent spreading behavior of the different materials. To optimize the sectional accuracy for the high-spread material X8Cr17, the entry section was sized to a smaller diameter, which led to the increase of interstand tensions and the intended decrease of spread.

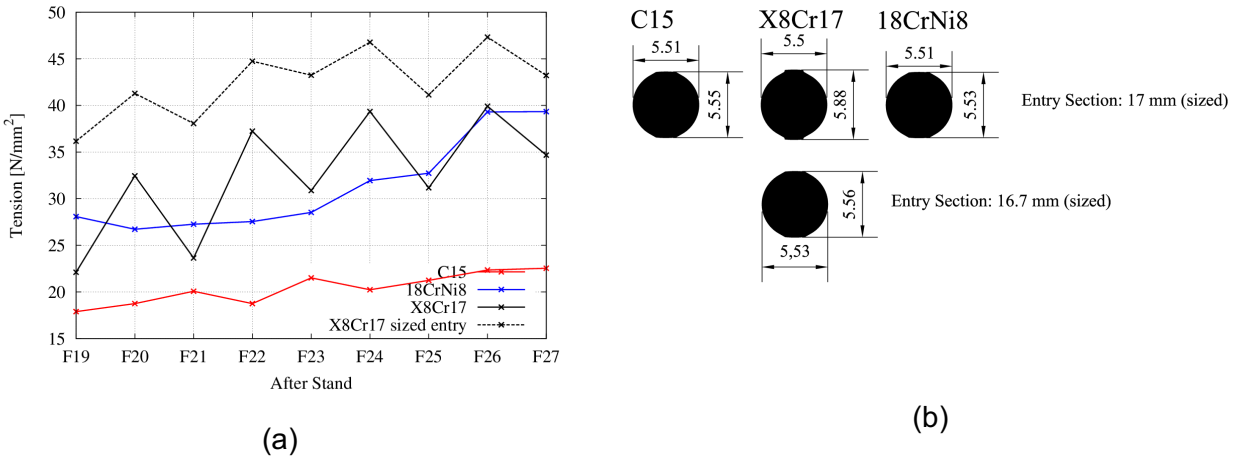

Fig.1: Calculated interstand tensions in a group-driven finishing block of a wire rod mill for different materials. Higher tensions are induced by purpose for the high-spread material X8Cr17 as to optimize sectional accuracy. (a): Tension stresses; (b): Calculated section geometry.

The model as presented here forms the metal forming basis for a control model which is developed by another working group in the PIREF project.

In order to couple the theoretical model with in-situ measurements of the cross sections and roll gaps in the rolling mill, the actual section shapes are constructed are constructed from the given roll geometry, as well as the measured cross section and rolling gap.

With help of the developed rolling model, the cross-sectional faults that can be expected from the rolling processes under elastic rolling stand feedback and interstand tensions can be investigated in. Rules for counteraction can be generated from these results to form the basis of future process control in rolling mills for wire rod and bars.

Acknowledgments – The project PIREF is financed from funds of the European Fonds for Regional Development (EFRE). The authors thank for financial support of the PIREF project with funds from EFRE.NRW under the project code EFRE-0800805.

References

[1] Ch. Overhagen and P. J. Mauk, "A New Rolling Model for Three-Roll Rolling Mills", 15th International Conference on Metal Forming 2014 (Metal Forming 2014), September 21-24, Palermo, Italy, pp. 879-886.
[2] H. Lippmann and O. Mahrenholtz, Plastomechanik der Umformung metallischer Werkstoffe. Berlin: Springer, 1967.
[3] Christian Overhagen, Models for Rolling of Flat and Full Sections. Dissertation University of Duisburg-Essen, Duisburg, November 2, 2018.
[4] Ch. Overhagen and P. J. Mauk, "Possibilities and Limitations of Free Size Rolling with Respect to Size and Temperature Variations of Different Materials", Proceedings of the Iron and Steel Technology Conference (AISTech 2015), May 4-7, Cleveland, OH, USA, pp. 3061-3071.
[5] A. E. Lendl, "Rolled Bars", Iron and Steel, 1948.

14 Non-contacting Velocity Measurement of Hot Rod and Wire Using Eddy-Current Sensors

Mario Radschun(1), Annette Jobst(1), Jörg Himmel(1) and Olfa Kanoun

(1) Institute for Measurement Engineering and Sensor Technology, University of Applied Sciences, D-45479 Mülheim an der Ruhr, Germany
E-Mail: mario.radschun@hs-ruhrwest.de Web: www.hochschule-ruhr-west.de
(2) Department of Measurements and Sensor Technology, Faculty of Electrical Engineering and Information Technology, Technische Universität Chemnitz, D-09120 Chemnitz, Germany

Abstract

Process diagnosis is an important method for improving product quality in rolling mills. In addition, the measurement of process variables such as roll gap, cross-sectional area, velocity, and volume flow of the material during production enables the implementation of model-based control concepts to improve product quality. The non-contact speed measurement of hot wire and bar is still a big challenge due to the rough environmental conditions and is solved mainly with optical measuring methods in production. The alternative measurement principle with eddy current sensors presented in this paper enables velocity measurement at locations in a rolling mill where optical measurement methods are not suitable.

Introduction: As part of the cooperative research project PIREF ("Process diagnosis and integrated control to increase the efficiency of hot rolling mills for steel bars and wire"), a measuring method for non-contact velocity measurement of quasi-continuous wire and steel bars must be developed, since commercial measuring systems cannot meet the requirements of model-based control. The most important requirements are e.g. the measurement of velocities up to 120 m/s, a measuring accuracy of better than 0.01 % and the possibility to install the measuring system directly in a rolling stand.

State of the Art: The commercial measuring instruments are typically based on optical measuring principles, such as the laser Doppler principle in [1][2], the picket fence effect in [3] and correlation of heat radiation in [4]. Unfortunately, these measuring instruments cannot meet the requirements mentioned above. Therefore, an alternative measuring method has to be developed.

Theory of operation: Ideally, a wire or bar has a perfect surface and a constant cross-sectional area over the entire rolling stock. In reality, the surface is not perfect and the cross-sectional area is not constant due to the residual eccentricity of the rolls, the non-uniform temperature during rolling and tension of the following stands. Surface inspection and measurement of the cross-sectional area [5][6] can be performed using eddy current sensors.

By modifying the cross-sectional area-measuring devices by [6] and using two eddy-current sensors at a defined distance d, the time offset Δt (Eq. 1) can be correlatively determined from the cross-sectional area and thus the speed $v(\Delta t)$ (Eq. 2) of the rolling stock.

$$\Delta t = T \cdot \Delta s \qquad (1) \qquad v(\Delta t) = \frac{d}{\Delta t} \qquad (2)$$

The correlation procedure is very robust and provides a sample shift Δs. The accuracy is mainly influenced by the time resolution (sampling rate T) and the distance d between the sensors.

Experimental results: In order to test the measuring principle, a laboratory setup was build up for simulating a quasi-continuous wire. Figure 1 shows two sensor signals which are correlated. The time offset is clearly visible and can be determined very easily and precisely. With this laboratory setup, velocities up to 10 m/s have been simulated and the relative measurement error has been determined, see Figure 2 below.

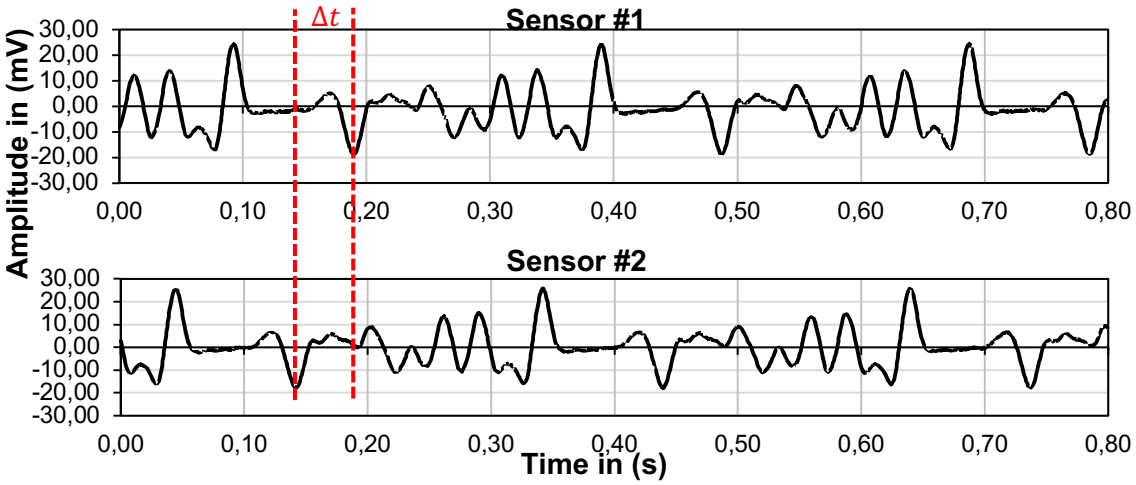

Fig.1: Voltage change caused by impedance change of two eddy-current sensors. The red lines clearly show the time offset.

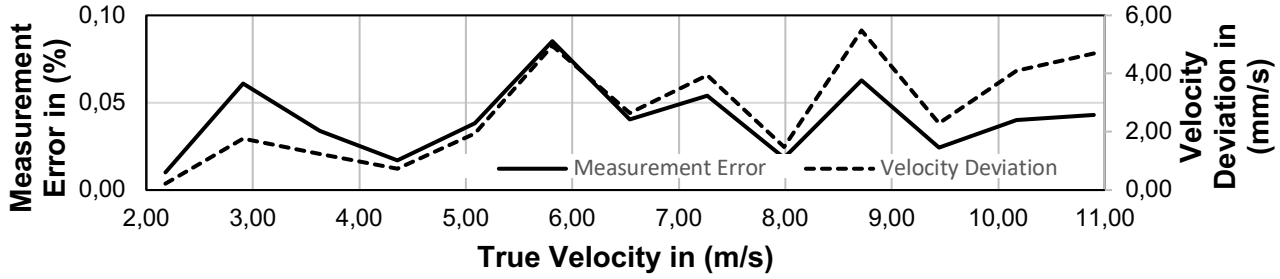

Fig.2: Measurement error and velocity deviation compared to true velocity.

Conclusion and Outlook: Measurements show very good results with two eddy-current sensors. In theory, this functional principle and the measuring system meet the requirements of the research project. In the next step, a modified cross-sectional area-measuring device by [6] will be used as a basic platform to test the functional principle in field tests and to verify the applicability.

Acknowledgment: The PIREF research project is funded by the European Regional Development Fund (EFRE) from 2017 to 2020.

EUROPEAN UNION
Investing in our Future
European Regional
Development Fund

EFRE.NRW
Investitionen in Wachstum
und Beschäftigung

References

[1] Stuart Manser, BETA LaserMike, "Non-Contact, Laser-Based Technology for Accurately Measuring the Length and Speed of Product in Web Coating and Lamination", AIMCAL Fall Technical Conference, 2011.
[2] Peter M. Nawfel, Polytec GmbH, "Optimizing Strip Speed Measurement for Mass Flow-AGC & Elongation Control with Laser Surface Velocimeters", 2018.
[3] MICRO-EPSILON Optronic GmbH, "Sensor systems for process optimization in rolling mills and strip finishing lines - Brochure", https://www.bestech.com.au/wp-content/uploads/cat-ascospeed-sensorsystems.pdf
[4] Danieli Automation, „SM3000 Optical Speed Meter Family - Brochure", http://www.dca.it/media/download/brochure-sm3000.pdf
[5] Danieli Automation, „HiSECTION Section gauge system for metal industry - Brochure", http://www.dca.it/media/download/brochure-hisection.pdf
[6] J. Weidenmüller, "Optimization of Encircling Eddy Current Sensors for Online Monitoring of Hot Rolled Round Steel Bars", 2014. ISBN: 9783844027945

15 Experimental Setup for Examination of the Roll Gap during a Rolling Process

Annette Jobst(1), Mario Radschun(1), Jörg Himmel(1) and Olfa Kanoun(2)

(1) Institute for Measurement Engineering and Sensor Technology, University of Applied Sciences, D-45479 Mülheim an der Ruhr, Germany
(2) Department of Measurements and Sensor Technology, Faculty of Electrical Engineering and Information Technology, Technische Universität Chemnitz, D-09120 Chemnitz, Germany
E-Mail: annette.jobst@hs-ruhrwest.de Web: www.hochschule-ruhr-west.de

Abstract

In the field of producing hot-rolled steel bars and wires, hot rolling mills are incomplete or barely equipped with measuring technology for recording relevant process parameters. Therefore, there is a big potential to increase product quality and to decrease costs and scrap by improving process control establishing new sensor systems. One of these crucial parameters is the roll gap, which is investigated as part of the research project PIREF. In this paper an experimental setup for examining the roll gap during a rolling process is presented and based on these results different sensor arrangements are discussed.

Introduction: Hot-rolled bars and wires are among the most important steel products and demand for steel in general has been growing steadily for decades. In order to reduce costs and scrap, it is necessary to optimize process diagnostics, to which we would like to contribute with our cooperative research project PIREF ("Process diagnosis and integrated control for increasing the efficiency of hot rolling mills for steel bars and wire"). Therefore, an in-situ measuring of different influencing parameters has to be implemented. In our project, we focus on three of these parameters: The velocity of the hot rod [1], the volume flow rate and the roll gap.

State of the Art: The roll gap is one of the most important parameters defining the quality and dimensional accuracy of the hot-rolled steel rod and it varies during the rolling process due to the forces applied by the steel rod to the rolling stand. Typically, the roll gap is set to a fixed value before starting rolling and the position change of the rolls is not taken into account. Since the roll gap is such crucial, there are several studies with focus on the effect of roll gap adjustment and of roll wear on the cross sectional shape of the rod, but there is no launched sensor system for in-situ measuring of the roll gap during production on the market [2] [3].

Theory of operation: For investigating

the roll gap a first experimental setup, a three-roll bending machine, was build up [4]. In the next step, this setup has been transformed to a rolling stand with two rolls, one driven roll and one drag roll.

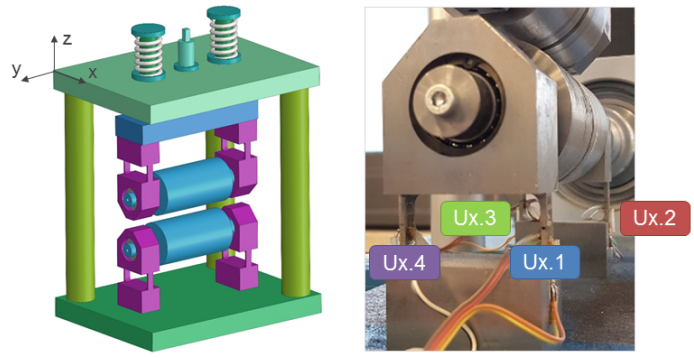

Fig.1: Experimental setup: (a) model of the rolling stand and (b) lower roll with strain gauges (with denomination of the bridge voltages)

This rolling stand is equipped with strain gauges forming eight measuring bridges (four per roll). The strain gauges are placed on the webs of the bearing blocks in order to record the position change of both rolls. To adjust the roll gap, the upper roll can be moved in the z-direction by a trapezoidal spindle. For the measurements, a 6 mm aluminium rod was positioned between the rolls and then the roll gap was reduced in size.

The bar was rolled over its entire length in x-direction. Then the roll gap was reduced once again and the rod was rolled in negative x-direction.

Experimental results: Figure 2 shows the measuring results. At first (100 s), the roll gap is reduced and all voltages rise. Since the rod is not rolled centered the voltages U1.2, U1.3, U2.2 and U2.3 are higher. Then the first rolling process starts (155

s) and a difference between U1.2 and U1.3 or rather U1.1 and U1.4 appears. This is caused by the deflection of the roll. For the next rolling process, the difference between the voltages is inverted since the roll is deflected in the opposite direction.

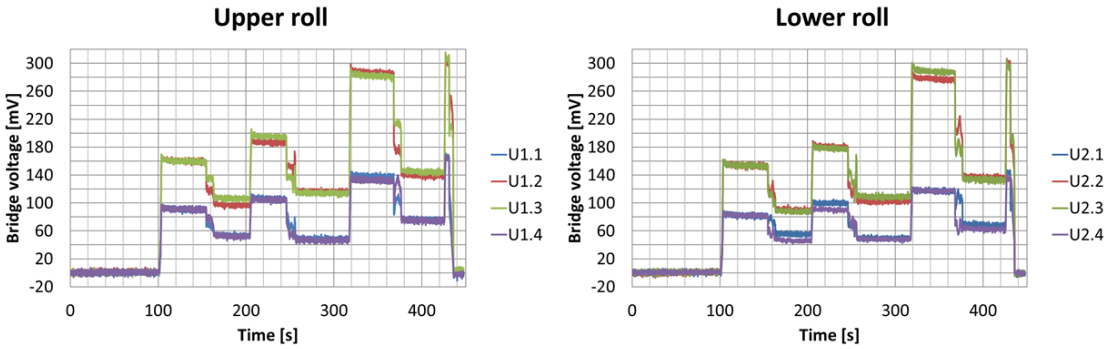

Fig.2: Voltage curve of the measuring bridges during a rolling process for upper and lower roll

Conclusion and Outlook: This study demonstrates that the roll gap is not only enlarged in z-direction by the rolling stock, but that the rolls are also deflected in the x-direction respectively negative x-direction. The deflection of the rolls depends on the structure of the roll stand, e.g. driven rolls versus drag rolls, but can consequently also be influenced by the tensile and compressive forces between the stands of a rolling mill. Therefore, a possible sensor system must detect the roll gap change in the form of a vector size. Figure 3 shows two conceivable sensor arrangements.

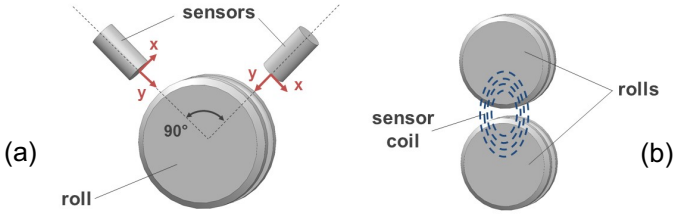

Fig.3: Sensor arrangements: (a) two sensor coils at 90° angle (b) elongate flat coil in front of the front faces of the rolls

Acknowledgment: The PIREF research project is funded by the European Regional Development Fund (EFRE) from 2017 to 2020.

EUROPEAN UNION
Investing in our Future
European Regional
Development Fund

EFRE.NRW
Investitionen in Wachstum
und Beschäftigung

References

[1] M. Radschun, A. Jobst, O. Kanoun and J. Himmel, “Velocity Measurement in Rolling Mills Using Impedance Analysis”, International Workshop on Impedance Spectroscopy 2018, September 27-28, Chemnitz, Germany, 2018

[2] S. M. Byon and Y. Lee, "A study of roll gap adjustment due to roll wear in groove rolling: experiment and modelling", *Proc. IMechE*, vol. 222, Part B, pp. 875-885, April 2008.

[3] S. M. Byon, D. H. Na and Y. Lee, “Effect of roll gap adjustment on exit cross sectional shape in groove rolling – Experiment and FE analysis”, Journal of Materials Technology, vol. 209, pp. 4465-4470, 2009

[4] A. Jobst, M. Radschun, O. Kanoun and J. Himmel, “Roll Gap Measurement in Rolling Mills Using Impedance Analysis”, International Workshop on Impedance Spectroscopy 2018, September 27-28, Chemnitz, Germany, 2018

16 Implementation and setup of a Rapid Control Prototyping system providing an environment for systematic model refinement techniques together with a plant simulator

Marc-Simon Schäfer[(1)], Omar Gamal[(1)], Jürgen Wahrburg[(1)], and Hubert Roth[(1)]

[(1)] *Institute for Automation and Control, Faculty of Electrical Engineering and Computer Sciences, University of Siegen, D-57076 Siegen, Germany*
E-Mail: marc-simon.schaefer@uni-siegen.de Web: https://www.eti.uni-siegen.de/rst/

Introduction

In this work, we present our developments in the context of the EU funded project *PIREF* with its aim to improve the efficiency of hot rolling mills for steel bars and wires. Usually, a hot rolling mill consists of multiple stands in which the material is formed to the desired output shape and dimension. Modeling of rolling mills is a common task and has been done over years . Most of the works available are related to flat products, whereas modeling of the bar and wire process is only partly done. Despite the general structure of rolling mills is considerably similar, the usage of sensors as well as the mathematical description of the forming process is noticeably different. Validation of the bar and wire process models (i.e. base equations and parameters) are of great importance for system analysis and control design, and thus a known environment during the validation process is preferable. In the PIREF project, a single test stand in two-roll configuration is available, which is used for getting a deeper insight into the forming process.

For these tests, we developed a solution that incorporates the data acquisition, interface for sensors and additionally a model-based system to run dynamic models in parallel to the process or simulate a rolling environment if no plant is accessible. This infrastructure is deployed in a real-time environment.

Setup and Methods: The development of more accurate models requires the automation of the testing workflow. General steps during that procedure are: test preparation, measurement and data acquisition, model comparison and model adaption. That well-known setup leads to a split of the modeling and the measurement steps as well as their respective hardware platforms. The data acquisition is often based on standalone devices or computer-based extension cards. On the other hand, modeling is usually done with the help of high-level programming tools, like MATLAB and Simulink. Tools for automated code generation have been developed to allow fast deployment of production code to real-time computers and were applied in different fields . Code generation helps to overcome the above-mentioned separation of designs and additionally yields to the possibility to get a real-time system response of the process model. Moreover, it provides the ability to use online estimators and filters, which can predict the behavior based on current measurements and states. It can be also used for implementation of control algorithms. As a side effect, data can be recorded for offline usage, which covers the traditional data acquisition task.

This system can be used in our application to simulate an entire roll stand. Thus, user-defined roll scenarios can be applied instead of using measurement data. Furthermore, developed controllers and estimators can be tested without the need of access to the rolling equipment. This design is also known as a Hardware-in-the-loop (HIL) setup . By following these application requirements, an RCP (Rapid Control Prototyping) system was selected and commissioned.

For the data acquisition, an electrical interface for the single-test stand in our partner's laboratory was developed. It provides the electrical connections to the different sensors and protection circuits for fault cases. Some of the sensors require a data preprocessing, which is done with additional microprocessors (Arduino and RaspberryPi) and connected to the RCP system over the network via UDP (1).

Formatierung im grünen Kasten noch nicht vertical zentriert

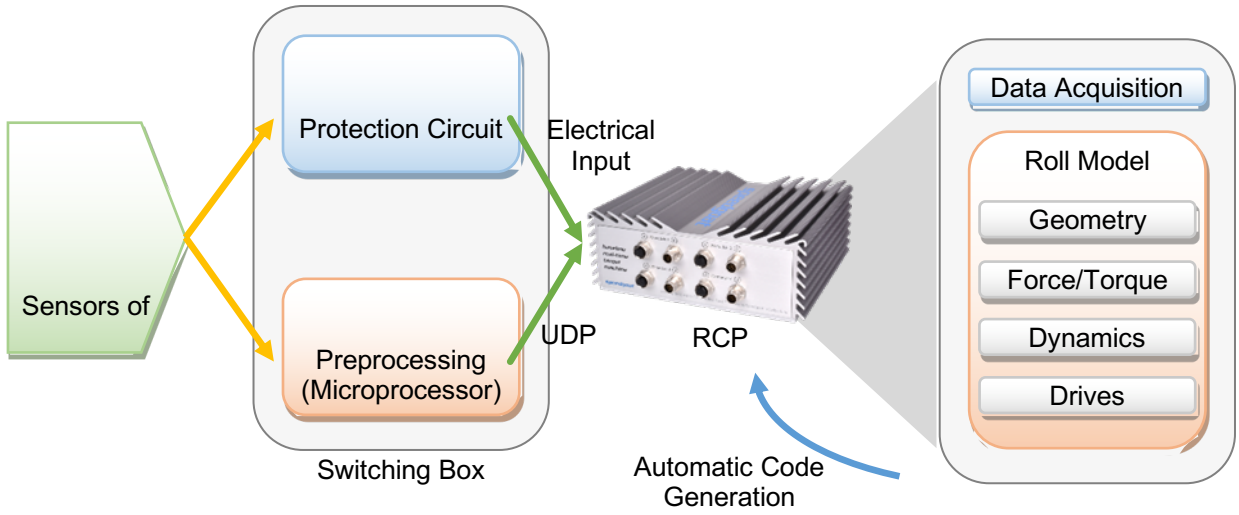

The code for the real-time system consists of two main parts: *data acquisition* and *roll model*. The data acquisition reads and optionally filters the signals and stores it to the drive. For future experiments, a roll model for this single-stand setup was implemented. After implementation of these above shown sub-models, a validation of each block was carried out in simulation on the development computer. Thereby the functionality of the code was confirmed. By changing the target platform from development computer to the RCP system, the code however required additional adaptions, because not all functions provided for the full MATLAB usage are useable for automatic code generation. In addition, the simulation configuration was adapted to suit the requirements of the RCP system.

In summary, a stand-alone solution for data acquisition combined with a dynamic model for a single-stand setup was implemented. Within these models, the crucial, partly unknown parameters are directly accessible so that these results can be used in our partner's future experiments. Thereby the adaptions can be implemented directly in a high-level language and automatically deployed on the RCP system. Different scenarios, material properties, and process information are easily interchangeable. If no plant is available, the reference values of the same system can be connected to control algorithms to test different control strategies. That leads to a seamless combination between model refinement and control design.

Acknowledgment: The PIREF research project is funded by the European Regional Development Fund (EFRE) from 2017 to 2020.

References

[1] Y. Fang-chen, Z. Dian-hua and Z. Yu-cheng, „Dynamic modeling and rolling data analysis of the tandem hot rolling process," SIMULATION, vol. 93, no. 4, pp. 307–321, 2017.
[2] O. Grieshofer, K. Mayrhofer and K. Zeman, „Mechatronische Modellierung und Simulation der Dynamik von Walzanlagen," e & i Elektrotechnik und Informationstechnik, vol. 121, no. 9, pp. 325–331, 2004.
[3] S. K. Yildiz, J. F. Forbes, B. Huang, Y. Zhang, F. Wang, V. Vaculik and M. Dudzic, „Dynamic modelling and simulation of a hot strip finishing mill," Applied Mathematical Modelling, vol. 33, no. 7, pp. 3208–3225, 2009.
[4] W. Wu, Model-based design for effective control system development, Hershey, Pennsylvania (701 E. Chocolate Avenue, Hershey, PA 17033, USA): IGI Global, 2017.
[5] A. Mutahir, Z. Gao, H. Ali, H. Zaman, A. Ashraf and B. Sun, „Rapid Control Prototyping Based Design of Buck Converter Using RTW/ MATLAB," [Piscataway, New Jersey], IEEE, 2018, pp. 506–511.
[6] D. Erdenechimeg, „Model-based design using Matlab/LabView in industrial automation," Piscataway, NJ, IEEE, 2016, pp. 549–552.
[7] D. Abel and A. Bollig, Rapid Control Prototyping, Berlin, Heidelberg: Springer-Verlag Berlin Heidelberg, 2006.

17 Development of a dynamic indentation device

Egorov Roman[(1)], Kuzmichev Mikhail[(1)] and Fedorov Aleksey[(1)]

[(1)] Lab Sensorics, Faculty of Control Systems and Robotics, ITMO University, RF- 197101 ITMO University, Russia
E-Mail: roman1465@yandex.ru Web: https://en.itmo.ru/en/, https://etu.ru/de/universitaet/

Abstract

The research considers the development of a measuring block for a prototype of a dynamic indentation device. Measuring data at the output of the hardware block of the device are subjected to algorithmic processing.

The model of shock contact interaction by finite element method has been developed to verify the algorithm operation and to derive the requirements (angle, material thickness, etc.) for the device. The model is made in axisymmetric statement for the material with elastic-plastic behavior and rigid hemisphere, moving at a constant speed at the moment of contact.

The algorithm is implemented in the MATLAB computing environment. The results of algorithmic processing are compared with the output data of the analogue of the developed device and the results of computer modeling.

Subtitle: One of the indicators of quality of any material is its mechanical characteristics. The control of physical and mechanical characteristics of materials is an inalienable operation in the manufacture of products.

In the conditions of modern production, specimenless nondestructive control becomes important in the industry, including the control in hard-to-reach places.

One of the methods of nondestructive testing, which has great versatility and allows to conduct nondestructive tests of a wide class of materials: from metals to low-module polymers and composites, is the method of dynamic indentation (DI). The development of computational systems and element base allows to design portable measuring devices, which are not inferior in accuracy to stationary devices of instrument indentation.

The task of developing a prototype of a portable device to check the mechanical characteristics of the product or its components by means of DI is relevant.

The purpose of this work is to improve the accuracy of determining the mechanical characteristics of metals by dynamic indentation.

In order to achieve this goal, the following tasks have been defined and resolved:

development of a computer model of the dynamic identification process.

development of the processing algorithm

development of a radio electronic measuring module.

The model (Figure 1) is made in axisymmetric statement for the material with elastic-plastic behavior and rigid hemisphere, moving at a constant speed at the moment of contact. The resulting model allows you to derive requirements for the design of the device and also to define restrictions on testing objects and materials.

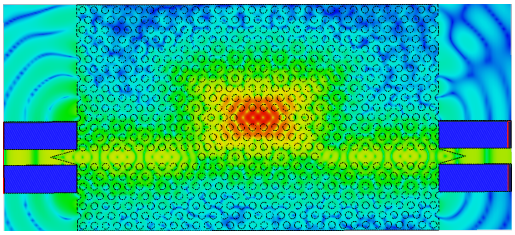

Figure 1. The result of simulation of impact-contact interaction.

The hardware of the prototype device consists of a measuring unit with a high-speed analog-digital converter (Figure 2), a primary transducer, a FPGA developer board and a wireless interface module for transmitting data to the computer.

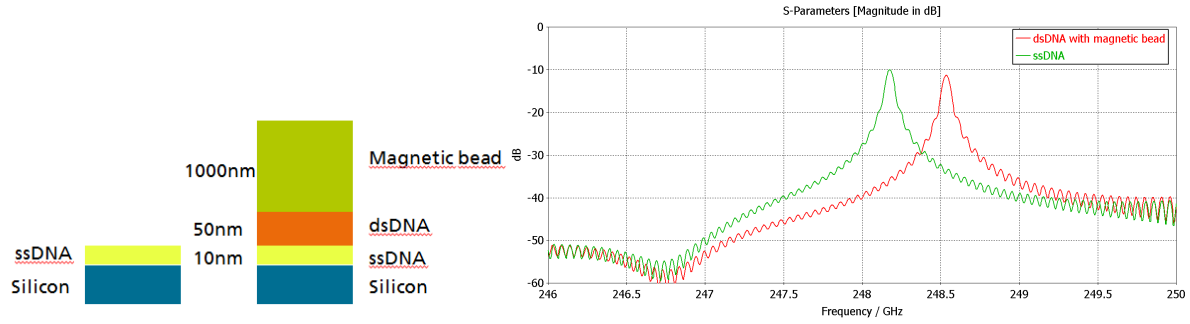

Figure 2. Data acquisition board.

Algorithmic processing and presentation of the results is performed on the computer. The core of algorithmic processing is performed in the MATLAB computing environment.

The results obtained in the course of this study will be introduced in the development of the dynamic indentation device.

References

[1] Francisco Diego Lima Moreira, Maurício Nunes Kleinberg, Hemerson Furtado Arruda, Francisco Nélio Costa Freitas, Marcelo Monteiro Valente Parente, Victor Hugo Costa de Albuquerque, Pedro Pedrosa Rebouças Filho. A novel Vickers hardness measurement technique based on Adaptive Balloon Active Contour Method // Expert Systems with Applications. 2016. V. 45. P. 294-306.

[2] Kren 'A.P. Control of physical and mathematical properties and crack resistance of nonmetallic constructional materials by indentation methods: the thesis abstract for the degree of Doctor of Technical Sciences: specialty 05.11.13. scientific institution "Institute of Applied Physics of the National Academy of Sciences of Belarus".

[3] Rabtsevich AV, Matsulevich OV New possibilities of the dynamic indentation method in the Impulse-2M device // Institute of Applied Physics of the National Academy of Sciences of Belarus. 2006. [5] The EM simulator *openEMS* based on EC-FDTD method: http://openems.de (accessed Dec. 20, 2015).

18 Assessment of Energy Efficiency and Productivity of CNC Machining Processes

Lorena C Moreira [(1)], Martin Zwiernik[(2)], Weidong Li[(1)], Michael E Fitzpatrick[(1)], Xin Lu [(1)]

[(1)] *Future Transport and Cities, Faculty of Engineering, Environment and Computing, Coventry University, CV1 5FB, Coventry, United Kingdom*
[(2)] *FORMTEC Engineering Services GmbH, 46244 Bottrop Germany*
E-Mail: moreiral@uni.coventry.ac.uk

Abstract

Computer Numerically Controlled (CNC) machines are the base energy consuming devices in manufacturing systems. At utmost concern, the energy efficiency of CNC machining processes is a challenging goal across the industry, government and academia. Feed rate is one of the machining process parameters defined during the process planning (CAPP) which greatly impacts on the machining performance (*i.e.*, productivity and energy efficiency). Hence, the performance of two machining strategies: i) the feed rate being traditionally defined by the machinists based on experience and tooling handbook, ii) the feed rate being defined by an optimisation method, when producing a multi-feature part design will be analysed and compared. For that, several experimental trials are carried out for data collection of the energy consumption and machining time using different machine tools. The results reveal that drilling and counter boring features represent the least energy-efficient features in both strategies, in addition, the amount of energy per machining state (*e.g.*, basic, actual cutting, standby, coolant) highly depends on the machine tool, where the amount of non-productive energy is greater on the more powerful machine. Also, the machining strategy using the optimised feed rates is more energy-efficient and productive when compared to the traditional processes, however, such improvements are highly affected by the machine tool capabilities. Such effects are further analysed, quantified and discussed.

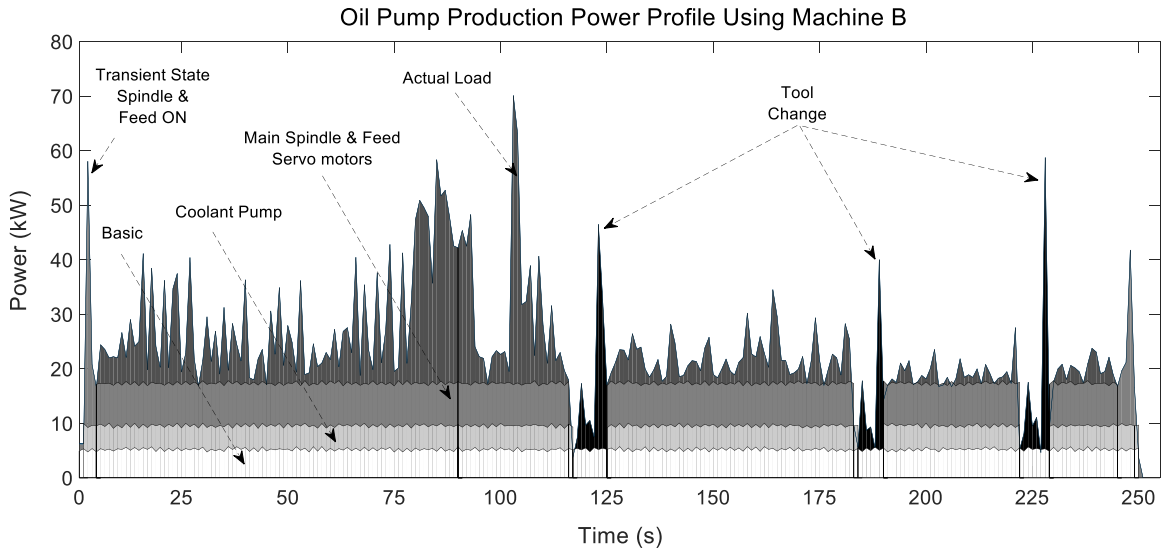

Fig.1: Power consumption profile of the traditional machining process to produce one multi-feature part design using machine tool Haas VF3 (Machine B).

Manufacturing is the backbone of economies and industrialised nations [1]. In the recent years, the total energy consumed by the manufacturing sector, equivalent to 41% of the global demand [2] and 38% of global CO2 emissions [3, 4], has become a concern due to the rises in energy price, environmental taxes and CO_2 emissions reduction agreements. Therefore, to enhance the energy efficiency of manufacturing processes is the prime target of industries and governments globally.

CNC machining is one of the most widely-deployed activities, which are well-known as the major energy consuming activities in factories' shop floors [5]. The high amount of energy demanded by the CNC machines was studied in [6], which showed that one CNC machine with main power of vector drive 30 HP operating over a year will emit the same amount of CO_2 of 61 SUV cars. Based on the great impact of CNC machines on the total energy consumed in factories, it is of paramount importance to develop more energy-efficient CNC machines and machining processes to achieve the goal of energy-efficient manufacturing.

Due to the complexity and variety of machining processes planning and CNC machines' capabilities, it is challenging to develop effective approaches to energy-efficient CNC machining, for this reason, there are still knowledge gaps that need to be fulfilled [7].

Hence, this lecturer will present a critical investigative study of the effects that process planning and CNC machine capabilities will have on the energy and productivity to produce a multi-features part for the automotive industry. Several experimental trials have been carried out using an aluminium alloy (Al6092) workpiece material. Traditional and optimised process planning (by employing a feed rates optimisation method), will be performed in CNC machines of different capabilities, monitored by a smart sensors network for data collection. A newly component level analysis is proposed which will embrace knowledge on the energy of several milling operations (*e.g.*, profiling, counter boring, drilling, face milling.). Accordingly, the investigations will study the impacts of process planning and CNC machine capabilities at the component, process and machine levels. In addition, a case study will be presented where a simplistic-smarter job scheduling is formulated considering the requirements of energy and time by the available CNC machines. Then, the Genetic algorithm (GA) will be used to solve the optimisation problem so as to assess the impacts in energy and productivity savings at the system level. The results will support the recommendations for further research to improve the energy efficiency machining processes and CNC machine selection.

This lecturer contributes four key points, as follows:

Assess the energy efficiency of specific milling operations to produce a multiple-features part (to support the development of new strategies and methods to energy-efficient CNC machining at the component level).

A feed rate optimisation method for machining time reduction is presented to support the analysis of the impacts of CNC machine capabilities on the effectiveness of optimisation approaches (, considering energy-efficiency and productivity at the process level).

Quantify the impacts of CNC machine types on the total energy consumption and productivity at the machine level (to support critical assessment of the energy consumption, energy efficiency and productivity).

References

[1] Rao, R. Venkata, "Advanced Modelling and Optimization of Manufacturing Processes". London, 2011.
[2] Edem, I. F. (2016). Energy Modelling for Machine Tool Axis and Toolpaths. This is the title of a PhD thesis. Dissertation University of Manchester, Manchester, 2016.
[3] Moreira L C, Li W D, Fitzpatrick M E, Lu X, "Research on energy consumption and energy efficiency of machine tools: a comprehensive survey". *Int. J. Nanomanuf.*, vol 14, no 2, pp. 140-164, February 2018.
[4] BP Energy Outlook 2035: http://bp.com/energyoutlook/ (accessed Feb. 07, 2019).
[5] Liu, F., Wang, Q., and Liu, G., "Content Architecture and Future Trends of Energy Efficiency Research on Machining Systems". *Chin J Mech Eng.,* vol. 49, no 19, pp. 87-94, 2013.
[6] Gutowski, T., 2013. Machining. http://web.mit.edu/2.810/www/lecture09/4.pdf (accessed March 20, 2019).
[7] Tao, P., & Xun, X. (2012). The State of the Art in Energy Consumption Model – The Key to Sustainable Machining. *Applied Mechanics and Materials*, vol. *232*, pp. 592–599, November 2012.

19 A quantitative assessment of remote-controlled telerobotic ultrasound measurement feasibility under Artificial Gravity

Timo Frett (1), Michael Arz (1), Guido Petrat (1), Ruth Hemmersbach (1), Carole Leguy (1, 2)

(1) German Aerospace Center (DLR e.V.) Institute of Aerospace Medicine D-51147 Cologne , Germany
(2) Ruhr West University of Applied Science Institute of Measuring and Sensor Technology
D-45479 Mühlheim a.d. Ruhr, Germany
E-Mail: Timo.frett@dlr.de Web: www.dlr.de/me

Abstract

Artificial Gravity generated by Short Arm Human Centrifuges is a promising multi-system countermeasure for physiological deconditioning during long duration space flights [1, 2]. Nevertheless cardiovascular responses to a steep gravity gradient are poorly understood. A robotic ultrasound device has been installed on a Short Arm Human Centrifuge to gain deeper knowledge of cardiovascular reactions during centrifugation. A feasibility study was conducted to define the use capabilities of such a novel method.

The objective of this study is to estimate the reproducibility and accuracy of remotely controlled vascular ultrasound assessment under centrifugation by assessing peripheral vascular diameter and wall distension.

Four repeated centrifugation runs of 5 minutes, with 2.4 g at feet level, have been performed including a 15 min rest between each runs for a group of 8 healthy male volunteers. Finger blood pressure and ECG have been continuously recorded. Alternatively, vascular diameter and distention were assessed for the common carotid artery (CCA) and the femoral artery by ultrasound imaging using a 10 MHz linear array probe (Mylab1, Esaote). Ultrasound measurements were consecutively performed: a) by an expert user in hand-held mode, b) using the robotic arm without centrifugation as baseline and c) using the robotic arm during centrifugation. Vascular responses were compared between baseline and under centrifugation. Inter-, intra-registration and group variability [3] have been assessed for hand-held and remotely controlled examination.

The results show that intra-measurement variability is not increased between hand-held and remotely controlled measurements (125 and 103 μm) for the carotid artery. No significant differences were obtained between femoral diameter measured by hand and using the remote arm (7.2±0.6 and 7.2±0.3mm p=0.85). However a significant decrease in diameter could be measured during centrifugation (6.3±0.5 ($p<0.01$)), that correspond to the expected physiological response to hypergravity. The diameter of the CCA decreased between hand-held and robotic measurements (7.1±0.2 and 6.9±0.3mm (p=0.04)).

Conclusion

Arterial wall dynamics can be assessed accurately for the CCA and femoral artery during centrifugation using a remote-controlled telerobotic ultrasound measurement system. However, some bias are observed for the CCA suggesting a too high pressure applied to the artery from the robotic-arm at the neck level. We suggest that a pressure contact feedback control should be used to reduce this measurement inaccuracy for the carotid.

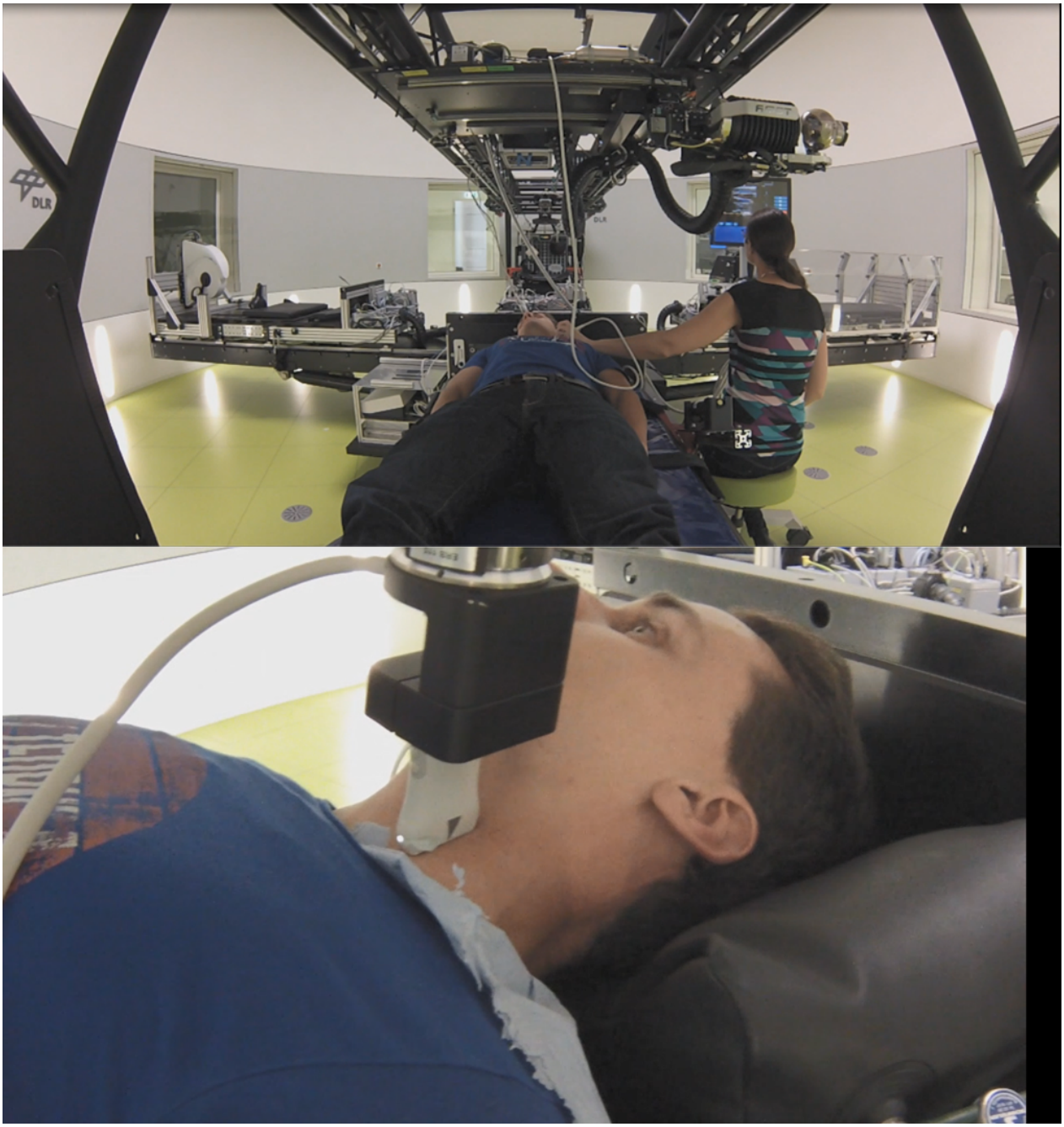

Fig.1: Top: Assessment of the carotid artery diameter using performed by an expert user in hand-held mode. Bottom: Assessment of the carotid artery diameter using the remote-controlled telerobotic arm.

References

[1] Clément, G. and A. Bukley, Artificial Gravity. Vol. 20. 2007: Springer Science & Business Media. [2] A. Author, B. Author and C. Author, "Proposal of a unique theory," *21th Annual Meeting of the International Society for Magnetic Resonance in Medicine (ISMRM 2013)*, April 20-26, Salt Lake City, UT, USA, Session on Novel RF Coils, pp. 2775, 2013.

[2] Frett, T., et al., DLR-AG Facilities & Research Plans, in International Workshop on Research and Operational Considerations for Artificial Gravity Countermeasures. 2014: Kalifornien, USA.

[3] C.A.D. Leguy, E.M.H. Bosboom, A.P.G Hoeks , F.N. van de Vosse, Model based assessment of dynamic arterial blood volume flow from ultrasound measurements, Medical & Biological Engineering & Computing, Vol. 47, pp. 641-648, 2009.

20 Design and simulation of a photonic crystal resonator as a biosensor for point-of-care applications

Yixiong Zhao[(1)], Kunj Vora[(2)], Gerd Vom Bögel[(1)], Karsten Seidl[(3)], Jens Weidenmüller[(1)]

(1) Fraunhofer Institute for Microelectronic Circuits and Systems, D-47057, Duisburg, Germany
(2) Hochschule Anhalt, D-06366, Köthen, Germany
(3)University of Duisburg-Essen, D-47057, Duisburg, Germany
Email: yixiong.zhao@ims.fraunhofer.de

Abstract

Point-of-care (POC) devices are essential for rapid testing of samples for early diagnosis of diseases. The accuracy and the sensitivity of the POC device depend on the biosensors. Biosensors consist of a biological receptor and a signal transducer. The currently used POC devices require specialized operating personnel, long sample preparation time and high equipment costs. We aim to show a bio-sensing method using a photonic crystal (PC) resonator that would mitigate the drawbacks of the present sensing techniques. Photonic crystals consist of spatially arranged dielectric materials which creates a photonic band gap that does not allow certain frequencies of electromagnetic waves to propagate through them. PC has shown to have very high sensitivities for bio-sensing applications at optical frequencies. A PC resonator with a high Q-factor leverages this quality to detect changes in the dielectric permittivity at the surface of the crystal. As an application for bio-sensing, the surface of the crystal is prepared to immobilize a biomolecule which is selective to binding with the biomolecules present in the sample. The biomolecules in the sample are labelled with magnetic beads. The simulation results show that, with successful binding on the crystal surface, there is a shift peak resonant frequency which indicates the presence of that biomolecule and its concentration. The simulation results are explained further.

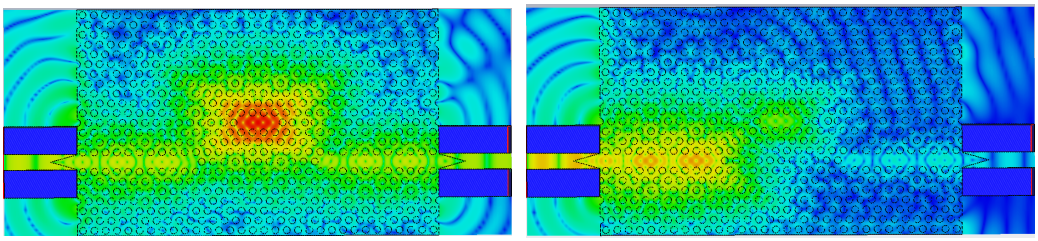

(a) (b)

Fig.1: (a) Shows the PC resonator in resonance. (b) Shows the PC resonator out of resonance

Introduction: The main factors that determine the performance of the PC resonator are the substrate material and the structure. Material properties like permittivity, mainly its contrast with the surrounding is an important factor that needs to be considered as the photonic band gap is dependent on it. High resistive silicon is a biocompatible material with a permittivity of 11.68. These properties along with high resistivity, makes it an appropriate choice for high frequency biosensors. The structure of the photonic crystal is two-dimensional. The dimensional changes in the hole structure affects the Q-factor of the resonator. Q-factor of 10^3 to 10^4 can be achieved which will increase the accuracy of the resonator. Having the facility of in-house fabrication labs, manufacturing of these sensors is possible at the institute. The PC resonator layout was simulated for single stranded DNA (ssDNA) binding with magnetic labelled double stranded DNA (dsDNA). The results depicted a frequency shift of 362MHz. These results highlight the possibility of a wide range of applications of a PC resonator as a biosensor.

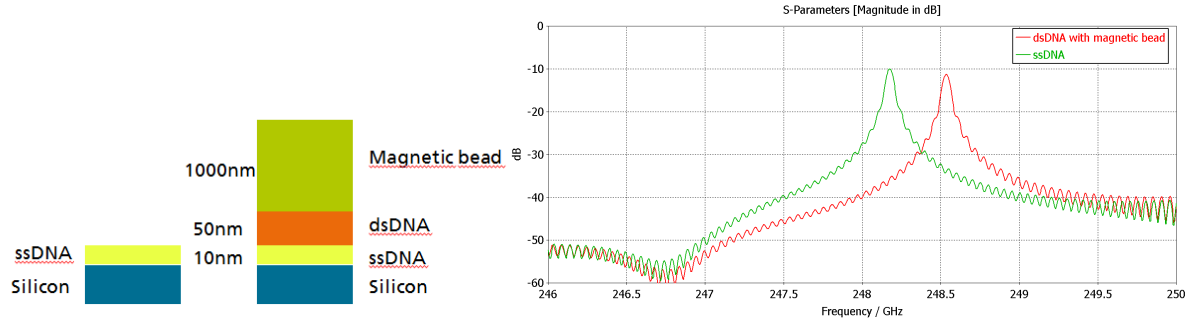

(a) (b)

Fig.2: (a) The layers of the immobilized ssDNA and the binding of the dsDNA.

(b) The simulation results showing a frequency shift.

References

[1] Jiménez-Sáez, Alejandro, Martin Schüßler, Rolf Jakoby, Christopher Krause, Frederic Meyer, and Gerd Vom Bögel. "Photonic Crystal THz High-Q Resonator for Chipless Wireless Identification." In *2018 First International Workshop on Mobile Terahertz Systems (IWMTS)*, pp. 1-5. IEEE, 2018.

[2] Inan, Hakan, Muhammet Poyraz, Fatih Inci, Mark A. Lifson, Murat Baday, Brian T.Cunningham, and Utkan Demirici.,"Photonic crystals: emerging biosensors and their promise for point-of-care applications", *Chemical society reviews 46, no. 2 (2017): 366-388.*

[3] Baker, James E., and Benjamin L. Miller. "Discrimination of "specific" and "nonspecific" binding in two-dimensional photonic crystals." Optics express 23, no. 6 (2015): 7101-7110.

21 A novel 4 camera multi-stereo tracking system for application in surgical navigation systems

Oliver Gieseler[(1)], Hubert Roth[(1,2)], and Jürgen Wahrburg[(1,2)]

(1) Center for Sensorsystems (ZESS), University of Siegen , D-57076 Siegen, Germany
(2) Institute of Control Engineering, University of Siegen, D-57076 Siegen, Germany
E-Mail: gieseler@zess.uni-siegen.de Web: www.zess.uni-siegen.de/modicas

Introduction

Since several years, optical navigation systems based on stereo cameras are used in surgical application. They are accurate up to submillimeter range [1] [2], because of high precision factory calibration before delivery, but they are expensive. Furthermore, they have to be shipped to manufacturer for recalibration in given intervals. Another disadvantage is the line of sight problem, which occurs when one camera is not able to see the reference body due to coverage. In this case, the system is not able to provide 3D data, because depth reconstruction is not possible from only one image [3].

We therefore propose a novel multi-stereo 3D digitizing system that overcomes these disadvantages.

The concept is characterized by independent, arbitrary camera mounting poses and demands easy on-site calibration procedures of the camera setup.

Materials and Methods: In this paper, we propose a novel low cost multi-stereo camera system that consists of up to four single industrial cameras with appropriate lenses. This shall replace a common stereo camera system in several applications in hip and spine surgery. For initial analysis of possible constellations and mounting poses, we used a Unity3D based simulation software. Here, the field of view of the cameras is adjustable with viewing angle parameters in horizontal and vertical direction. Later, the necessary focal length of the lens, also depending on sensor size, resolution and pixel size can be calculated from this.

In addition, we evaluated two possible mounting scenarios: Firstly, ceiling mount at an operating room lamp (Fig.1 (a)) and secondly mount on a rack near the patients head where commonly incise drape is raised up (Fig.1 (b)). In the first case up to four cameras are mounted at the rim of an operating room lamp with variable radius and height above the operating table. Cameras can be tilted from the lamp plane to the center. In the second case, two cameras are used. Their distance and height above the table as well as tilt angle from the table plane is adjustable. The fields of view of the single cameras are displayed as grey pyramids and the measurement volume of the whole system is divided into small sector cubes of 5 cm edge length. These are represented by colored spheres, where the color shows for how many single cameras the sector is visible (black = four, red = three, green= two).

We chose four Basler acA1920-155um industrial USB 3.0 monochrome cameras to build up a test hardware setup. The resolution is 1920 x 1200 pixels and the sensor size 11,3 x 7,1 mm with 5,86 μm pixels. For this setup either lenses with 6 or 8 mm focal length were taken into account. 8 mm lens usage results in image angles of 70,46° horizontal and 47,86 vertical, which results in maximum 2.12 m times 1.33 m image object size in 1.5 m distance. 6 mm lenses cause 86,56° horizontal and 61,22° vertical angle, which results in maximum visible area of 2.83 m times 1.77 m also in 1.5 m distance.

The camera system is desired to recognize and track X-markers or other pattern landmarks in visible light spectrum. For calibration of the system, we propose a two-step procedure. Intrinsic calibration of single cameras with chessboard pattern is done in lab [4]. Extrinsic calibration will be carried out on-site and is currently under investigation.

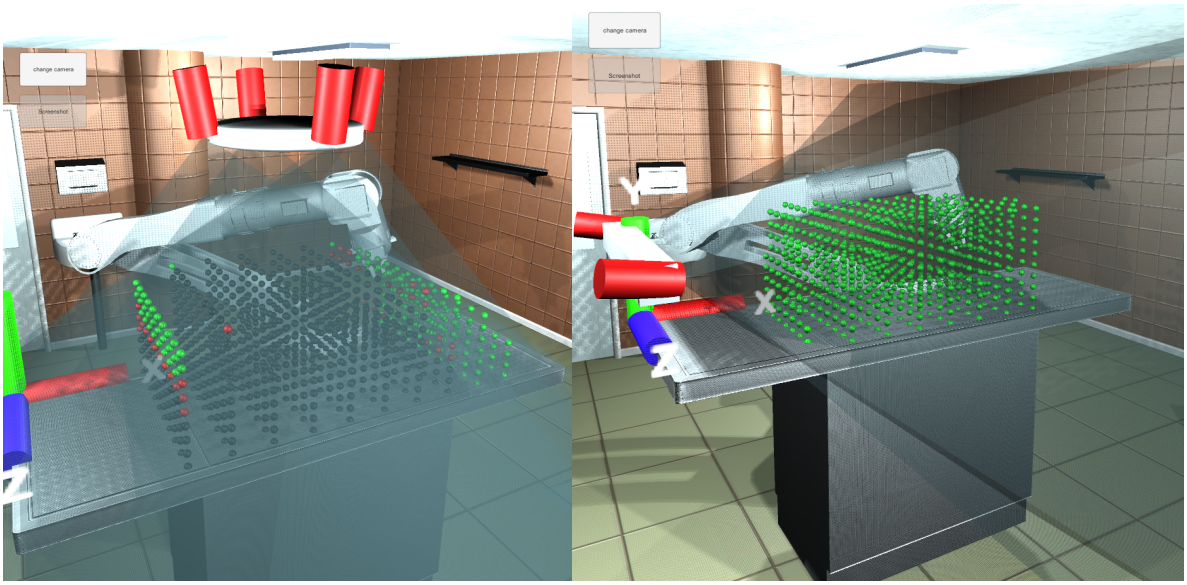

Fig.1 (a): Four cameras (red) mounted at OR-lamp with single fields of view and measurement volume, (b): two cameras at a rack at patients head with measurement volume (green)

Results and Discussion: The combination of four cameras brings the advantage that triangulation for 3D point and especially depth calculation can be carried out with six stereo camera combinations resulting of the four camera setup. This redundancy increases accuracy. In a test scenario, where cameras placed on a 30 cm lamp radius 1.5 meters above the table and tilted 10° to the center, measurement volume covered an area of 1.35 m times 0.85 m on the table. This is comparable to measurement volumes of common stereo cameras e.g. Axios CamBar B2S (0.97 m times 0.87 m in 1.5 m distance) [5] and sufficient to cover incision areas for hip or spine interventions.

If 6 mm lenses are used and focused to 1.5 meters, the sharpness range was from 0.76 to infinity in case of 8 mm lenses form 0.95 m to 3.5 m.

Mostly line of sight interruptions are caused by markers covered by hands or bodies of operating room staff. This kind of coverage is expected to be less from the ceiling view. System breakdown by coverage is less probable, because in worst case also two cameras are sufficient to create 3D data. In addition, the lamp will be aligned directly to the incision area so that the center of cameras measurement volume is also suitably aligned, automatically. Still we have to evaluate the influence of calibration inaccuracies caused by the unknown baseline distances and the proposed on-site calibration.

Acknowledgements: Part of this work is funded by the German Federal Ministry of Education and Research (program KMU-innovativ: Medizintechnik, contract number 13GW0175B)

References

[1] Northern Digital NDI, Waterloo, Ontario, Canada, https://www.ndigital.com/products/, (Polaris Cameras)
[2] Atracsys LLC, Puidoux, Switzerland, https://www.atracsys-measurement.com/, (fusionTrack Cameras)
[3] Wong, R. et al., "Current Limitations and Opportunities for Surgical Navigation", University of Toronto Medical Journal, Vol. 92(1), pp.7-9, 2014
[4] ZHANG, Z. et al.: A Flexible New Technique for Camera Calibration, IEEE Trans. Pattern Anal. Mach. Intell. 22, (11), pp.1330–1334, 2000
[5] AXIOS 3D® Services GmbH, Oldenburg, Germany, https://axios3d.de/

22 Influence of Blood Perfusion during transurethral Resection of Prostate Tissue

Tino Morgenstern(1), Daniel Richter(1), Jörg Himmel(1), Dinan Wang(2),

Institute for measurement and sensor technology, Institute of Energy System and Energy Economics
Hochschule Ruhr West, D-45479 Mülheim an der Ruhr, Germany
E-Mail: Tino.Morgenstern@hs-ruhrwest.de Web: https://www.hochschule-ruhr-west.de

Abstract

Transurethral resection of the prostate is a high frequency (HF) surgical technique for surgery of benign prostatic hyperplasia. Monopolar systems have been investigated since the 1970s [1–6], so their influence on the surgical process is well known. Ongoing studies of bipolar systems, which represent the gold standard of this technique, are focused on investigations of the electric potential distribution close to the resectoscope sheath and the calculation of the power loss density [7]. The bio-heat equation from Penne [8] and Jiji and Weinbaum [9–12] are usually used to solve the heat distribution in biological tissue. The aim of this work is to analyse the blood perfusion influence on the temperature distribution in prostate tissue during transurethral resection via numerical simulations with Finite Volume (FV) method.

Introduction: Transurethral resection of the prostate is an HF surgical technique for surgery of benign prostatic hyperplasia and can be realized by monopolar and bipolar systems [13]. In both systems, the tissue temperature depends on a high-frequency electric current which passes through the tissue. The electro-thermal transition takes place through a hot gas layer filled with plasma [14], which is surrounding the cutting element of the resectoscope. As a result the tissues in contact with the gas layer will be purposefully destroyed. From the medical point of view, the investigation of the temperature distribution is important, because the temperature distribution in the tissue is responsible for either desired tissue removal or unfavoured tissue damage [4]. For the calculation of the temperature distribution in the tissue, two different heat equations [8-12] are used. Both add a bio-heat term into the heat transfer equation which presents the blood perfusions effect with different approaches [15]. In this study we have investigated the influence of blood perfusion on the temperature distribution in prostate tissue with the bio-heat equation from Penne and Jiji and Weinbaum, respectively.

Methods: The potential high temperature caused tissue damage mainly results from the current density distribution around the surgical instruments; here we focus on bipolar resectoscopes and the associated isotonic saline solution. Looking at the power density and the electrical properties of prostate tissue, it is assumed that the electrical energy is fully converted into thermal energy. Thus, the plasma layer of the cutting element can be assumed as a heat source. Therefore, the complexity of the simulation model can be reduced to the thermal effects coupled with the fluid dynamic effect of the rinsing liquid. The simulation is two dimensional with a small region of interest (ROI) in the tissue close to the resection loop as shown in Figure (1a). The movement of the cutting element is realized with a moving heat source. The simulations have been carried out with software ANSYS FLUENT.

Results and discussion: The results of the temperature distribution based on Penne's bio-heat equation and the equation of Jiji and Weinbaum are shown in Figure 1b and Figure 1c, respectively. The cutting element velocity amounts 29 mm/s, the source temperature was set to 150 °C and selected on the tissue boundary close to the cutting element. The temperature distribution perpendicular to the tissue surface is shown in figure 1d. The results were determined with the red lines in figure 1b and 1c. The magenta line in figure 1d represents the results from Penne's bio-heat equation. The black line shows the results from the model which based on Jiji and Weinbaum's bio- heat equation. In a distance bigger than

0,4 mm from the tissue surface both models lead to the same result. Here the temperature amounts 37 °C which is the predefined surrounding tissue temperature. In conclusion the thickness of the influenced tissue is smaller than 0,4mm. The tissue with temperature above 60°C is in a distance from the tissue surface smaller than 0,125 mm for Penne's bio-heat and 0,15 mm for Jiji and Weinbaum's equation, here small difference are visible. The same results were determined for a simulation without any perfusion model. With respect to the short duration of active heat source the influence of both perfusion models to the temperature distribution in the tissue is only in a distance up to 0,15 mm visible, for bigger distances the blood perfusion can be neglected here.

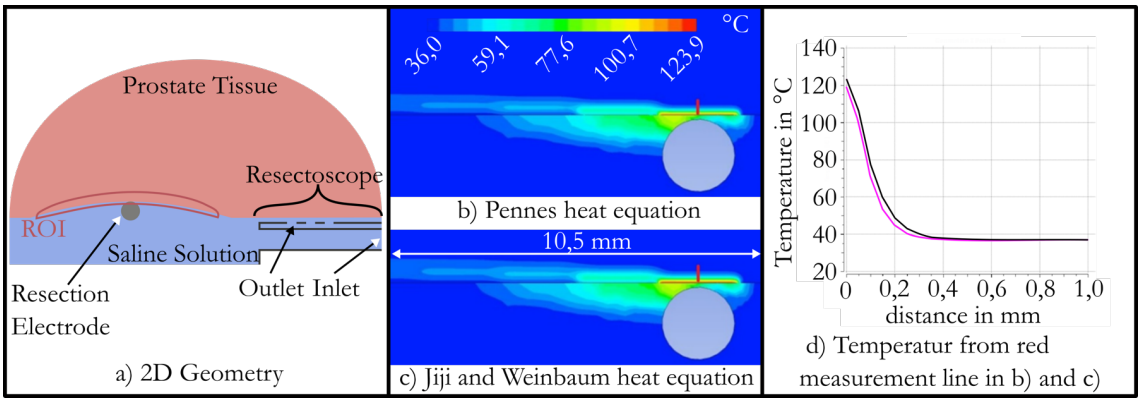

Fig.1: a) 2D Geometry of the simulation model; b) temperature distribution based on Penne's bio-heat equation; c) temperature distribution based on Jiji and Weinbaum; d) Data from red measurement line in fig 1 a) and fig 1 b)

References

[1] G. Flachenecker, K. Fastenmeier, E. SCHMIEDT, and F. EISENBERGER, "Zur Frage der kapazitiven Leckströme bei der transu- rethralen Prostataresektion bei Verwendung von Metallschäften," Urologe A 16, pp. 25–27, 1977.
[2] G. Flachenecker and K. Fastenmeier, "High Frequency Current Effects During Transurethral Resection," Journal of Urology, vol. 122, no. 3, pp. 336–341, 1979.
[3] G. Flachenecker and K. Fastenmeier, "Die transurethrale Prosta- taresektion mit Hochfrequenzströmen aus elektrotechnischer Sicht," Urologe A 15, no. 167–172, 1976.
[4] J. Rassweiler, D. Teber, R. Kuntz, and R. Hofmann, "Complications of transurethral resection of the prostate (TURP)--incidence, management, and prevention," (eng), European urology, vol. 50, no. 5, 969-79; discussion 980, 2006.
[5] J. A. Pearce, Electrosurgery. London: Chapman and Hall, 1986.
[6] P. Faul and K. Fastenmeier, "Die Rolle des Gleitmittels bei der transurethralen Elektroresektion," (ger), Der Urologe. Ausg. A, vol. 47, no. 3, pp. 326–330, 2008.
[7] C. Knopf, Methodik zur Analyse der elektrischen Feldverteilung und thermischer Vorgänge bei der bipolaren transurethralen Resektion. Zugl.: Chemnitz, Techn. Univ., Diss., 2014, 1st ed. Aachen: Shaker, 2014.
[8] H. H. Pennes, "Analysis of tissue and arterial blood temperatures in the resting human forearm. 1948," (eng), Journal of applied physiology (Bethesda, Md. : 1985), vol. 85, no. 1, pp. 5–34, 1998.
[9] L. M. Jiji, S. Weinbaum, and D. E. Lemons, "Theory and experiment for the effect of vascular microstructure on surface tissue heat transfer--Part II: Model formulation and solution," (eng), Journal of biomechanical engineering, vol. 106, no. 4, pp. 331–341, 1984.
[10] S. Weinbaum and L. M. Jiji, "A new simplified bioheat equation for the effect of blood flow on local average tissue temperature," (eng), J. Biomech. Eng., vol. 107, no. 2, pp. 131–139, 1985.
[11] S. Weinbaum and L. M. Jiji, "Discussion of papers by Wissler and Baish et al. concerning the Weinbaum-Jiji bioheat equation," (eng), Journal of biomechanical engineering, vol. 109, no. 3, pp. 234–237, 1987.
[12] S. Weinbaum, L. M. Jiji, and D. E. Lemons, "Theory and experiment for the effect of vascular microstructure on surface tissue heat transfer--Part I: Anatomical foundation and model conceptualization," (eng), Journal of biomechanical engineering, vol. 106, no. 4, pp. 321–330, 1984.
[13] R. Kramme, Ed., Medizintechnik: Verfahren - Systeme - Informationsverarbeitung, 5th ed. Berlin: Springer, 2017.
[14] R. Hofmann, Endoskopische Urologie: Atlas und Lehrbuch. Berlin, Heidelberg: Springer Medizin Verlag Heidelberg, 2005.
[15] L. Zhu, L. X. Xu, Q. He, and S. Weinbaum, "A New Fundamental Bioheat Equation for Muscle Tissue—Part II: Temperature of SAV Vessels," J. Biomech. Eng., vol. 124, no. 1, p. 121, 2002.

23 Placement of a surgical tool using a robot-mounted optical tracking system

Dominik Scarpin[(1)], Hubert Roth[(1,2)] and Jürgen Wahrburg[(1,2)]

[(1)] Center for Sensorsystems (ZESS), University of Siegen, D-57076 Siegen, Germany
(2) Institute of Control Engineering, University of Siegen, D-57076 Siegen, Germany
E-Mail; scarpin@zess.uni-siegen.de

Introduction

In this paper we evaluate a novel solution to perform tool placement and guidance during neurosurgical interventions using a robot-mounted optical tracking system. Nowadays neurosurgery is part of the standard surgical interventions performed worldwide. High precision regarding the tool placement and guidance is crucial for the success of these interventions and to avoid trauma of the surrounding tissue. Therefore the use of surgical assistant systems, especially robotic assistant systems, gains more and more importance to relieve the surgeon and to increase the accuracy and efficiency of the operation. This leads to shorter operation times and recovery periods for the patient. Additionally this opens new possibilities to perform a better treatment for the patient by being able to do more complicated operations. Using a robot-mounted tracking system near the patient will reduce the line of sight problem of stationary tracking systems but be as precise as state of the art systems.

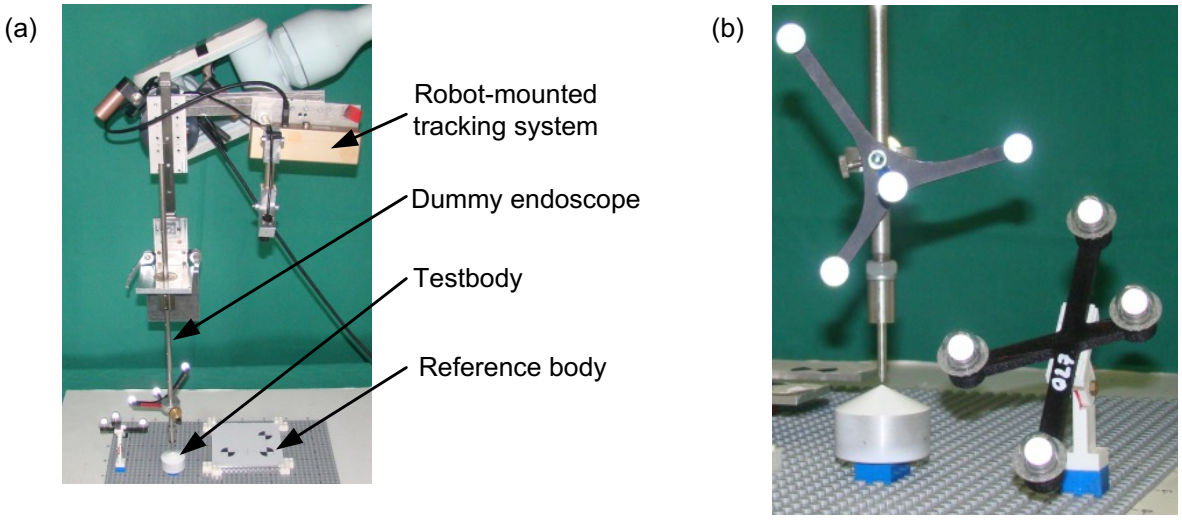

Fig.1: a) Robot-mounted tracking system with fully extended endoscope dummy after positioning is done.

b) Placed dummy endoscope with reference bodies of the second commercial tracking system used for the accuracy measurement.

Materials and Methods - For this work the Bumblebee 2, a compact and light weight optical tracking system, is connected rigidly with a dummy endoscope on a mechanical linear guidance. This combination afterwards is mounted to the flange of a robot arm by using a mechanical fast coupling (see Fig. 1 a)). The software integration of this system was done before in another project [1]. Prerequisite is a hand-eye calibration, which is needed to calculate the transformation between the coordinate systems of the robot arm and the tracking system. Thus the robot arm can be positioned, using the acquired data of the mounted tracking systems reference bodies. By using a non calibrated robot the known methods

for hand-eye calibration which require a calibrated robot arm [2][3] cannot be used. Hence, a new method for hand-eye calibration, which is suitable for non calibrated robot arms, was developed. The position of the tip of the fully extended dummy endoscope is related to the coordinate system of the robot-mounted tracking system manually with a pointer device.

As a reference point for the placement of the dummy endoscope a tip of a cone shaped testbody is used, which is attached to a LEGO plate. The tip of the testbody represents a target point on the patient's anatomy and is easy to locate with a pointer device during the accuracy measurement.

Additionally a reference body of the robot-mounted tracking system is placed on the LEGO plate in a way that the x- and y-axis of its coordinate system are aligned to the dot grid of the plate with the origin located on the center of a LEGO dot. The position of the reference point for the dummy endoscope tip placement with regard to the origin of the reference body of the robot-mounted tracking system is known from the dot spacing of the LEGO grid. With the known positions of the tip of the dummy endoscope and the reference point the new position of the robot arm is calculated and the positioning is done, supervised by the user, automatically. To avoid collision of the dummy endoscope with its surrounding, it is pulled and fixed in an upward position with the linear guidance. The placement of the dummy endoscope is done afterwards with four iterative steps to compensate the positioning error of the used robot arm. For every step the position of reference body is measured by the robot-mounted tracking system.

The accuracy of the placement is measured with a second high accurate commercial optical tracking system with an achievable measurement accuracy of approximately 0,3 mm. This system uses reference bodies with retroreflective spherical markers as seen in Fig. 1 b). It is placed on a static position on a tripod with reference bodies attached to the dummy endoscope and the LEGO plate. Before the dummy endoscopes placement is done the positions of the tip of the dummy endoscope and the reference point are measured with the second tracking system relatively to the attached reference bodies. After the placement of the dummy endoscope is finished and the linear guidance is fixed fully extended, the distance between the acquired reference point and the tip of the dummy endoscope is measured (see Fig. 1 b)). The endoscope placement is repeated 20 times with randomly chosen starting positions in which the reference body of the robot-mounted tracking system is visible. To ensure comparable results regarding accuracy the orientation of the dummy endoscope is aligned coaxial to the z-axis of the reference body on the LEGO plate during the placement.

Results and discussion - The results of the measurement give a mean deviation between the defined reference point and the tip of the dummy endoscope after the placement is finished of 0,315 mm. The attained accuracy using a robot-mounted tracking system for tool placement is within the achievable accuracy of the second tracking system. The results of these measurements are influenced by the measurement errors of both tracking systems. Also the manual acquisitions of the tip of the dummy endoscope and of the reference point on the testbody using pointer devices are influencing the result of the measurement. The results prove that this system reaches an acceptable accuracy for being used in surgical applications.

References

[1] T. Kerstein Entwicklung von Verfahren und Elementen zur optischen 3D-Lokalisierung in der computerassistierten Chirurgie, ZESS-Forschungsberichte, Band 31, 2015, ISBN: 978-3-8440-3819-4

[2] R. Y. Tsai and R. K. Lenz, "A New Technique for Fully Autonomous and Efficient 3D Robotics Hand/eye Calibration", IEEE Trans. on Robs. and Aut., vol. 5, no. 3, pp. 345–358, June 1989

[3] K. H. Strobl and G. Hirzinger, "Optimal Hand-Eye Calibration", Proceedings of the IEEE/RSJ International Conference on Intelligent Robots and Systems (IROS 2006), Beijing, China, pp. 4647-4653, October 2006

24 ASYSTED - Advanced System for Tele-Guidance in Diagnostics

Markus Lindlar(1), Mario Polaschegg(2) and Timo Frett(3)

(1) Lab for Digital Health, Department of Sleep and Human Factors, German Aerospace Center - DLR, D-51147 Cologne, Germany
(2)Department of Customization, SCOTTY Group Austria GmbH, A-8074 Raaba-Grambach, Austria
(3) Department of Gravitational Biology,Institute of Aerospace Medicine, German Aerospace Center - DLR D-51147 Cologne, Germany
E-Mail: markus.lindlar@dlr.de Web: www.dlr.de/me

Abstract

Experts in ultrasonography often are not present when needed at the Point of Care (PoC). This can lead to poor quality examination results when performed by inexperienced examiners. How can quality of examinations be increased? Remote guidance of the examiner at the POC can be realized by using video communication systems in combination with assistive technology. Tele-ultrasonography systems in combination with examiner guidance can deliver both, examination support for inexperienced examiners and high quality data for diagnostics[1].

The scenario

- An ultrasound examination is performed and the video signal is transferred to a remote medical expert via a communication platform.
- The expert assists the examiner by sending optical and acoustic signals.
- DICOM images of relevant findings are produced by the ultrasound device and transferred to the examiner system
- DICOM files are sent to the expert‘s system and diagnosis can be made (Fig .1)

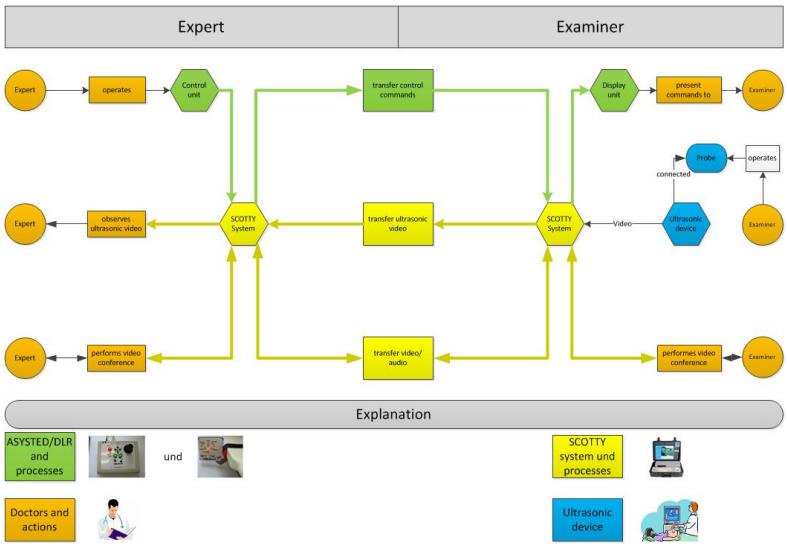

Fig.1: ASYSTED process diagram

The Tele-ultrasonography system

The SCOTTY Communication Platform (SCP) is optimized for high quality video streaming at low bandwidths over any IP -network primarily over satellite networks. The SCP transfers real time ultrasound video to an expert. In addition the system provides DICOM transfer. Using serial channels in the SCP-Teleporter software the commands of an input device can be transferred in real time between expert and examiner.).

Hypothesis

The quality of diagnostics in teleultrasonography can be increased when a less or not experienced examiner is supported in positioning the ultrasound probe by visual instructions in addition to audio guidance.

Aim of the Project

To develop a software application that combines conventional voice-guided teleultrasonograhy with visual instructions presented to the examiner.

Results

- Telesonography is a reliable tool to support examiners with a minimum experience in performing examinations
- Visual teleguidance can complete telesonography by adding visual commands to audio guidance.
- ASYSTED thus enhances precision in sound probe positioning.
- ASYSTED is a communication tool to support examinations.
- Thus it is not a medical product[2] (BfArM 2018).
- Diagnoses are made on the basis of DICOM files.

References

[1] F. Walcher et al, “Prehospital Ultrasound imaging improves management of abdominal trauma”, British Journal of Surgery 2006, 93: 238-242

[2] The European Council, “Council Directive 93/42/EEC of 14 June 1993 concerning medical devices”, (OJ L 169, 12.7.1993, p. 1)

25 Simulation of Circular Electrode for Poultry Tissue Study by Impedance Spectroscopy

Hanen Nouri[1], Shubham Mirajkar[2], and Olfa Kanoun[1]

[1] *Chair of measurement and sensor technology, Faculty of Electrical Engineering and Information Technology, TU Chemnitz, Chemnitz, Germany*
[2] *University of Applied Sciences of Karlsruhe, Karlsruhe, Germany*
E-Mail: hanen.nouri@etit.tu-chemnitz.de Web: https://www.tu-chemnitz.de/etit/messtech

Abstract

Meat high-quality assessment becomes a necessity in food industry. Various techniques are used for the quality and aging detection such as shear and compression forces as a mechanical methods, optical and electromagnetic methods. But these techniques lead to a high cost, complex, time consuming and must be carried out in laboratory by experts. Bio-impedance spectroscopy measurement technique is frequently used method for non-invasive system identification. This technique is straightforward, in-situ and cost-effective. Impedance based methods for biological tissues characterization have been of a big interest in research field for many years. Such a method provides detailed information about tissue state at low costs.

Several electrodes for bio-impedance measurement have been developed in order to get accurate and reproducible measurements. Different probes are designed for various studies in meat muscle such as shaped needle probe with four planar electrodes on its shaft [1]. In fact, such probe can reach inner tissue and it is non-invasive. Trabelsi [2] has investigated the variation of dielectric properties of chicken meat with frequency in temperature. In this study, an open ended coaxial line probe and stain-less-steel cup, where the simple is inserted, is used. Mahdi et al. [3] has developed a probe for the classification between veal and beef muscle type and the aging state of the muscle. The probe has a cylindrical geometry and consists of nine gilded needle electrodes. Such probe can solve the influence of the anisotropy and also guarantee a good contact with fibres because of needles can be inserted in meat.

Electrode Design: To ensure an accurate and precise measurement, acupuncture needles can be useful in this work for electrodes design. In fact, they are tiny, highly polished and specially can be electrically stimulated. Moreover, they can be inserted in the skin safely and without damaging the muscle tissue. The electrode's configuration is investigated with the software COMSOL Multiphysics based on the Finite Element Methods (FEM).

The geometric parameters of the phantom have a radius of 30 mm and a height of 10 mm. It has the dielectric conductivity of 0.5 S/m and dielectric permittivity of 90.The needles are composed of three main parts of 2.8 mm as a total length as shown in figure 1.

Simulation results shows the same impedance spectrum behaviour but the impedance increases when less needles are used. As shown in figure 2 (b) the impedance increases by increasing the distance between electrodes. Furthermore, the effect of different number of electrode on the behaviour of impedance is considered. Different number of needles are taken 5,9,13 and 17 needles. It can be observed that change in number of electrodes changes the behaviour of impedance towards the phantom. By taking more number of needles the contact area is increasing in increase which results a decrease in the impedance.

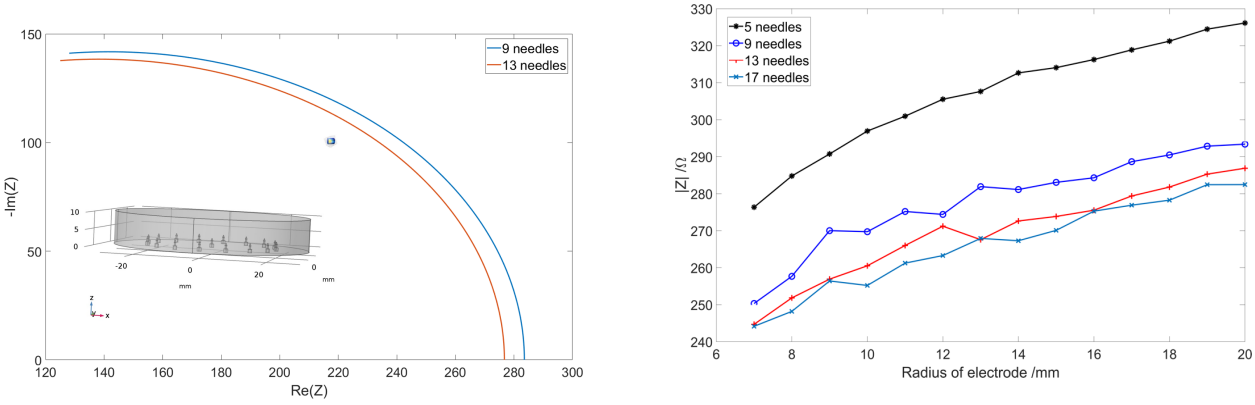

(a) (b)

Fig.2: (a) Nyquist plot from 40 Hz to 110 MHz (b) Influence of the electrode radius on the impedance

The simulation investigation of the influence of radius and number of needles was carried out with considering the phantom has the same dielectric properties of chicken meat. We can conclude that increasing the number of needles and decreasing the radius of the electrode can perform better results. More investigations can be carried out considering the influence of the length and material of inserted needles.

References

[1] Ivorra A. Bioimpedance monitoring for physicians: an overview. Centre Nacional de Microelectr_onica Biomedical Applications Group. 2003; 11:17.

[2] Trabelsi S. Variation of the dielectric properties of chicken meat with frequency and temperature. Journal of Food Measurement and Characterization. 2015; 9(3):299{304.

[3] Guermazi M, Kanoun O, Derbel N. Investigation of long time beef and veal meat behavior by bioimpedance spectroscopy for meat monitoring. IEEE Sensors Journal. 2014; 14(10):3624{3630.

26 Towards a method to identify microorganisms via Raman spectroscopy: the challenge of transferring calibrations from one device to another

Thomas Tewes, Frank Platte and Dirk Bockmühl

Faculty of Life Sciences Rhine-Waal University of Applied Sciences, D-47533 Kleve, Germany
E-Mail: Thomas-Johann.Tewes@hsrw.org Web: www.hochschule-rhein-waal.de

Abstract

A quick and easy identification of microorganisms is desirable for a variety of reasons. For example, in medical diagnostics hours could decide about the health status of a patient and in food processing and safety time is money. Besides the common identification by a combination of cultivation on different nutrition media and additional tests like morphology tests and Gram staining there are faster and more powerful techniques like DNA-based methods or matrix-assisted laser desorption ionization - time of flight mass spectroscopy (MALDI-TOF MS). Optical spectroscopy in combination with chemometric methods are also allowing an identification of microorganisms. Numerous publications have already shown that a reliable identification of bacteria via Raman spectroscopy is feasible [1] [2] [3] [4]. However, these promising methods aren't used routinely yet. Here, we show the process of calibration development and the difficulties of transferring calibrations from one device to another.

First, we established a method to obtain spectra of sufficient quality by using a confocal Raman microscope with an excitation wavelength of 633 nm and a 100x magnification. Dominating fluorescence effects were mostly bleached out by pre-irradiation for up to 15 minutes. We collected nearly 3000 spectra from nine different none pathogenic microorganisms to develop robust calibration models and 900 spectra to validate the models. The cultivation conditions were standardized, and we used both completely different genera and microorganisms differ on strain level. The data pre-treatment of the spectra comprised baseline correction, smoothing, normalization (Fig.1 (a)) and a principal component analysis (PCA) (Fig.1 (b)). The predictive models based on quadratic discriminant analysis (QDA), the k-nearest neighbor algorithm (kNN), and support vector machine (SVM) were created with different numbers of principal components (PC) and using a five-fold cross-validation. The theoretical prediction accuracies for the most accurate models are 99.0 % (QDA), 99.1 % (kNN) and 99.7 % (SVM). For practical validation, totally new spectra have been used which weren't included in the calibration data set. The accuracies of the prediction in practice are 98.1 % (QDA), 97.1 % (kNN) and 97.0 % (SVM).

To proof general applicability of our method we collected additional data using a different Raman device where we used both the same as well as two other excitation wavelengths. Although the setup was nearly the same, it was necessary to customize exposure time, laser power and the number of accumulations to gain comparable spectra at 633 nm excitation. Different numbers of datapoints for spectra, differences in the available bandwidths of each device and a specific signal to noise ratio are minor problems which can be solved relatively easy. It was noticeable that some features of the spectra were characteristic for the used devices. For example, there was a "negative peak" visible in all spectra of Fig. 1 (a) and in the left picture of the comparison in Fig. 1 (d) shortly before the phenylalanine peak at around 1000 cm^{-1}. This phenomenon is most likely caused by a speck of dust on the grating within the Raman measuring system.

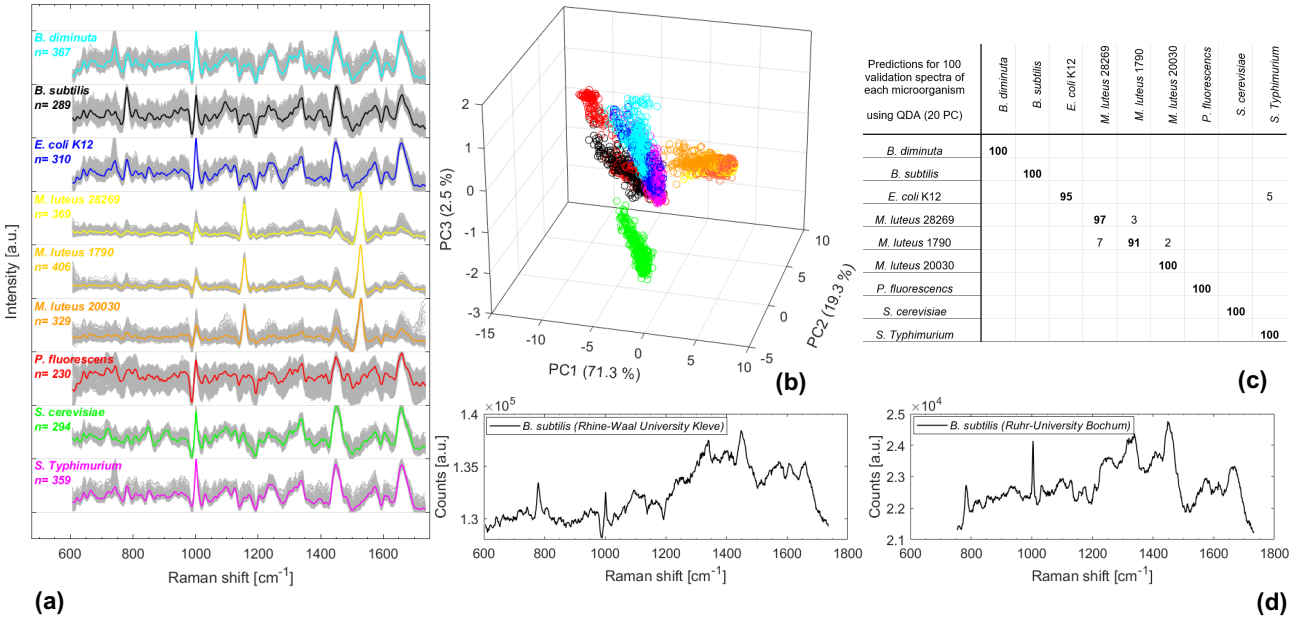

Fig.1: (a) shows the pre-treated Raman spectra of nine different microorganisms for calibration; (b) shows the first three components of the PCA; (c) shows the number of predictions for each microorganism from one of the used classifiers; each row shows the right predictions (bold) and the number of false predictions; the kind of false predictions goes out of the columns; (d) shows the comparison of two untreated Raman spectra measured in Rhine-Waal University Kleve (left) and in Ruhr-University Bochum (right).

So literally a single speck of dust in one of the optical elements within the Raman measuring system can cause the incompatibility from developed predictive models for data gained on other devices. Nonetheless, spectroscopic methods are a promising alternative to traditional methods. After a fix on our device we could largely eliminate the effect and after a mathematical removal of the "negative peak" in our spectra, we could create predictive models which are able to achieve similarly good predictions for the external spectra. With an enlargement of the dataset by using more and different devices and with a suitable unified data pre-treatment more reliable calibrations could be developed. Progress in artificial intelligence and accessibility of appropriate software offer new possibilities and are also an approach we pursue.

Acknowledgements

We are very grateful to Mr. Markus Grafen from the Ruhr-University Bochum of the Faculty of Mechanical Engineering, who gave us the opportunity to use the equipment of the lab for Applied Laser Technologies.

References

[1] M. Harz, P. Rösch, K. Peschke, O. Ronneberger, H. Burkhardt and J. Popp, "Micro-Raman spectroscopic identification of bacterial cells of the genus Staphylococcus and dependence on their cultivation conditions", *Analyst*, vol. 130, no. 11, pp. 1543-1550, November 2005.

[2] K. Maquelin, C. Kirschner, L. Choo-Smith, N. van den Braak, H. Endtz, D. Naumann and G. Puppels, "Identification of medically relevant microorganisms by vibrational spectroscopy", *Journal of Microbiological Methods*, vol. 51, no. 3, pp. 255-271, November 2002.

[3] P. Rösch, M. Harz, M. Schmitt, K. Ronneberger, H. Burkhardt and J. Popp, "Chemotaxonomic identification of single bacteria by micro-Raman spectroscopy: application to clean-room-relevant biological contaminations", *Applied and Environmental Microbiology*, vol. 71, no. 3, pp. 1626-1637, March 2005.

[4] S. Strola, J. Baritaux, E. Schultz, A. Simon, C. Allier, I. Espagnon and J. Dinten, "Single bacteria identification by Raman spectroscopy", *Journal of Biomedical Optics*, vol. 19, no. 11, November 2014

27 Simulation modeling and sensor-system in the study of respiration processes on 3D solid models

Gennadij Lukyanov[1,2], Anna Rassadina[1,2], Artem Kasatkin[1], Konstantin Ganzhenko[1], Roman Neronov[3]

(1) Lab Sensorics, Faculty of Control Systems and Robotics, ITMO University, RF- 197101 ITMO University, Russia
(2) Microwave Microelectronics Lab, Faculty of Microelectronics and Radioengineering, Saint-Petersburg Electrotechnical University "LETI", RF-197376 Saint-Petersburg Electrotechnical University "LETI", Russia
(3) Otolaryngology Department, JSC "Modern Medical Technologies", RF- 190121 JSC "Modern Medical Technologies", Russia
E-Mail: gen-lukjanow@yandex.ru Web: https://en.itmo.ru/en/, https://etu.ru/de/universitaet/

Abstract

When solving problems of otorhinolaryngology regarding the study of nasal breathing, the formulation of an experiment on a real object is not possible. The nasal cavity is a branched miniature structure with numerous protrusions and irregularities. Placing diagnostic sensors inside the nasal cavity is difficult. In this case, simulation models and numerical simulations are required.

The simulation model and sensor-system to it partly replicate the idea of leading researchers in this direction [1,2]. The repetition of experience was required in view of the results of recent studies in the physiology of respiration [3-5]. It was found that the shape of the nasal cavity affects the direction of movement of air in it. Based on anatomical studies, three forms of the nasal cavity were identified: a wide (platyrhine), medium (mesorhine) and narrow (lepthorhine) nose [5]. The results of an experimental study are of the most immediate interest for practicing surgeons, because will improve the methods of surgery.

Numerous analytical studies in the clinic could highlight those three persons with the required types of nasal cavities [6]. Computer tomography of these persons became the basis for the creation of 3D solid models. Models of wide, medium and narrow noses were created. These models were produced of plastic in full size using 3D printing.

Earlier, on these models, simulation modeling of heat air flows was performed by using a thermal imager as research equipment [7]. However, the proposed method is indirect and requires further confirmation. For this purpose, imitational modeling of respiration was performed. Three 3D solid models of the nose were the object of the study, which were placed in an aquarium filled with distilled water. Objects of the study were three 3D solid models of the nose, which were placed in an aquarium filled with distilled water. When modeling the breath, water was run through the model using a pump. Visualization of water flows movement in the 3D solid model was performed by injecting a dye into the 3D solid model at the same velocity as that of the distilled water injection.

Natural environment - air is the first preference. But air is a transparent medium. Our use of tobacco smoke to visualize air flow in the model, as in similar studies previously [2], did not give a positive result. Smoke spread throughout the model and did not allow to identify the directions of air flow movement.

In going from air to water in order to save the nature of the flow, the Reynolds number was calculated using the well-known formula. The result of the calculation showed that the average flow velocity of water entering the model should be 14 times less than the average air velocity under the same conditions. The average value of air velocity is taken from previously conducted experiments with a prototype diagnostic sensor.

Dyes were used to visualize the flow of water. The dye velocity was support the same with water velocity. It was important for saving the dye stream filament. The choice of dye was determined by the requirements: (1) hydrous solution; (2) neutral solution (without acids and alkalis); (3) solution, not a slurry or emulsion; (4) low concentration; (4) resistant to air oxidation. As a result, two options were chosen - methylene blue and magenta.

The sensor system is shown in Fig.1.

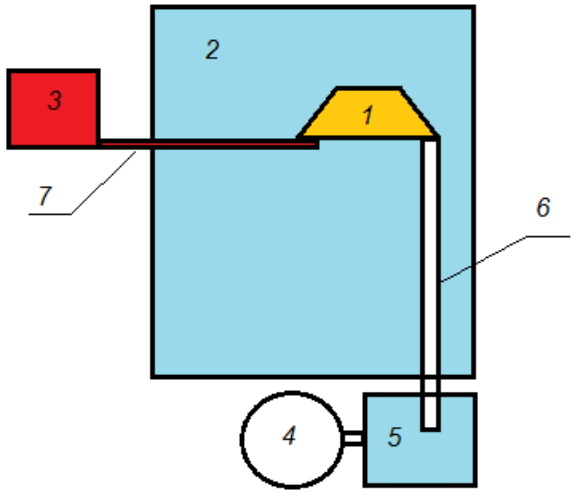

Fig.1: Sensor-system for study of respiration processes on 3D solid models, where (1)solid model, (2) aquarium, (3) pump with speed controller for supplying dye to the model through a silicone tube (7), (4) backing pump with speed controller for modeling for inspiration simulation, (5) buffer vessel and silicone tube for water dumping (6).

The simulation modeling results show that at the model of wide nose the flow tends to the upper areas of the model. In a narrow model of nose the flow moves along the bottom of the model. In the middle model of nose the flow was concentrated in the lower lobes of the model.

References

[1] G. Mlynski, S. Grutzenmacher, S. Plontke, B. Mlynski, and C. Lang, "Correlation of nasal morphology and respiratory function", *J. Rhinology*, vol. 39, pp. 197-201, 2001.

[2] G. Mlynski, S. Grutzenmacher, S. Plontke, W. Grutzmacher, B. Mlynski, P, C. Lang "A method for studying nasal air flow by means of fluid dynamics experiments", *J. z. Med. Phy.*, 10, 207-214, 2000.

[3] J. Znu "A numerical study of airflow through human upper airways". Singapore: *National University of Singapore*. 192 p., 2012.

[4] J. H. Zhu, H. P. Lee, K. M. Lim, Sh. J. Lee, D. Y. Wang, "Evaluation and comparison of nasal airway flow patterns among three subjects from Caucasian, Chinese and Indian ethnic groups using computational fluid dynamics simulation", *J. Respiratory Physiology & Neurobiology*, vol. 175, 62–69, 2011.

[5] R. V. Neronov, G. N. Luk'yanov, A. A. Rassadina, A. A. Voronin, A. G.Malyshev, "The effect of the nasal cavity form on air flow distribution during inhalation", *J. Russian Otorhinolaryngology*, vol. 1, no.86, 83-94, 2017.

[6] R. V. Neronov, A.I. Gaivoronovskii, "The specific of lepto-, meso- and platyforms of nasal cavity", *J. Russian otorhinolaryngology*, vol. 5, no. 84, pp. 72-79, 2016.

[7] G.N. Lukyanov, A.A. Rassadina, A.G. Malyshev, R.V. Neronov, E.N. Oslopovskikh "Air Flow Estimation through the 3D Natural Model of Nose", *IEEE Workshop 2017 Industrial and Medical Measurement and Sensor Technology Vehicle Sensor Technology (Sensorica 2017): Abstractbook*, pp. 52-53, 2017.

[8] G.N. Lukyanov, A.A. Voronin, A.A. Rassadina "Simulation of Convective Flows in Irregular Channels on the Example of the Human Nasal Cavity and Paranasal Sinuses", *J. Technical Physics*, Vol. 62, No. 3, pp. 484-489, 2017.

28 Development of an Impedance Measurement Circuit with AD5933 for Nanocomposite Based Pressure Sensor

Rajarajan Ramalingame, Nikhil Sudhir Apte, Olfa Kanoun

Technische Universität Chemnitz, Reichenhainer Straße 70, 09126 Chemnitz, Germany
E-Mail: rajarajan.ramalingame@etit.tu-chemnitz.de

Abstract

Nanocomposite based pressure sensors exhibit both piezoresistive and piezocapacitive behaviour under applied pressure. Thus, the measured electrical parameter of the sensor depends on the type of excitation signal. Hence, an impedance measurement on such sensors can provide a complete change in the electrical signal under pressure. Such an impedance measurement system based on AD5933 for the nanocomposite pressure sensor is presented in this paper. The measurement system can self-calibrate with tunable gain and is capable of measuring impedance in the range of 1 kΩ to 1 MΩ with a relative error less than ±1% and an acquisition time of 2 ms. Additionally, the results of the measurement system are compared with standard devices such as "Agilent 4294A Precision Impedance Analyzer" and "Agilent 4284A precision LCR meter". As a future enhancement, the measurement system could be equipped with a multiplexer module to interface multiple sensors.

Introduction

Electrical impedance measurement has proven its feasibility in several sectors including medical applications like body composition analysis and skin electrode measurement. Despite several highly precise benchtop measurement devices for impedance, compact, portable and programmable impedance measuring system is still far from reality. Manufacturers like Analog Devices have introduced the first integrated circuit (IC) dedicated to measuring impedance, AD5933 [1]. The AD5933 evaluation board contains all the hardware and the software resources required to realize a system for measuring and characterizing impedance. Moreover, this evaluation board is capable of measuring impedance in the range of 1 kΩ to 10 MΩ and frequency up to 100 kHz with a manual calibration process and a programmer gain amplifier (PGA). Consequently, the application of this circuit refers to the realization of complex impedance measurement and measurement of non-electrical quantities through impedance measurements [2]. Other impedance measurement board such as AFE4300, ADUCM350 and MAX32600 are dedicated for bioimpedance measurement with several limitations such as narrow or selective frequency of operation [3], narrow impedance range [4] and complexity to integrate at a chip level. Impedance measurement circuit using AD5933 are typically deployed in the field of bio-impedance. Even-though AD5933 does not supply the wide frequency range of 1 Hz to 100 kHz as required for microbiology [5], discrete frequency like 50, 100, 300 and 400 kHz are suitable for impedance cardiograph [6]. Furthermore, the error caused by resistive measurement is around 1.06% and that of impedance with capacitance components is around 2.97% [7, 8].

(a)

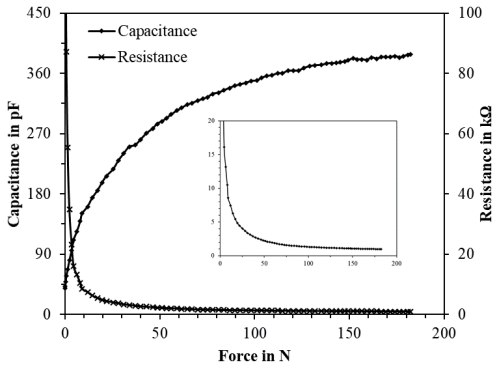

(b)

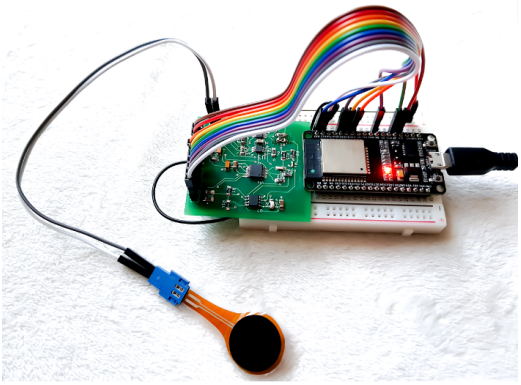

Fig. 1 (a) Nanocomposite pressure sensor exhibiting both resistive and capacitive change under applied pressure, (b) the proposed circuit interfaced with the nanocomposite sensor

Soft pressure sensors [9] based on nanocomposite material such as polydimethylsiloxane (PDMS) and carbon nanotubes (CNTs) work on the principle of piezoresistive [10] or piezo capacitive [11] under applied pressure as shown in Fig.1a. By simple measurement techniques like voltage divider or wheat stone bridge, the change in resistance under pressure can be measured. In order to achieve more sensitivity and precision, an impedance measurement is a feasible option. The main challenge with resistance measurement is that it saturates beyond certain high pressure as the generated conduction paths in the sensor under pressure has reached a percolation threshold [11]. An impedance measurement on such pressure sensors can be beneficial to avoid saturation at high pressures.

The proposed measurement system (Fig. 1b) is based on AD5933 IC, which is capable of self-generating sinusoidal signal at any desired frequency, measuring at 12-bit ADC resolution, I2C communication and filtering for impedance measurement. Thus, this paper aims to develop a compact programmable impedance measurement technique based on AD5933 as a portable embedded solution for highly sensitive nanocomposite-based pressure sensors.

Results and discussion

The proposed measurement circuit must be evaluated for the feasibility to measure impedance changes in nanocomposite pressure sensors under pressure. Before the evaluation at a sensor level, standard elements such as resistor and capacitors and the combination of both were measured using the proposed circuit and compared with the results of standard devices as shown in Fig. 2a. It can be observed that the circuit is able to measure accurately resistances with a relative error of less than 0.8%. With the inclusion of capacitance, depending on the element configuration, the relative error is less 0.3% for parallel RC element and over 4% for pure capacitors and series RC elements. This is advantageous in the measurement of nanocomposite sensors as the impedance response resembles a constant phase element [9] which is contributed by the parallel RC network in the nanocomposite.

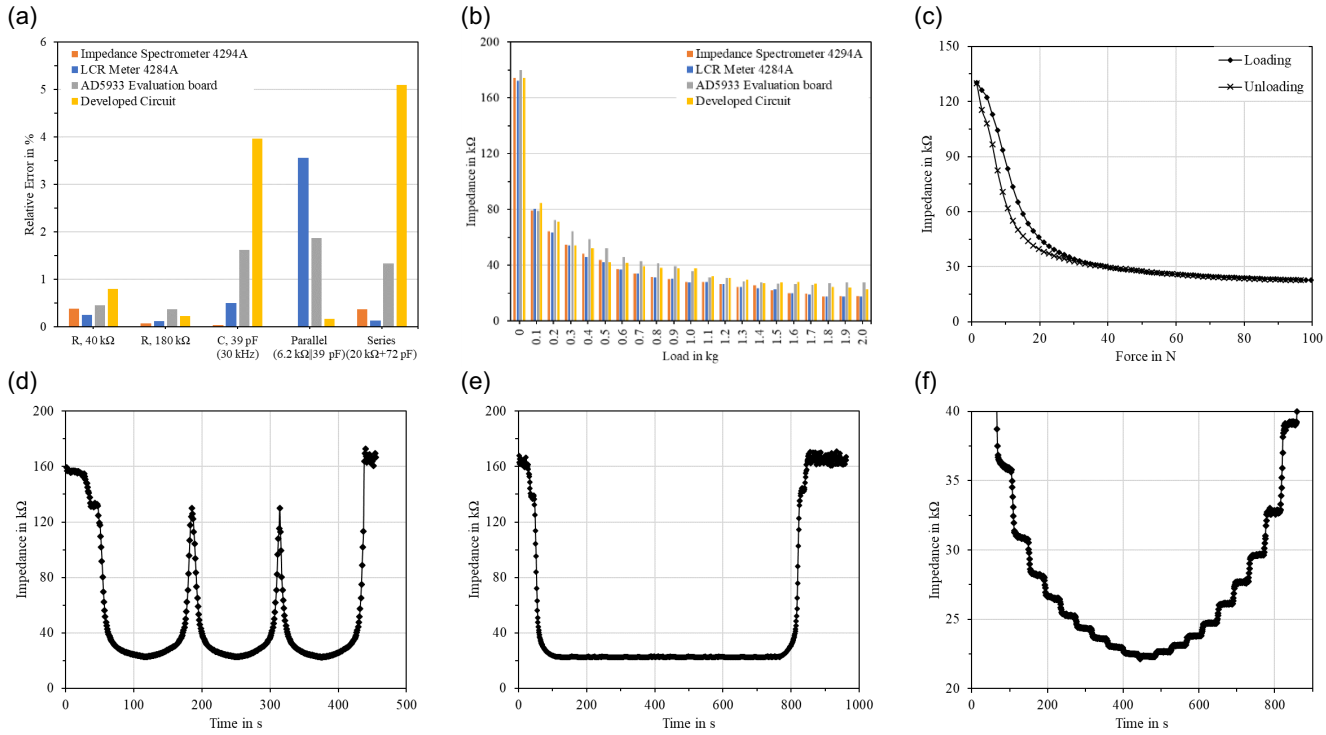

Fig. 2 (a) Standard elements measured with the proposed circuit and compared with other standard devices, (b) nanocomposite pressure sensor under different applied weights, measured with the proposed circuit and compared with other standard devices, (c) loading and

unloading curve of the nanocomposite sensor, (d) cyclic test on the nanocomposite sensor, (e) creep test on the nanocomposite sensor, (f) step loading test on the nanocomposite sensor

The nanocomposite sensor was interfaced to the circuit and the circuit is set to operate at a frequency of 50 kHz [11] which is the frequency corresponding to the dominant time constants of the nanocomposite sensor. The sensor was subjected to loading test with standard weights up to 2 kg in steps of 100 g. To evaluate the measured results the sensor was tested with standard devices with the same loading conditions. It is evident from Fig. 2b that the circuit can measure impedance change in the nanocomposite sensor under pressure and the measured values are the same as that measured with standard devices. Further experiments were performed on the nanocomposite sensor using a pressure test bench to evaluate the measurement capabilities of the circuit. The sensor was subjected to a loading-unloading test at a rate of 2 Ns^{-1} to a maximum load of 100 N. Fig. 2c shows the response of the sensor for one complete cycle. It can be observed that the circuit can measure both the response with high sensitivity until 20 N and the reduced sensitivity beyond 20 N. The sensor was then tested with cyclic loading-unloading at 5 Ns^{-1} to a maximum load of 100 N. Fig. 2d shows the cyclic behaviour of the sensor and it is observed that the sensor exhibits good repeatability which is essential for the continuous operation of the sensor. In-fact for continuous operation, the sensor should also exhibit good stability and hence a constant load of 100 N was applied on the sensor for 15 min as shown in Fig. 2e. Finally, a step loading test to a maximum of 100 N with a step hold time of 60 s for every 10 N was performed to estimate the step sensitivity of the sensor as shown in Fig. 2f.

Conclusion

The proposed impedance measurement circuit can measure the change in impedance caused by pressure on the nanocomposite sensor. The circuit utilizes AD5933 impedance measurement IC that can operate in any desired frequency in the range of 1 kΩ to 1 MΩ. The system is designed to auto-calibrate to set the necessary gain in the selected range based on the unknown impedance. The circuit can measure impedance with a relative error less than ±1% for resistive element and less than ±0.3% for parallel RC elements. This is especially beneficial for impedance measurement of nanocomposite sensor. Apart from measuring the pressure response of the sensor the circuit can also be used to evaluate the critical properties of the sensor such as repeatability, stability, hysteresis, sensitivity and step sensitivity. As future enhancements, a co-relation algorithm pressure-impedance and a multiplexing system to facilitate simultaneous impedance measurement on multiple sensors will be implemented.

Acknowledgement

The research work is carried out under the “Landesinnovationsstipendium (100284169)”, funded by the Sächsische Aufbaubank (SAB) and the European Social Fund (ESF).

References

[1] Datasheet by Analog Devices Inc. “1 MSPS 12-bit Impedance Converter, Network Analyzer AD5933”
[2] Mohd Akmal, Mhd Yusoff, “Development of AD5933 based Impedance Meter Prototype for Impedimetric Sensor Applications” 11th Asian Conference on Chemical Sensors ACCS 2015
[3] Liam Riordan by Analog Devices, “Application Note AN1053: Evaluation Board Example Measurement”
[4] Datasheet by Texas Instruments, “AFE4300 for Low-cost Integrated Analog Front End for weight Scale and Body Composition Measurement”
[5] K. Chabowski, T. Piasecki, A. Dzierka, and K. Nitsch, “Simple Wide Frequency Range Impedance Meter Based on AD5933 Integrated Circuit,” Metrology and Measurement Systems, vol. 22, no. 1, pp. 13–24, Mar. 2015.
[6] J. Ferreira, F. Seoane, and K. Lindecrantz, “Portable bioimpedance monitor evaluation for continuous impedance measurements. Towards wearable plethysmography applications,” Conf Proc IEEE Eng Med Biol Soc, vol. 2013, pp. 559–562, 2013.
[7] J. Ferreira, F. Seoane, A. Ansede, and R. Bragos, “AD5933-based spectrometer for electrical bioimpedance applications,” Journal of Physics: Conference Series, vol. 224, p. 012011, Apr. 2010.

[8] L. Breniuc, V. David, and C. Haba, “Wearable impedance analyzer based on AD5933,” in 2014 International Conference and Exposition on Electrical and Power Engineering (EPE), 2014, pp. 585–590.
[9] Ramalingame, R., Torres, R., Hu, Z., Chandraker, P., and Kanoun, O.: Electrical impedance analysis on nanocomposite-based pressure and strain sensors, 10th International Workshop on Impedance Spectroscopy (IWIS), September 2017, Chemnitz, 102–103, 2017.
[10] Ramalingame, R., Hu, Z., Gerlach, C., Rajendran, D., Zubkova, T., Baumann, R., and Kanoun, O.: Flexible piezoresistive sensor matrix based on a carbon nanotube PDMS composite for dynamic pressure distribution measurement, J. Sens. Sens. Syst., 8, 1–7, 2019.
[11] R. Ramalingame, A. Lakshmanan, F. Müller, U. Thomas, O. Kanoun: „Highly sensitive capacitive pressure sensors for robotic applications based on carbon nanotubes and PDMS polymer nanocomposite”, J. Sens. Sens. Syst., 8, 87-94, 2019

= fast 4 Seiten = Problem

29 Development of a measurement system for detecting contact erosion

Christoph Clemens[(1)], Nicole Keller[(2)], René Schäfer[(3)], Jörg Himmel[(1)]

[(1)] Institute of Measurement Engineering and Sensor Technology, University of Applied Sciences Hochschule Ruhr West, D-45479 Mülheim an der Ruhr, Germany
(2) Institute of Civil Engineering, University of Applied Sciences Hochschule Ruhr West, D-45479 Mülheim an der Ruhr, Germany
E-Mail: christoph.clemens@hs-ruhrwest.de Web: www.hochschule-ruhr-west.de

Abstract

In the case of seepage flow within earthworks, there is a risk that the induced flow forces will trigger material transport. If material transport occurs at layer boundaries between two adjacend soils, we speak of contact erosion. This may lead to the destabilization of buildings or dams/dikes. In order to ensure sufficient safety against contact erosion, there are hydraulic and geometric criteria [1] [2], which were deduced from different applications and have respective application limits. Thus it is likely that in some cases there is no valid criterion or the use of these criteria may lead to an uneconomical design. From both geotechnical and clients' perspective it would be efficient and desirable to not only calculate the risk of material transport by using the empirical criteria but also to evaluate the risk and the resistance to material transport by laboratory testing, which is the reason why a test cell is developed to investigate flow-induced material transport.

Method

The test cell is used to investigate hydraulic and geometric criteria for contact erosion. Two soils with different grain sizes (e.g. sand and gravel) were installed in the test cell. Water was pumped from the bottom of the test cell to the top. Thus, a hydraulic gradient was applied to the soils. This hydraulic gradient can cause a material transport, so the finer material from the bottom of the cell migrates into the upper, more coarse material. Due to this migration, the overall volume of the soil composition in the cell was reduced, which can lead to a loosening of the soil and this could result in a hydraulic heave (collapse). To prevent the soil from collapsing, a constant force was applied to the top of the cell.

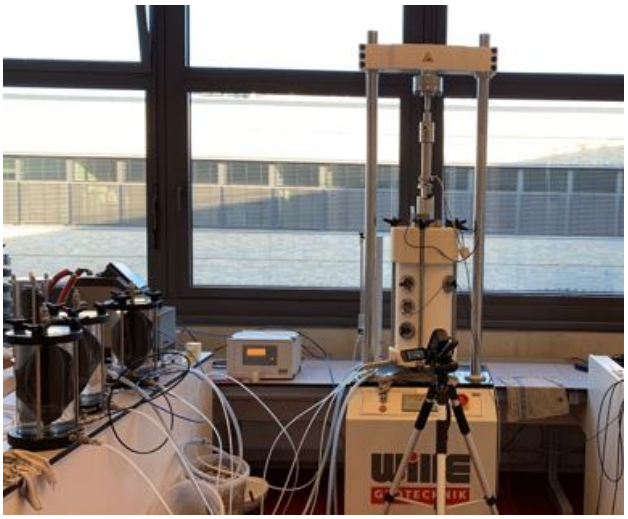

Fig.1: Test Cell for flow induced material transport in soils

For measuring the material transport, a flat coil was embedded in the coarser material above the layer boundary of the two materials. When material transport occurs, the density in the region of the coil changes. Because of the density change, the complex impedance of the coil also changes which was measured with a vector network analyzer [3]. In addition, the structural settlement was measured with a displacement encoder.

Results

The complex impedance of the coil has been measured at the frequency of 3 MHz and the hydraulic gradient increased over time.

Fig. 2 shows the complex impedance and structural settlement over time. The measurements show that the complex impedance starts increasing after 600s. The structural settlement followed this trend with a time delay. After 900s, the impedance reached a nearly constant value and the same applies to the structural settlement.

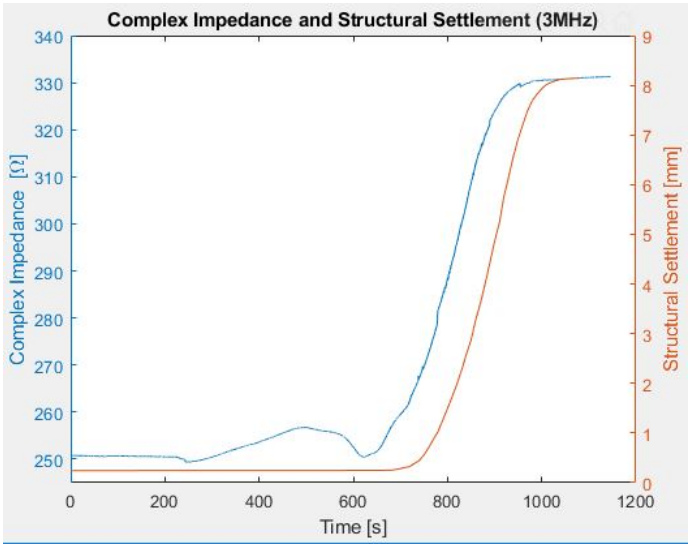

Fig. 2 Complex impedance and structural settlement over time

References

[1] BAW, Bundesanstalt für Wasserbau, "Merkblatt Materialtransport im Boden", Karlsruhe, 2013
[2] K.-F. Busch, L.Luckner und K. Tiemer, *Geohydraulik,* vol. 3, Berlin/Stuttgart, 1993
[3] Mario Radschun, Tino Morgenstern, René Schäfer, Olfa Kanoun, Jörg Himmel, "Improved VNA Hardware for Applications in Civil Engineering", SSD.2017.8166937, March 2017

30 A Permittivity Independent Method to Approximate Fill Levels from Measured Capacitances

Christian Weber[(1)], Johannes Trautmann[(1)]

[(1)] ifm efector gmbh, Department of Capacitive Sensor Development / Department of Software Development
D-88069 Tettnang, Germany
E-Mail: christian.weber@ifm.com Web: www.ifm.com

Abstract

Capacitive sensing is an interesting and comparatively low-cost method to determine fill levels of liquids or granulated material like salt or grain. Many interesting approaches to realize a capacitive level gauge have already been proposed. However, these approaches often rely on a fixed geometry, like a bypass-tube [1], a sensing unit built directly into a fuel tank [2] or a specially designed comb electrode mounted on the outside of the container [3]. Furthermore, the approximation of the fill level from the measured capacitance often depends on the dielectric properties of the medium to be detected. In this work, we present a method that uses multiple measured capacitances to determine the fill level independent of the dielectric properties of the medium.

Figure 5 shows the principle of operation. A relative measurement can be implemented by using an electrode array of ***N*** electrodes. Due to offset capacitances caused by the mounting of the sensor, e.g. installation clamps or dielectric properties of the container wall, it is necessary to conduct an empty offset compensation of the sensor, where for each electrode an empty offset value is measured and stored.

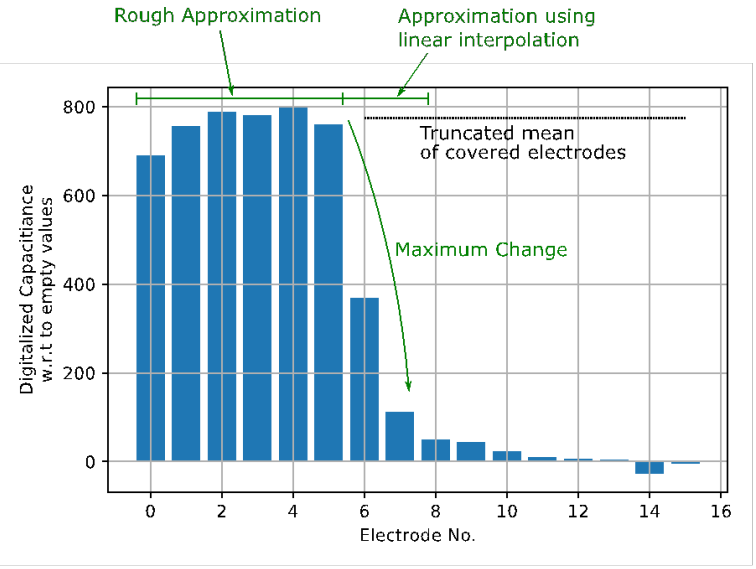

Figure 5: Principle of Operation for a sensor with 16 electrodes. The digitized capacitances are shown w.r.t. the stored empty values.

A rough approximation of the fill level can be found by searching for the biggest change along the electrode array (the fill level edge), which yields the number of electrodes that are covered with the medium to be detected. The approximation of the fill level can be carried out by using linear interpolation with respect to the truncated average values of the covered electrodes.

Special care must be taken when detecting limit states where no fill level edge can be found, i.e. a completely full or completely empty container where the electrode array is either completely covered or not covered at all.

In case of a completely empty container, we can compute the average over all measured values. If the average is below a certain threshold, which is related to mechanical tolerances and the dynamic range of the measurement circuit, the container is considered empty by the sensor.

If the electrode array is fully covered, a possible approach is store the extrapolated full values as shown in Figure 5. However, if another medium is filled into the container or its dielectric properties vary significantly over time, this method of detecting the full state of the container may fail, because the average measured is too small w.r.t. to the stored full values. Therefore, we propose to treat the

measured values of the electrodes as a vector with ***N*** elements and calculating the angle between that vector and a reference vector. A small value of the angle corresponds to a fully covered electrode array. The advantage of this method is that it is independent of the length of the measured vector and therefore independent of the medium to be detected. The reference vector can be determined by choosing its elements in such a way that the computed angle becomes minimal for a number of typical applications.

To validate the proposed approximation method, measurements using a grounded metal target (the medium to be detected), a step motor and a dial gauge have been carried out. The electrode array consists of 16 electrodes, a total length of 228mm and a width of 16mm. The target was mounted at a distance of 7.5mm from the sensor housing, which has a thickness of 1.8mm. Figure 2 shows the result of the validation measurement. The offset error of the approximation is 4% and the non-linearity is 1%. The offset error is due to stray field effects, because the capacitance of an electrode increases before the target has reached its lower edge. Non-linear behavior is caused by the changing fill level edge during target movement.

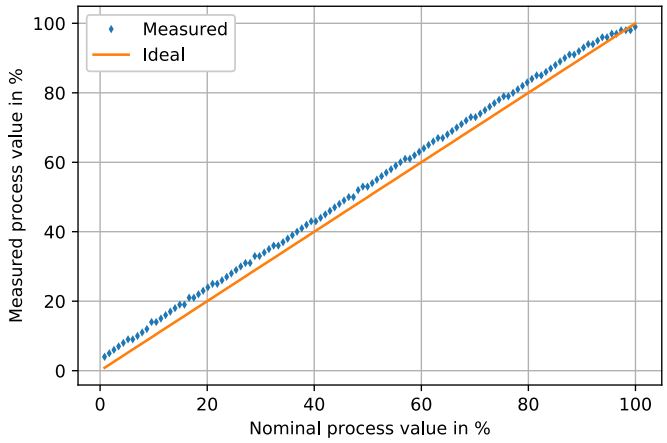

Figure 6: Result of validation measurements. The process value shows the percentage of the covered electrode length

To expand applications of capacitive level sensing to non-contacting applications with unknown container wall thickness and changing dielectric properties of the medium to be detected, a novel method to approximate the fill level from measured capacitances has been developed. After performing an offset compensation with an empty container, the fill level can be approximated by finding the maximum change along the electrode array. Approximation quality is improved by linearly interpolating at the fill level edge. If no fill level edge is present, the full state is detected by treating the measured capacitances as a vector and calculating the angle between this vector and a reference vector. A low angle indicates a homogenous coverage of the electrode and therefore a full state. This method is independent of the absolute signal values and therefore allows for changes in the medium to be detected without requiring additional compensation. Evaluation of accuracy was carried out using a grounded metal target (the medium to be detected), a step motor and a dial gauge. Accuracy of the approximation algorithm is sufficient for many targeted applications. Further field- and application testing will be carried out.

References

[1] J. K. Roy und S. Das, „Low cost non contact capacitive gauge glass level transmitter suitable for remote measurement and contro," in 2015 9th International Conference on Sensing Technology (ICST), 2015.

[2] M. E. Hamanaka, A. K. R. Segundo and S. A. Lopes da Silva, "Portable non-invasive capacitive transducer for measuring fuel level," in 2017 IEEE SENSORS, 2017.

[3] C. A. Gong, L. R. Chiu, C. H. Lin, Z. D. Hsu und P. Tu, „Low-Cost Comb-Electrode Capacitive Sensing Device for Liquid-Level Measurement," IEEE Sensors Journal, pp. 2896-2897, May 2016.

31 A compact EMAT for examination of the liquid volume inside metallic tanks

Kai Rieger[(1)], and Dirk Rueter[(1)]

[(1)] *Hochschule Ruhr West, Faculty of Measurement and Sensor Technology, University of Applied Sciences Ruhr-West, D-45478 Mülheim a. d. Ruhr, Germany*
E-Mail: kai.rieger@hs-ruhrwest.de Web: www.hochschule-ruhr-west.de

Abstract

Herein, an electric circuit for small electromagnetic acoustic transducers (EMATs) without the use of bulky permanent magnets is presented. The aim of this EMAT design is to examine metallic tanks when filled with liquids. Longitudinal ultrasound bursts at low MHz frequencies are required. To generate these burst, two capacitor banks are loaded up to 1200V and 300V. The EMAT circuit has to handle currents of 1.3 kA and higher. The challenge is to damp the pulse within μs to receive the weak echo signals in the μV - mV regime. There are some pitfalls in such an EMAT design, which will also be discussed.

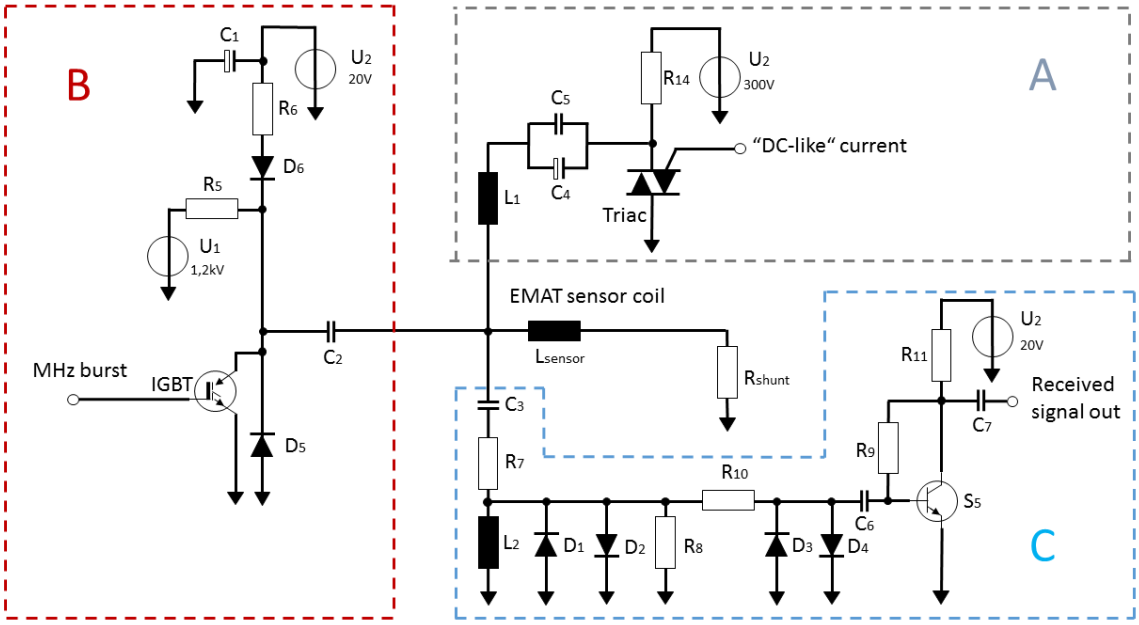

Fig.1: Electric circuit of the longitudinal wave EMAT.

Electromagnetic acoustic transducers (EMATs) are a promising solution for examining the volume of metallic liquid tanks (e.g., filled with oil or water). EMATs generate and receive ultrasound in metallic objects via electromagnetic coupling [1], i.e., a mechanical contact is not essentially required. Non-contacting ultrasound transduction is even possible for rough surfaces (e.g. rust) or non-metallic protection layers (paintings). Shear waves cannot propagate in liquids and, therefore, longitudinal ultrasound is required.

Longitudinal wave EMATs are less prominent, caused by the disadvantageous field topologies of the usually required and bulky permanent magnets. Strong permanent magnets also attract ferromagnetic particles and these could inhibit a suitable operation. Bourdais et al. describes an EMAT for longitudinal wave inspection in liquid sodium [2].

Rueter demonstrated in an experimental study the design of an EMAT without a bulky permanent magnet to generate and receive longitudinal ultrasound in an aluminum tube [3]. This paper presents further progress of Rueters circuit design. The main difference is the more distinct separation (= parallelization) of the different signal sources. Thus, a time offset between the rise of the "DC-like" current – required for the bias field - and the MHz pulse is adjustable. An increased "DC-like" current over-proportionally increases the received signal: almost quadratic response. A just linear slope is obtained with the amplitude of the MHz pulse. The experimental setup is investigated with a water basin, confined with aluminum walls.

The electric circuit in Fig.1 consists of three functional groups. Part A generates a slow rising and "DC-like" current (for the bias field). The electrolytic capacitor bank C4 of 2x220μF is charged up to 300V. A triac switches the "DC-like" current of 1.3kA and higher.

Part B generates a MHz burst. An IGBT must quickly switch a film capacitor bank C2 of 3x10nF, charged to 1200V. This capacitor and the inductivity of the sensor coil determine the characteristic LC-frequency of the pulse. An additional low-voltage capacitor C1 ensures a small DC current to keep the IGBT in good conductivity after the MHz burst, until the reflected and incoming signal has to be detected.

Part C is the receiver to measure and amplifies the reflecting incoming ultrasound.

There are several pitfalls in designing an electric circuit with these extraordinary strong (overdriving the characteristic specifications) current pulses. Film capacitor are recommended as DC blocking capacitors. Ceramic capacitors suffer from piezoelectric ringing effects, excited from strong signal bursts.

The use of resistors as carbon or metal film resistors for dampening the resonant circuit can lead to undesired noise: rapid heating induces thermal crackles, which easily covered the delicate echo signal.

High and transient current pulses in the wires induce pulsed Lorentz forces (a mechanical momentum and then movements inside a strong magnetic field), which also provides undesired artefacts. In a real world application these wires have to extend at least 10cm and more to place the relatively small sensor coil at the target. A solution for the problem is the use of wide copper foil instead of wires to reduce the current density and thus the Lorentz forces.

Another pitfall is the choice of an unfavourable ratio between the aluminium wall thickness and the ultrasound burst period λ. The aluminum wall behaves as an acoustic transmission line. Ideal is a $\lambda/2$ line, which ideally couples the water to the EMAT. Conversely, a $\lambda/4$ transmission line results to much weaker ultrasound transduction.

For subsequent circuits, an adjustable resonant frequency for different wall thicknesses is of interest. The simplest way to tune the characteristic emission frequency is to adapt the capacity C2.

Acknowledgements

This work is supported by the DFG (Deutsche Forschungsgemeinschaft) contract RU 2120/4-1

References

[1] M. Hirao and H. Ogi, "EMATs for Science and Industry: Noncontacting Ultrasonic Measurements," *Springer Science + Business Media*, New York, NY, USA, 2003.

[2] F. Le Bourdais, T. Le Pollès and F. Baqué, " Liquid sodium testing of in-house phased array EMAT transducer for L-wave applications," *4th International Conference on Advancements in Nuclear Instrumentation Measurement Methods and their Applications (ANIMMA 2015),* April 20-24, Lisbon, Portugal, 2015

[3] D. Rueter, "Experimental Demonstration and Circuitry for a Very Compact Coil-Only Pulse Echo EMAT," *Sensors,* pp. 926-941, April 2017.

32 Coin Sorting using Multi Frequency Inductive Sensor Systems

Rohan Munjal[(1)], Frank Wendler[(1)] and Olfa Kanoun[(1)]

[(1)] Chair for Measurement and Sensor Technology, Technical University of Chemnitz, Chemnitz, Germany
E-Mail: rohan.munjal@etit.tu-chemnitz.de Web: https://www.tu-chemnitz.de/etit/messtech/

Abstract

The reliable differentiation between original and counterfeit coin currency is an essential means of fighting crime and securing cash circulation for keeping healthy economy. There is sharp increase in counterfeiting of euro coins especially 2 euro coins, which requires a further development of the sensor system to differentiate between the original and counterfeit coins. Nowadays, it is a decisive quality feature on a coin counting machines.

In this paper, we propose an embedded inductive measurement system using impedance spectroscopy for differentiating of the various coins from different countries. The system is based on the principle of eddy current sensors using an inductive coil to measure the impedance of the coin present in vicinity. The system result shows that the bi-metallic 2 euro coins can be differentiated from counterfeit coins and coins from other countries having similar metal composition with similar physical and magnetic properties.

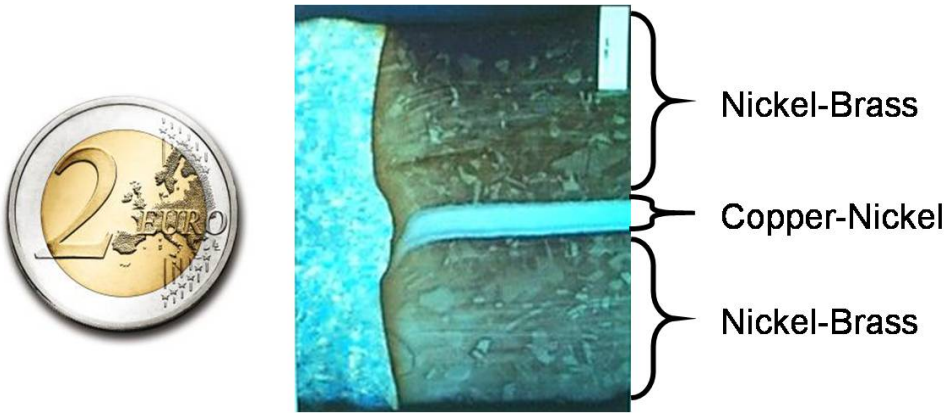

Figure 1: 2 Euro coin (left) and microscopic cut through the cross-section of the coin (right)

Introduction: Coins are manufactured out of individual metal sheets by stamping with a die having a certain physical properties such as weight, size, thickness, conductivity [1], magnetic properties like permeability [2] and acoustic properties [3]. The aim of the minting facilities is to create individual coin sets with distinct and precisely defined properties. For this reason complicated structures are created in most modern coins like the 2 Euro coin displayed in Figure 1. The counterfeiting of coin is the imitation of the genuine coin with respect to its properties. Coin discriminators also known as selectors, are present in coin vending machines and differentiate between a genuine and a fake coin [4]. The different methodologies can be used to sort out the coins such as image recognition using image abstraction and spiral decomposition [5], image recognition using neural networks [6, 7, 8], compact vision based system using optical sensors [9], pattern recognition using eigenspace approach [10] and sorting coins on the basis of magnetic features using inductance measurement.

In this paper, we focus on the design of an eddy current based embedded solution for inductance measurement with the main aim to eliminate the 2 euro counterfeit coin and coins with similar magnetic properties as that of 2 euro coin. With the introduced multi-frequency eddy current sensor system, we can achieve the defined penetration of the excitation signal in the coin and gather information out of different layers of the individual coin.

The different coins from various countries were tested and sorted out on the basis of inductance magnitude against the phase difference at a signal frequency of 10 kHz as shown in Figure 2.

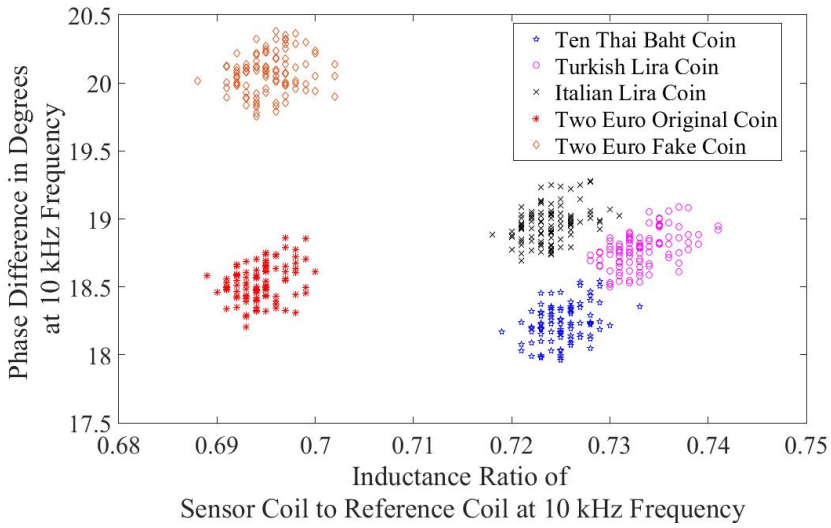

Figure 2: Inductance Value versus Phase Difference for Different Coin

Classes at 10 kHz

References

[1] P. Davidsson, "Coin Classification Using a Novel Technique for Learning Characteristic Decision Trees by Controlling the Degree of Generalization", *Ninth International Conference on Industrial & Engineering Applications of Artificial Intelligence & Expert Systems* , Gordon and Breach Science Publishers, Sweden, pp. 403-412, 1996.

[2] Ph. A. Passeraub, P-A. Besse, C. de Raad, 0. Dezuari, F. Quinet, R.S. Popovic, "Metallic Profile and Coin Imaging using an Inductive Proximity Sensor Microsystem", *Sensors and Actuators,* vol. 66, no. 1-3, pp. 225-230, 1998.

[3] H. Wu and M. Siegel, "Correlation of Accelerometer and Microphone Data in the Coin Tap Test", *IEEE Transactions on Instrumentation and Measurement,* vol. 49, no. 3, pp. 493-497, 2000.

[4] A. Carlosena, A. J. Lopez-Martin, F. Arizti, A. Martinez-de-Guerenu, J. L. Pina-Insausti, J. M. Garcia-Sayes, "Sensing in Coin Discriminators", *IEEE Sensors Applications Symposium*, California, USA, 2007.

[5] A. Chalechale, "Coin recognition using image abstraction and spiral decomposition", In *Proceedings of IEEE Int. Symposium on Signal Processing and Its Applications*, Sharjah, United Arab Emirates, February 12-15, 2007; pp. 1-4.

[6] M. Fukumi and S. Omatu, "Designing A neural network for coin recognition by a genetic algorithm", In *Proceedings of the International Joint Conference on Neural Network*, Nagoya, Japan, October 25-29, 1993; pp. 2109-2112.

[7] R, Bremananth, B. Balaji, M. Sankari and A. Chitra, "A new approach to coin recognition using neural pattern analysis", In *Proceedings of the IEEE Annual INDICON*, Chennai, India, December 11-13, 2005; pp. 366-370.

[8] A. Khashman, B. Sekeroglu and K. Dimililer, "Intelligent coin identification system", In *Proceedings of the IEEE Int. Symposium on Intelligent Control Munich*, Munich, Germany, October 4-6, 2006; pp. 1226-1230.

[9] M. Tresanchez, T. Pallejà, M. Teixidó and J. Palacín "Using the Optical Mouse Sensor as a Two-Euro Counterfeit Coin Detector", *Sensors*, vol. 9, pp. 7083-7096, 2009.

[10] R. Huber, H. Ramoser, K. Mayer, H. Penz and M. Rubik, "Classification of coins using an eigenspace approach", *Pattern Recognition Lett.*, vol. *26*, pp. 61-75, 2005.

33 Study of the dynamic properties of the flame using acoustic sensors

Gennadi Lukyanov [1,2], Evgeni Dyachkovsky[1] and Marina Simonova[3]

[1] Lab Sensorics, Faculty of Control Systems and Robotics, ITMO University, RF- 197101 ITMO University, Russia
(2) Microwave Microelectronics Lab, Faculty of Microelectronics and Radioengineering, Saint-Petersburg Electrotechnical University "LETI", RF-197376 Saint-Petersburg Electrotechnical University "LETI", Russia
(3) RF-196105 Saint-Petersburg University of State Fire Service of Emercom of Russia
E-Mail: gen-lukjanow@yandex.ru Web: https://en.itmo.ru/en/

Abstract

The study of the characteristics of the flame, as a rule, is based on the study of static or averaged process parameters. But the flame has a complex dynamics, due to the uneven reaction rate of combustion, fluctuations in the characteristics of the environment, etc. A method based on the study of the acoustic characteristics of the flame is used to study the dynamics of combustion. To implement this method, a sensor system consisting of electret sensors has been developed, experiments have been carried out in a laboratory setup, and initial data processing has been performed.

Combustion processes cause turbulent processes in the environment and are accompanied by vortex acoustic oscillations. These fluctuations contain all the information about the combustion process. As the wave propagates from the flame source, new and new areas of the air environment are involved in oscillatory movements with a frequency equal to the frequency of the oscillation source and with a phase lag depending on the distance to the source and on the wave propagation speed. This serves as a base for obtaining information about the combustion process. Preliminary studies of the dynamic propagation of acoustic waves of flame sources were carried out. A metal tray was used as such sources, the length of which varied from 55 cm to 110 cm, and the width was 10 cm. The photo (Fig. 1) shows a 110 cm long flume with burning gasoline. Electret acoustic sensors were used.

One of the examples of acoustic oscillations detected by sensors from a flame and the power spectral density for signals from sensors are shown in Fig. 2 On the given in fig. 2 time dependencies are clearly visible synchronous oscillations of the signals at the outputs of the sensors. Power spectral densities demonstrate that oscillations occur at frequencies of 30, 60, 130, and 280 Hz. These processes are associated with the properties of the combustible fuel and the conditions of combustion.

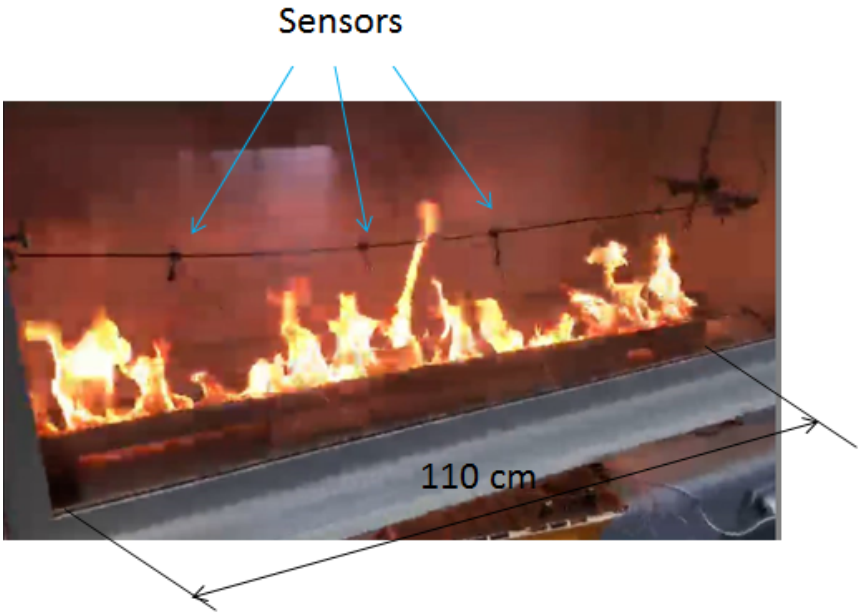

Fig. 1: The flume with burning gasoline. Electret acoustic sensors are used

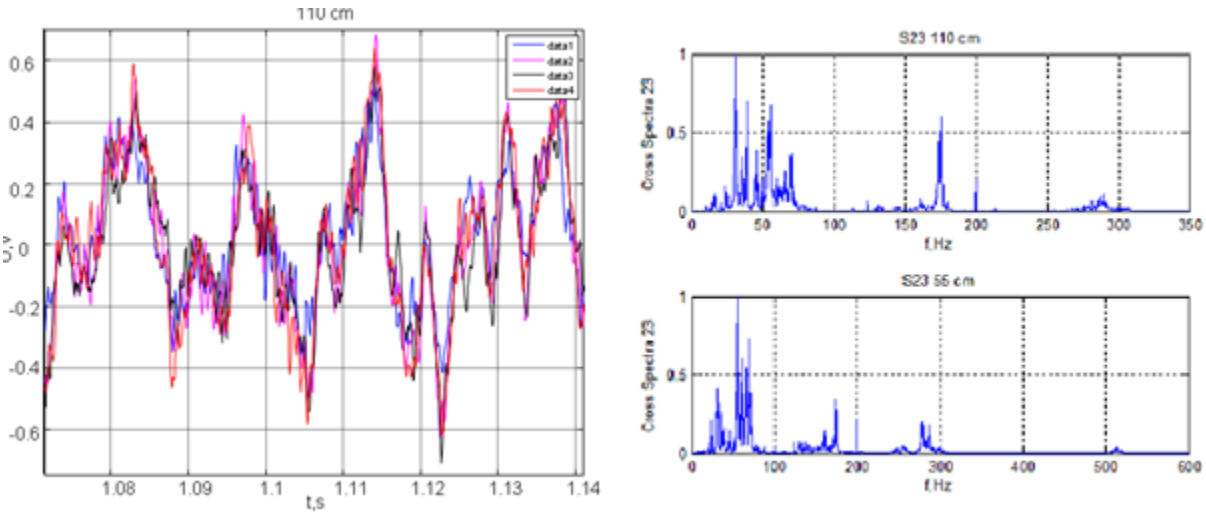

Fig. 2: Acoustic oscillations detected by sensors from a flame (left) and the power spectral density for signals from sensors for flumes 110 and 55 cm long (right)

Experiments have shown that acoustic sensors respond well to oscillations excited by the combustion process and can be used both to study the processes associated with burning and to control them. The study showed the possibility of using acoustic sensors to study the dynamics of combustion. In this case, measurements are made without direct contact with the flame.

This is a big advantage over other methods, as it has high speed (low response time), which allows you to perform measurements with minimal distortion.

References

[1] N. Ivanova, G. Lukyanov, F.N. Fett, M. Wirsum.“ Dynamic prediction of fluidized bed system“. *IFAC Proceedings Volumes.,* vol. 34, Issue 6, pp. 375-379, July 2001

34 Printed carbon nanotube-based sensors for the measurement of temperature and pressure

José Roberto Bautista-Quijano[(1)], Dhivakar Rajendran[(1)], Tatiana Zubkova[(2)], Peter Frenzel[(3)], Reinhard R. Baumann[(2,4)],, Heinrich Lang[(3)] and Olfa Kanoun[(1)]

(1) Professorship of Measurement and Sensor Technology,
(2) Institute for Print and Media Technology,
(3) Department of Inorganic Chemistry, Technical University of Chemnitz, D-09126 Chemnitz, Germany
E-Mail: olfa.kanoun@etit.tu-chemnitz.de Web: https://www.tu-chemnitz.de
(4) Fraunhofer Institute for Electronic Nano Systems, D-09126 Chemnitz, Germany
Web: https://www.enas.fraunhofer.de/en.html

Abstract

The current demand of smart wearable devices requires the development of flexible electronics able to detect, measure or monitor body activities and changes around its environment. An affordable approach to realize such devices is the integration of thin, small and flexible printed sensors that can be adapted to application specifications [1]. Printed sensors have a wide range of applications such as in sport medicine, health care and aerospace industry. There are different techniques that can be used to print sensors such as stencil printing, inkjet printing and screen printing. However, to realize printed sensors it is necessary to have a printable material with sensing capabilities. A promising printable sensing material are carbon nanotube (CNT)-based inks [2]. CNTs and polymer/CNT composites are known to have high sensing performance for diverse applications such as pressure, gas and temperature sensing [3-5].

In this work, two types of materials were used employing two different printing techniques to fabricate temperature and pressure sensors. A functionalized CNT-solvent based ink was inkjet printed on top of interdigitated silver electrodes (ISE) using Kapton® as substrate for the measurement of temperature. A layer of a commercially available polymer (Bectron®) was printed on top of the sensor as encapsulation method to reduce the effect of humidity on the temperature sensor. A mixture of commercially available CNTs dispersed in polydimethylsiloxane (PDMS) and isopropanol was used as ink to screen printing pressure sensors on top of ISE on a polyethylene terephthalate (PET) substrate.

Temperature steps of 5°C per 90 minutes were employed for the temperature sensing evaluations. The inkjet-printed temperature sensor showed high sensitivity to temperatures changes having a change in its relative resistance ($\Delta R/R_0$) of ~15% for a temperature up to 80°C. As visible from Fig.1(a), the electrical response of the sensors showed to have high linearity and exhibited a negative temperature coefficient which can be attributed to a negative thermal expansion of the CNTs here employed. Additionally, the electrical response of the sensors upon exposure up to 100% or relative humidity was evaluated. The non-encapsulated sensor presented a change in its relative resistance of ~55% indicating the need of reducing the effect of temperature on the sensor to ensure a proper performance in different conditions. Conversely, the Bectron-encapsulated sensor exhibited an almost negligible effect ($\Delta R/R_0$ < 1%) on the sensor for an exposition up to 100% of relative humidity proved that the encapsulating layer provided the sensor of an effective protection against humidity. For the evaluation of pressure sensing on screen printed sensor a pressure up to 245 kPa was applied to the sensor and the resistance was measured during 5 loading/unloading cycles. It is visible from Fig. 1(b) that the resistance decreases upon the application of the mechanical load. This is a typical electrical response given the reduction of distancing between the carbon nanotubes as the polymer is being compressed [3]. The sensor presented a high sensitivity as the resistance has a significant change of ~400 kΩ upon the application/release of the mechanical load. For this kind of pressure sensor sensitivities in the range of ~1.7 kΩ/kPa were found, showing a high pressure sensitivity.

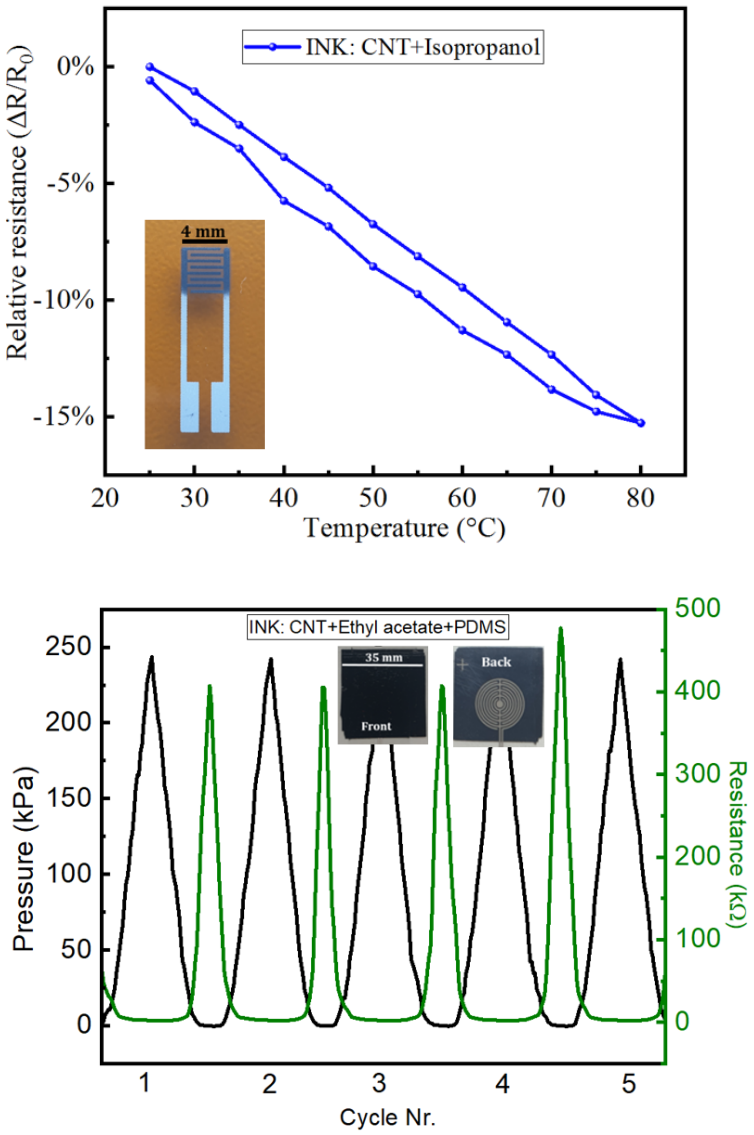

Fig.1: Sensing response of printed sensors and photographs of the sensors for: (a) Temperature and (b) Pressure.

The results found in this work demonstrated the feasibility of utilizing standard printing techniques for the fabrication of sensors for multiple physical stimuli. This kind of printed sensors can provide a reliable solution in wearable electronics were thin and flexible devices are desirable. This research was funded by the European Social Fund under the project "SenseCare".

References

[1] P. Lorwongtragool, et al., "A Novel Wearable Electronic Nose for Healthcare Based on Flexible Printed Chemical Sensor Array", Sensors, vol. 14, no. 10, pp. 19700-19712, October 2014.

[2] D. Mitra, et al., "Inkjet Printing and Intense Pulsed Light Sintering of Multiwall Carbon Nanotubes for Sensor Applications", J. Imaging Sci. Tech., vol. 62, no. 4, pp. 40409-1-40409-5, July 2018.

[3] R. Ramalingame, et al., "Flexible piezoresistive sensor matrix based on a carbon nanotube PDMS composite for dynamic pressure distribution measurement", J. Sens. Sens. Syst., vol. 8, no. 1, pp. 1-7, January 2019.

[4] A.S. Alshammari, et al., "Inkjet printing of polymer functionalized CNT gas sensor with enhanced sensing properties", Materials Letters, vol. 189, pp. 299-302, February 2017.

[5] R. Ramalingame, et al., "MWCNT-PDMS Nanocomposite Based Flexible Multifunctional Sensor for Health Monitoring", Procedia Engineering, vol. 168, pp. 1775-1778, 2016.

35 Justification of the choice of active thermography method for automated non-destructive testing of products made of composite materials

Ilya Kotovshchikov [1,2], Alexey Fedorov [1]

(1) Faculty of Control Systems and Robotics, ITMO University, Saint Petersburg, Russia
(2) OOO «Locus», Saint Petersburg, Russia
E-Mail: kotovshchikov.ilya@mail.ru Web: www.ifmo.ru

Abstract

The research carried out as part of the development of an automated non-destructive testing (NDT) system for blades made of composite materials (CM) inspection. The object of this study are aviation purposes products made of CM – helicopter tail rotor blades. The structure of the testing area of the product is a sandwich panel with a porous filler and carbon fiber reinforced plastic (CFRP) cover. The most common internal defect in the studied products, which need to detect, is the delamination of the CFRP cover from the sandwich panel filler.

The purpose of the research is the selection of an optimal NDT method for helicopter tail rotor blades inspection, and its approbation. To achieve this purpose, the following tasks were completed:

1. To analyze the most promising NDT methods for products made of CM inspection, and to choose the best one by preassigned criteria;
2. Experimentally validate (approbate) the selected method using defective samples.

The timeliness of the research caused by a new helicopter tail rotor blades producing technology adoption, including the replacement of a glass fiber reinforced plastic (GFRP) to a CFRP.

The analysis of a promising NDT methods for composites: Currently, methods of destructive and non-destructive testing are using for the composite blades quality control. Destructive methods has evident limitations: the cost of producing additional copies of the product, as well as the possible characteristics discrepancy between the witness samples and the other products of the production lot. The most common and promising NDT methods for the products made of CM inspection are: ultrasonic testing (UT), special low-frequency acoustic methods (SLFAM), radiation testing (RT), eddy current testing (ECT), active thermography (AT). Table 1 shows a result of the comparison of the most common and promising NDT methods, based on literature review [1-6], with the relative qualitative assessments of the most significant parameters of the methods in a five-point scale: from "1" - the method has critical limitations concerning this parameter, to "5" - the method fully satisfies the requirements associated with this parameter. In the last line of the table, we can see that the best NDT method for products made of CM inspection, by indicated criteria is the Active Thermography.

Table 1. Comparison of most common and promising NDT methods for CM inspection

Parameter \ Method	UT	SLFAM	RT	ECT	AT
Resolution	5	3	5	5	4
Maximal depth coverage	3	4	5	1	2

The measuring of the flaw depth	5	1	1	1	3
Easy operation	2	2	3	2	4
Portable configuration option	5	5	2	5	4
Automated configuration option	5	4	4	3	5
Operational safety	5	5	1	5	5
Inspection productivity	2	2	2	2	5
The influence of a part geometry	2	2	5	2	5
The influence of a part surface condition	2	2	5	2	4
The influence of a part material	3	4	5	1	4
One-sided access inspection capabilities	4	5	1	5	4
The noncontact inspection capabilities	2	1	5	4	5
Commissioning costs	4	4	2	4	5
Summary	**49**	**44**	**46**	**42**	**59**

The approbation of the AT method:

For the experimental approbation of the AT method for products made of CM inspection, the NDTherm system by Opgal was used. The approbation carried out by using two samples that have undergone mechanical strength tests. During the mechanical strength tests, the porous filler of the sandwich panel was partially destroyed, as a result, internal defects appeared in the samples. Figure 1b shows a thermographic defectogram (thermogram) of sample No. 1 and shows detected defects a delamination of the CFRP cover type. Detected defects are confirmed by the UT method (white marking in Figure 1a).

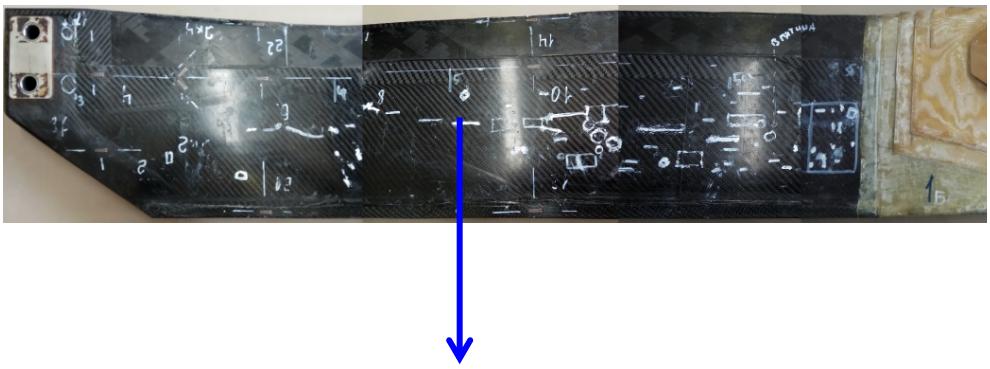

(a)

(b)

Figure 1 – The result of the sample No. 1 research using the AT method: a – general view of the sample with the white marking obtained by the UT; b - sample thermogram obtained by the AT method

Thus, the optimal NDT method for helicopter tail rotor blades inspection is the active thermography. The experimental approbation of the AT method has shown that the most common defects (the CFRP cover delamination type) are reliably detected. In the future, an automated NDT system for helicopter tail rotor blades inspection, which will include equipment for AT realization, will be developed.

References

[1] Vavilov V. P. Infrared thermography and thermal control //Moscow,"Spectrum" Publisher. – 2009.
[2] Kretov, E. F. Ultrasonic flaw detection in power engineering: a Handbook // "SVEN" Publisher. - 2007.
[3] Mishurov K. S., Murashov V. V. Determination of the composition and density of polymer composite materials in details and constructions by nondestructive methods //Polymer Science Series D. – 2016. – vol. 9. – no. 2. – pp. 176-180.
[4] Cai Z., Zou D., Liu C. Research on Eddy-Current Testing of Functional Polymer Composite Material //IEEE Transactions on Magnetics. – 2018. – no. 99. – pp. 1-5.
[5] Garcea S. C., Wang Y., Withers P. J. X-ray computed tomography of polymer composites //Composites Science and Technology. – 2018. – T. 156. – C. 305-319.
[6] Amenabar I. et al. Comparison and analysis of non-destructive testing techniques suitable for delamination inspection in wind turbine blades //Composites Part B: Engineering. – 2011. – vol. 42. – no. 5. – pp. 1298-1305.

Zu lang = Problem

36 Real time executable model for dynamic heat flow analysis of a solar hydrogen reactor

Steffen Menz(1), Arne Pahl(1), Philipp Weiler(1), Hannes Trumpf(1), Uwe Tröltzsch(1) and Thomas Fend(2)

(1) Rheinische Fachhochschule Köln (2) Deutsches Zentrum für Luft und Raumfahrt,
(2) Professur für Elektrotechnik und Elektronik Institut für Solarforschung, Vogelsanger Str. 295 Linder Höhe, 50825 Köln
51147 Köln
E-Mail: menz@rfh-koeln.de Web: https://www.rfh-koeln.de

Abstract

In this contribution, we focus on a real time model of heat transport and temperature distribution within a receiver of a solar hydrogen reactor. The use of radiosity method and significant optical characteristics including reflectance, transmittance, absorption, extinction and scattering are presented. The simulation results show good agreement with experimental data.

Introduction: Solar fuels offer promising potential to reduce CO2 emissions in the electricity, heat and transport sectors. Hydrogen can be produced by concentrated solar power (CSP) - plants via two-step thermochemical cycles. In the current application, cerium oxide is reduced at 1400°C and oxidized at temperatures between 900 - 1100°C. Research is carried out in various fields such as reactive materials, heat and mass transfer [1], reactor design [2], plant operation [3,4] and techno-economic analysis [5]. In order to increase efficiency, a fully-automated plant operation is to be developed. For this reason, a detailed simulation model is required which is used for state estimation of several aspects including fluid flow, heat transfer and chemical reaction in customizable abstraction levels. The proposed model will be executed in real time using a PLC, controlling the whole hydrogen production process.

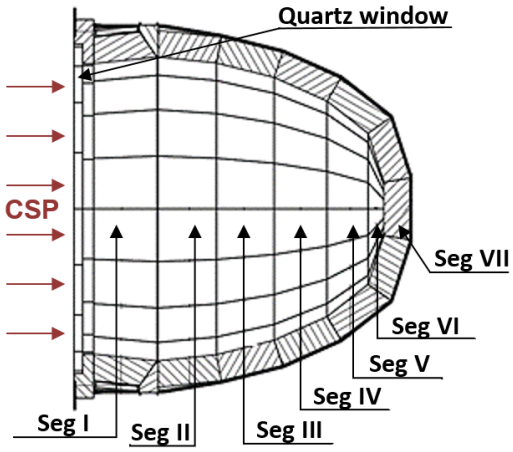

Fig.1: Receiver geometry and cell classification

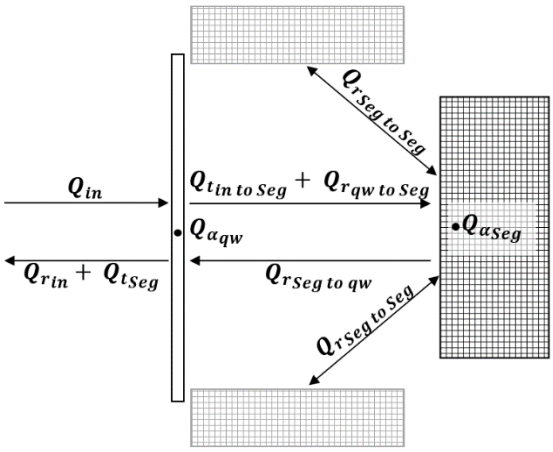

Fig.2: Model schematic

Model: Figure 1 shows a schematic of the solar receiver. The geometry is reshaped by using cell method, subdividing the absorber into seven isothermal segments (Seg I - VII) and the quartz window in one single segment (*qw*). Several optical characteristics have strong influence on the temperature distribution throughout the receiver. The incoming solar flux density (Q_{in}) is usually distributed inhomogeneous, comparable to a Gaussian distribution. The optical efficiency of the quartz window depends on spectral transmittance (*t*), absorbance (α) and reflectance (*r*). Basically, the porous absorber is implemented with the optical characteristic of a diffuse reflecting and emitting gray body. To increase model accuracy, additional influences are taken into account. Due to the inhomogeneous open foam material structure, extinction and scattering are considered. According to [1], the absorbance and reflectance varies caused by a change in color at the application temperature ranges. The spatial

distribution of reflection and thermal radiation between the surfaces is modeled by using the radiosity method [2]. The approximated radiative heat flow $\dot{Q}$ in W/s for each segment is given by the following equations:

$$\dot{Q}_\iota = \frac{A_i\,\varepsilon_i}{(1-\varepsilon_i)}\,(\sigma {T_i}^4 - H_i) \tag{1}$$

$$\dot{Q}_\iota = A_i\ \sum_{j=1}^{n} F_{ij}(H_i - H_j) \tag{2}$$

Equation 1 describes the balance of heat flow for one surface as the amount of emitted radiation and reflected irradiation using the radiosity H of the participating segments in W/m². Furthermore, ε is the emissivity, σ the Stefan Boltzmann constant in W/(m²K⁴), T is the temperature in K and A the area in m². Equation 2 contains the radiosity of surrounding surfaces including geometrical view factors F, which depend on the surface positions and the direction of emission. The localized heat flow distribution can be determined by a numerical solution of the resulting equation system. Analogously, a physical network is developed which is illustrated simplified in figure 2.

Results: Figure 3 shows a comparison of simulation and experimental data at a given concentrated solar input power as an example of segment VI. Due to the porous absorber structure, view factors can be subject to tolerances which may lead to slight local deviations. For this reason, a model optimization has to be performed.

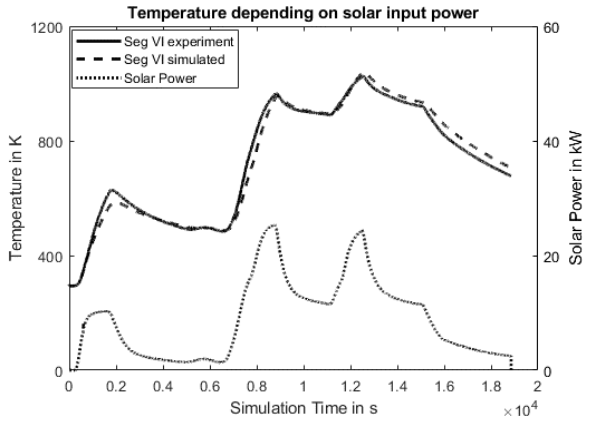

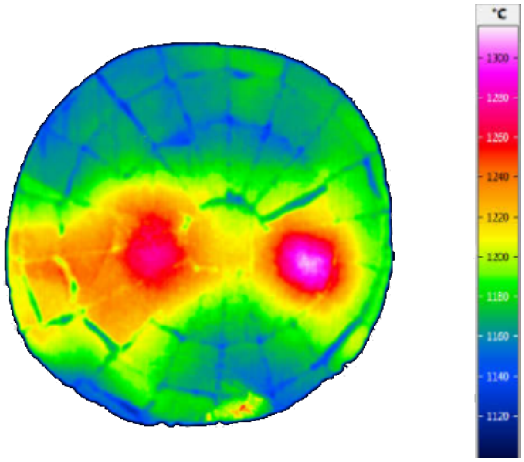

Fig.1: Receiver geometry and cell classification

Fig.2: Model schematic

References

[1] P. Furler, A. Steinfeld, "Heat transfer and fluid flow analysis of a 4 kW solar thermochemical reactor for ceria redox cycling", Chemical Engineering Science, vol. 137, pp. 373 - 383, 2015

[2] R. Palumbo, M. Keunecke, S. Möller, "Reflections on the design of solar thermal chemical reactors: thoughts in transformation", Energy, vol. 29, pp. 727 - 744, 2004

[3] J.-P. Säck, S. Breuer, P. Cotelli, "High temperature hydrogen production: Design of a 750 KW demonstration plant for a two step thermochemical cycle", Solar Energy, vol. 135, pp. 232–241, 2016

[4] S. Lorentzou et. al., "HYDROSOL-PLANT: Structured redox reactors for H2 production from solar thermo- chemical H2O splitting", SolarPaces, AIP Conference Proceedings 2033, Published Online: November 2018

[5] M. Moser, M. Pecchi, T. Fend, "Techno-Economic Assessment of Solar Hydrogen Production via Thermo- Chemical Cycles" Energies, vol. 12, issue 3, February 2019

This work was supported by the LeitmarktAgentur.NRW within the EFRE-Project ASTOR KHH-1-001D.

37 Experimental study of the oscillatory movement of the air flow from the heating surface

Gennadij Lukyanov [1], Elena Shapovalova[1]

[1] *Lab Sensorics, Faculty of Control Systems and Robotics, ITMO University, RF- 197101 ITMO University, Russia*
E-Mail: gen-lukjanow@yandex.ru Web: https://en.itmo.ru/en/

Abstract

Experimental studies of heat transfer from heating devices are usually reduced to estimating average values of heat flux, temperature, and heat transfer coefficient. Meanwhile, it is shown that there are fluctuations of these quantities, and the measurement of their average values often leads to an incorrect assessment of the characteristics of enclosing structures and heating devices and that there are significant periodic fluctuations in temperature and heat flux of the enclosing structure, both with a daily period and more rapid [1].

The experiments used a flat electric heater with a maximum power of 440 W and dimensions of 80x40 cm (Fig. 1).

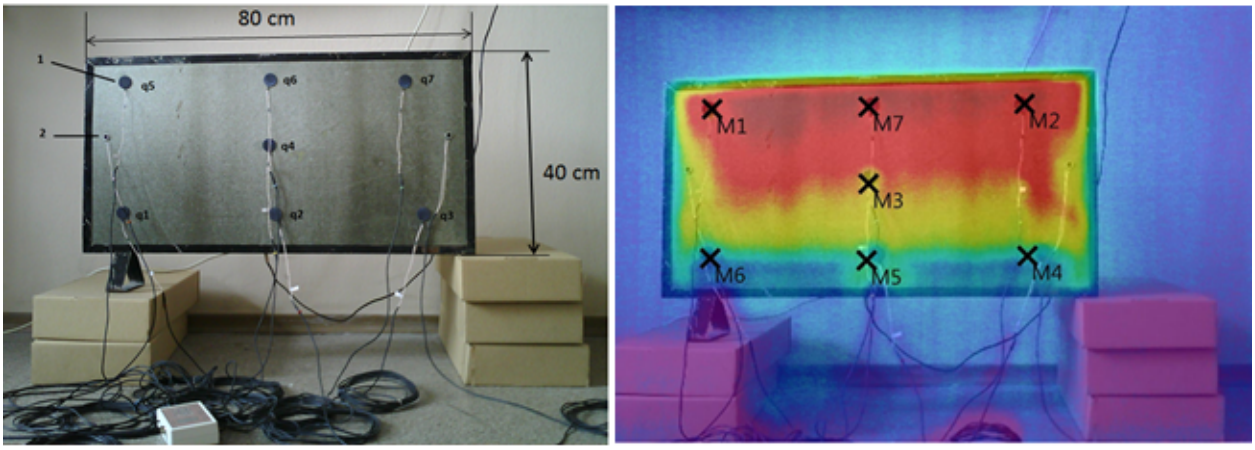

Fig. 1: Heater with sensors (left), and its thermogram (right)

The measurements were carried out using an instrument for measuring the density of the heat flux and temperature of ITP-MG “POTOK”. Measured values of temperature and heat flux on the heater surface. In addition, the temperature of the heater was recorded with a Testo 890-2 thermal imager. Heating was carried out to a temperature of t = 80 ° C. Graphs of changes in heat flux densities and surface temperatures of the heater were obtained (Fig. 2). The graphs show that when entering the stationary mode, oscillations of measured values occur, due to convective vortices from the heated air layers located below. Depending on the location of the heat flux sensor, the values differ 3.5 times.

To estimate the oscillations, the data obtained were approximated by exponential functions, which were then subtracted from the original curves. After the transformations, graphs of the amplitude of the periodic signal (convective vortices) versus frequency were obtained. In fig. 3, they are arranged according to the location of the sensors on the heater.

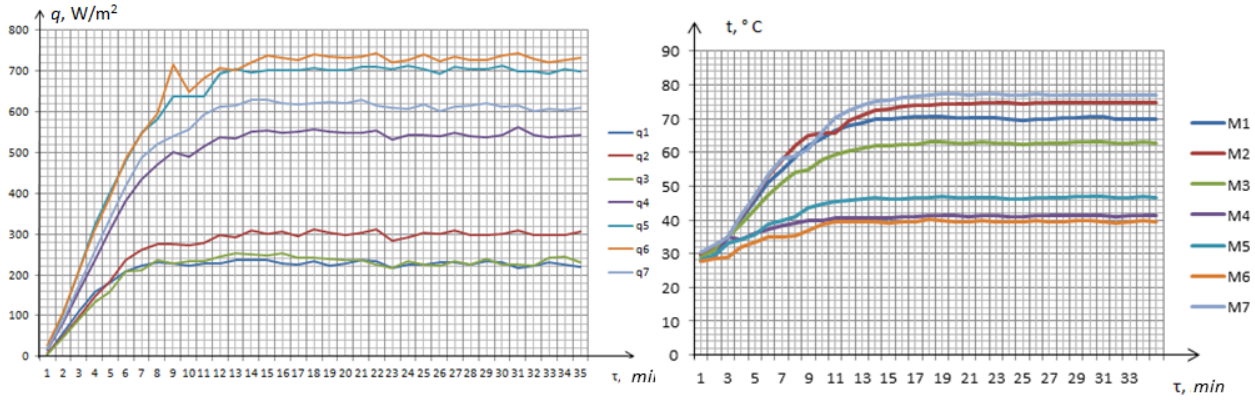

Fig.2: Changes in heat flux density and surface temperature of the heater

To estimate the oscillations, the data obtained were approximated by exponential functions, which were then subtracted from the original curves. After the transformations, graphs of the amplitude of the periodic signal (convective vortices) versus frequency were obtained. In fig. 3, they are arranged according to the location of the sensors on the heater.

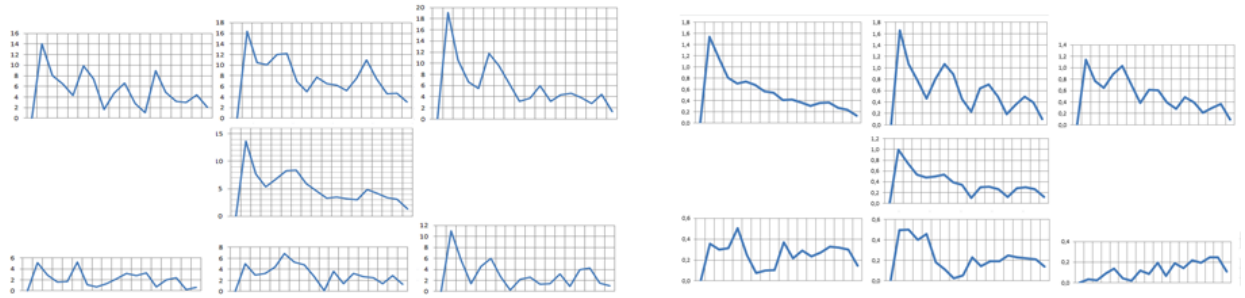

Fig. 3: Fluctuations of heat flow (left) and temperature (right) in accordance with the location of the sensors on the heater surface

The results will help improve the design of heat sources and find application in order to heat saving.

References

[1] K.S. Kostenko, G.N. Lukyanov, D.S. Petrov. "Experimental study of the dynamics of heat transfer through the enclosing structure" Journal of Instrument Engineering. no. 4, pp. 45-49, April 2010.

38 Determination of Measurement Errors Using Radio Thermometry in Closed Cavities Caused by finite Wall Conductivity

Fabian Ströder, Dawei Xu, Jörg Himmel, Klaus Thelen

Institute of Measurement and Sensor Technology, Hochschule Ruhr West, University of applied science, D-45479 Mülheim an der Ruhr, Germany
E-Mail: Fabian.stroeder@hs-ruhrwest.de Web: www.hochschule-ruhr-west.de

In [1], [2] and [3] a method of contactless temperature measurement is described. This system calculates the temperature of a weakly conductive object in a closed metal cavity. Therefore the thermal noise power density in the cavity is measured in the microwave band by an antenna [1]. For ideally reflecting cavity walls, the noise power is proportional to the object's temperature. For walls with finite conductivity, e.g. stainless steel the noise power consists of two parts, one is the emitted radiation of the target object, while the other part originates from the emissions of the conductive walls. To obtain the correct target temperature a factor must be found, defining the temperature portion of the target and wall. The translation can be set as

$$T_m = a \cdot T_t + (1 - a) \cdot T_w \tag{1}$$

Where T_m is the measured temperature, is the target´s temperature, the wall temperature and is the portion of temperature originating from the target´s noise power.

The cavity used in [1] and [2] has a size of 300 mm x 230 mm x 250 mm and is made out of aluminum. The electric modes inside the cavity containing an object are complex. To create a simpler, nearly one-dimensional mode structure, a smaller aluminum cavity with a size of 300 mm x 76 mm x 46 mm was built. The main components of the E-Field inside this structure are directed between the largest two sides of the cavity. The antenna is oriented the same way as the main E-Field components and placed in the upper section of the cavity. It is made out of silver-coated copper wire (0.8 mm diameter, 8 mm long). Salty water is filled to the smallest bottom side and acts as the target of interest.

The mentioned portions of the used components (walls, and water) correspond to the total absorbed power of both parts when external RF power is emitted through the used antenna. Accurate measurement of the power loss contribution of both wall and target is difficult to obtain with sufficient accuracy. The structure was simulated with CST-Microwave Studio.

To validate the quality of the simulation the outcome of an s11-parameter measurement of the simulation and the experimental setup has to be compared. If there is good consistency between s11 measurement and simulation, the latter can be taken as reliable thus there is enough evidence in using the results for a trustworthy determination of the mentioned temperature portions. The water level inside the cavity was chosen as 40 mm, 80 mm and 160 mm.

In Fig.1, the outcomes of simulation and measurement are shown for said water levels. We assume that the differences in peak heights originate from inaccuracies of the used model parameters concerning material properties. The shift in frequency can be traced back to an inaccurate measurement of the target´s height.

The outcome of measurement and simulation have substantial similarity in their signal sequence. Very likely, the simulation adequately represents reality. The power loss within the material is computed at a Water level of 80 mm (Fig.2). The focus is on the lowest mode at 2.068 GHz. The loss in the antenna (silver) is insignificant. Nearly 5% of the absorbed power is lost in the aluminum, so the major power couples with the object (water). Used in (1) we get an of 0.95.

As mentioned in [3] the system of interest uses aluminum or stainless steel cavities. The computed power loss in a steel cavity brings about an of 0.9.

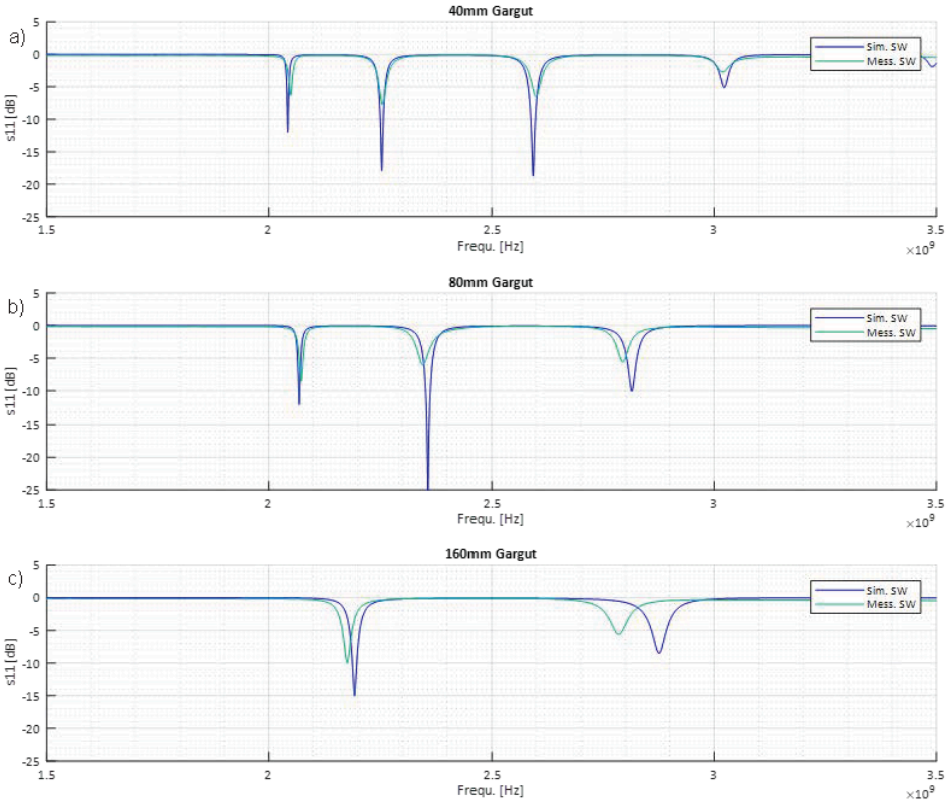

Fig. : s11 of simulation and measurement with different water levels. a) 40 mm; b) 80mm; c)160 mm

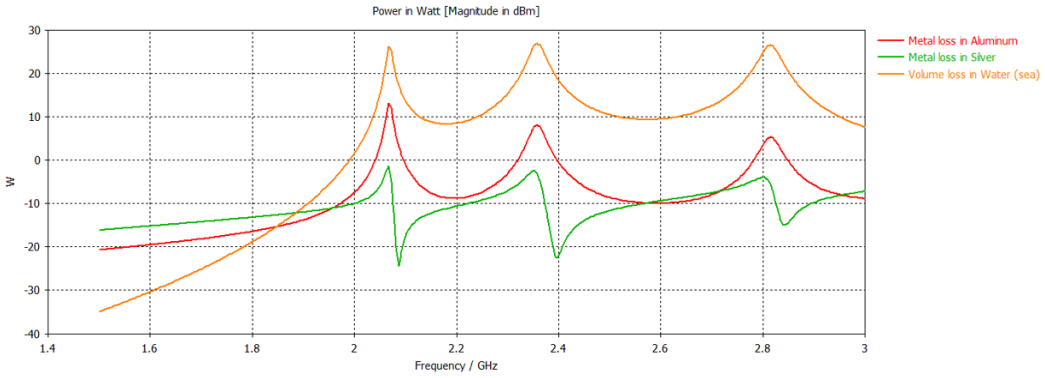

Fig. : Power loss in materials. Simulation with an aluminum cavity. (Picture out of CST-MWStudio)

References

[1] D. Xu, D. Rueter, and D. Erni, "Non-contact radiative temperature monitoring of blood plasma and packed red blood cells in a powerful microwave environment," *1st YRA MedTech Symposium (YRA-MedTech 2016), YRA - Young Researchers Academy MedTech in NRW*, April 8, University of Duisburg-Essen, Duisburg, Germany, session: Thermal Treatments, pp.66-67, 2016.

[2] D. Xu, K. Thelen, and D. Erni, "Temperature measurement of an object using blackbody radiation with compensation of impedance mismatch," *IEEE Workshop 2017 (Instrumentation & Measurement Chapter IEEE Germany Section) & SENSORICA 2017,* June 8-9, Hochschule Ruhr West, Mülheim a. d. Ruhr, Germany, paper no. 35, pp. 76-77, 2017.

[3] Hochschule Ruhr West, 45473 Mülheim, DE; RATIONAL Aktiengesellschaft, 86899 Landsberg, DE, „Verfahren zur berührungslosen Bestimmung der Temperatur eines Garguts in einem Gargerät sowie Gargerät“, DE 10 2016 113 216 B3, 2017.